Journal of Energy Storage 98 (2024) 113029

Contents lists available at ScienceDirect

Journal of Energy Storage

journal homepage: www.elsevier.com/locate/est

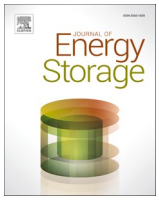

Research papers

3D carbon based phase change composites: A review on progress in fabrication strategies, thermal energy storage-conversion efficacy, prototypes, numerical models and applications

Madhurima Das, Urszula Stachewicz *

Faculty of Metals Engineering and Industrial Computer Science, AGH University of Krakow, 30-059 Krakow, Poland

ARTICLE INFO

Keywords:
3D carbon
Composites
Latent thermal energy storage
Conversion
Application

ABSTRACT

LHTES has emerged as an efficient and viable solution to mitigate a large amount of renewable and sustainable thermal energy wastage from solar radiation and industrial production in the twenty-first century. To date, 3D carbon/PCM composite has brought remarkable attention for achieving high performance in this field. This review provides a comprehensive outlook on the progress of 3D carbon and PCM-based composite materials as high-performance LHTES materials over the past 10 years, focusing on the synthesis strategies of 3D carbon, PCM infiltration process, and thermophysical attributes of 3D carbon/PCM composite. Furthermore, an effort has given to conduct rigorous literature to explore the utilization of different numerical assumptions and models for describing the heat transfer process between 3D carbon and PCM, thermal conductivity evaluation for the composite, and the mechanism of 3D carbon/PCM composite for battery thermal management and building application. The investigation of the advanced applications of 3D carbon/PCM composites reveals its potential utilization in building comfort, waste-heat recovery, power generation, and thermotherapy-based applications. Finally, the current shortcomings and future challenges associated with the developments of such composite are encountered. This comprehensive review will show the future pathway for researchers to develop high-performance composites in thermal management.

1. Introduction

To date, the dramatic rise in the energy crisis triggers a consequential threat to global socio-economic and environmental conditions. Over-consumption of fossil fuels, epidemic urbanization, and excessive energy waste are the most potential reasons for such issues [1]. In 2017, according to the US Energy Information Administration, about a ~28 % hike in total global energy consumption would take place in 2040 [2]. Apart from energy consumption issues across the globe, the wastage of energy is another growing concern to society. For example, ~5-7 % of electrical energy is wasted during the delivery of electricity from power stations to buildings or industries, while 60 % of loss arises from home appliances in the US [3,4]. Under this circumstance, energy-saving and perfect utilization of contemporary energy cradles, such as the ocean, biological, wind, and solar fuels, has evolved as an alternate theme to the scientific community [5,6]. However, the discontinuous supply of such renewable energies concerning the considerable demand over time and space is the additional drawback of such a project [7]. Under this circumstance, converting thermal energy from different energy sources coupled with thermal energy storage (TES) technology is an excellent alternative to mitigate such critical issues with reduced carbon emissions [8,9]. Sensible heat [10], chemical heat [11], and latent heat [12]

Abbreviations: AC, activated carbon; AA, azelaic acid; BN, boron nitride; CF, carbon foam; CA, carbon aerogel; CAGR, compound annual growth rate; Cu, copper; CuO, copper oxide; CW, carbonized wood; DMF, dimethyl formamide; ExFG,, exfoliated graphite; EG,, expanded graphite; T_f, freezing temperature; GF,, graphite foam; GO, graphene oxide; HTF, heat transfer fluid; HDIB, hexamethylene diisocyanate biuret; LA, lauric acid; H_m, latent heat of melting; H_f, latent heat of freezing; LHTES, latent thermal energy storage; LiB, lithium ion battery; T_m, melting temperature; MWCNT, multi-walled carbon nano tube; MOF, metal-organic framework; ODPA, octadecyl phosphonic acid; PS, polystyrene; PF, polyurethane foam; PRF, phenolic resin fiber; PEG, polyethylene glycol; KOH, potassium hydroxide; PC, porous carbon; PDA, polydopamine; PAA, palmitic acid; PW, paraffin wax; PCM, phase change material; PM, particulate matter; SEM, scanning electron microscopy; SA, stearic acid; SWCNT, single wall carbon nanotube; s-s PCM, solid-solid PCM; TES, thermal energy storage; λ, thermal conductivity; TD, tetradecanol; TSU, thermal storage unit; 3D, three dimensions; UGF, ultrathin graphite foam; VI, vacuum Impregnation.

* Corresponding author.
E-mail address: ustachew@agh.edu.pl (U. Stachewicz).

https://doi.org/10.1016/j.est.2024.113029
Received 7 January 2024; Received in revised form 6 June 2024; Accepted 14 July 2024
Available online 26 July 2024

are the primary classifications of TES technology. LHTES is a progressively evolving concept compared to sensible heat storage technology owing to its better heat accumulation density and mild change in temperature [13]. LHTES is the latent heat stored or released within the substance in potential energy, exploiting phase alteration without a remarkable difference in the substance's temperature. The thermal heat storage capacity of a substance having phase change attributes is generally denoted as [14]

$$Q_s = \int_{t_i}^{t_m} mC_{ps}dt + m\,f\Delta q + \int_{t_m}^{t_f} mC_{pl}dt \quad (1)$$

where Q_s is storage capacity (J), t_m is the melting temperature (°C), t_i is the initial temperature (°C), t_f is freezing temperature (°C), m is the mass of material (kg), C_{ps} is the specific heat of solid phase $kJkg^{-1}\,K^{-1}$, C_{pl} is the Specific heat of liquid phase $kJkg^{-1}\,K^{-1}$, f is the melt fraction, Δq is the latent heat of fusion (JKg^{-1}). PCM's most eye-catching and profitable benefits compared to the materials used in sensible heat storage (SHS) technology are high heat storage efficacy and the capability to work in an isothermal environment with small space occupation. PCM can be classified into several categories based on their chemical composition, phase change state, and melting temperature. Solid–solid PCMs, solid-liquid PCMs, liquid–gas PCMs, and solid-gas PCMs are the fundamental division of PCMs concerning their phase state change. However, solid-gas and liquid-gas PCM are the most ignored materials in LHTES applications because of their immense change in volume during phase transition [15]. The non-leakage attributes of s-s PCM during phase transition gradually attract the researcher's interest in further improving such PCM in practical thermal management applications [16]. However, s-s PCM has also not drawn huge research interest compared to solid-liquid PCM till date because of its complicated synthesis procedure and phase adulteration issues during solid-solid phase transition [15,17]. Organic, Inorganic, and eutectic mixture-based PCM is another division of PCM concerning its chemical composition [18]. In addition, PCM can also be classified into several categories in terms of their phase transition temperature [19]. At present, the market size of PCM is about 1.9 billion USD in 2019, and the anticipated market size of PCM will grow at a rate of over 17.4 % from 2020 to 2026 [20]. However, low thermal conductivity (~0.2-0.6 $W.m^{-1}\,K^{-1}$) [21], fast cooling [22], leakage during phase transition [23], and phase separation [24], sub-cooling is the common drawback of PCM for successful utilization of such materials in LHTES applications.

As we discussed earlier, nowadays, researchers are trying to design PCMs that satisfy thermal needs and can function as a media to convert a range of energy sources. Therefore, fabrication of PCM with energy conversion attributes, especially photo-thermal and electro-thermal, has gained significant attention in recent years. The primary mechanism of the energy conversion process involves the heat release by PCM composite caused by electronic transition or electronic motion of different electron-triggering media under stimuli of varying energy sources [25,26]. The joint venture of the photo, electrothermal energy conversion, and storage theme has widened the application scope of PCM, especially thermal management of electronic devices, high-temperature warning, anti-counterfeiting, and bio-medical applications [25,26]. Introducing virgin or inorganic-organic-based hybrid carbon media into PCM is the preferred choice for researchers to revamp the thermal conductivity, photo-thermal, electro-thermal efficiency, and leakage issues of PCM [27–34]. To date, 3D carbon possesses paramount importance from technological and essential scientific aspects owing to its lightweight [35,36], high surface area and tunable porosity [27], and brilliant thermal conductivity and electro-chemical attributes [28,29]. The efficient transfer of heat through the network-like thermal pathway of 3D carbon with reduced phonon scattering owing to its structural architecture is one of the most significant advantages of this filler in LHTES application compared to 2D fillers [8]. The microstructural and physicochemical properties of different 3D carbon arise mainly due to the various synthesis strategies and the use of different precursors when preparing different 3D carbon that significantly affect the chemical structure, surface texture, and reactivity of 3D carbon particles [31]. The commercial market value of graphitic carbon foam will overcome 40 million USD by the end of 2026 at a CAGR of 6.0 % [37], while the anticipated market size of graphite will reach 21.6 billion within 2027 with a CAGR rate of 5.3 % [38]. Therefore, the presence of 3D carbon in the composite structure has several benefits for thermal energy storage and management applications [32]. The primary benefit of 3D carbon/PCM-based composite is shown in Fig. 1a. As shown in Fig. 1b, the research interest and focus on different 3D carbon-based composites for LHTES application has increased rapidly, especially over the last 5 years. Based on such consideration, this review covers an outlook on the progress in different synthetic strategies, thermal energy storage, and conversion performance of different 3D carbon/PCM composites employed for LHTES applications.

Finally, the critical challenges and future opportunities for developing high-performance 3D carbon-based composite are highlighted. For a clear-cut research aspect, the focus and the importance of this review compared to recently published articles in this research arena are highlighted in Table 1. The architecture of the review is shown in Fig. 1c.

2. Preparation and modification strategies of 3D carbon and supplementary 3D carbon

Phonon propagation and scattering are the most crucial factors affecting heat transfer and conduction in the composite structure. The phonon diffusion can be drastically decreased due to phonon scattering via a change in the direction of the energy transfer in the composite structure [8]. The high loading of PCM with minimum leakage from carbon architecture is a pressing issue for real-field applications. Therefore, the selective choice of the proper carbon media or design of carbon media with a 3D porous network structure close to PCM is required for application purposes.

2.1. EG and its modified carbon skeleton

Expanded graphite is typically the modified form of graphite, posing porous and layered architecture with 150 times better expansion than graphite with inflated electrical and thermal attributes [42]. EG is typically prepared from graphite by expanding stacked graphitic layers via strong oxidizing agents or under microwave, thermal, and ultrasonic irradiation [43]. In general, EG has been prepared in the presence of potent oxidizing agents or intercalators via a chemical or electrochemical process, followed by the thermal treatment, which allows the removal of in-situ produced gaseous molecules as a by-product along the *Z*-axis [44,45]. This phenomenon enables the formation of worm-like porous 3D microstructure with defined interlayer spacing with lightweight, compressible attributes. Liang et al. designed an EG@GO-based carbon skeleton via the combination of compression of EG, impregnation of PW followed by milling to form particles, and addition of GO hydrosol in the presence of surfactant under mechanical agitation [46].

2.2. CF and its modified carbon skeleton

Carbon foam or porous carbon can be synthesized from a wide variety of carbonaceous precursors via the direct carbonization process, blowing agent method, templating replica method, the combination of foaming, carbonization, and graphitization process, depending on the nature of the precursors [47]. Some of the synthesis strategies are described below.

2.2.1. Carbonization

Lin et al. utilized PF as a template for carbon growth by treating phenolic resin fiber (PRF) for 6 h at 30-60 °C, followed by curing and carbonization at 1000 °C [48]. Wang et al. employed porous CF-based

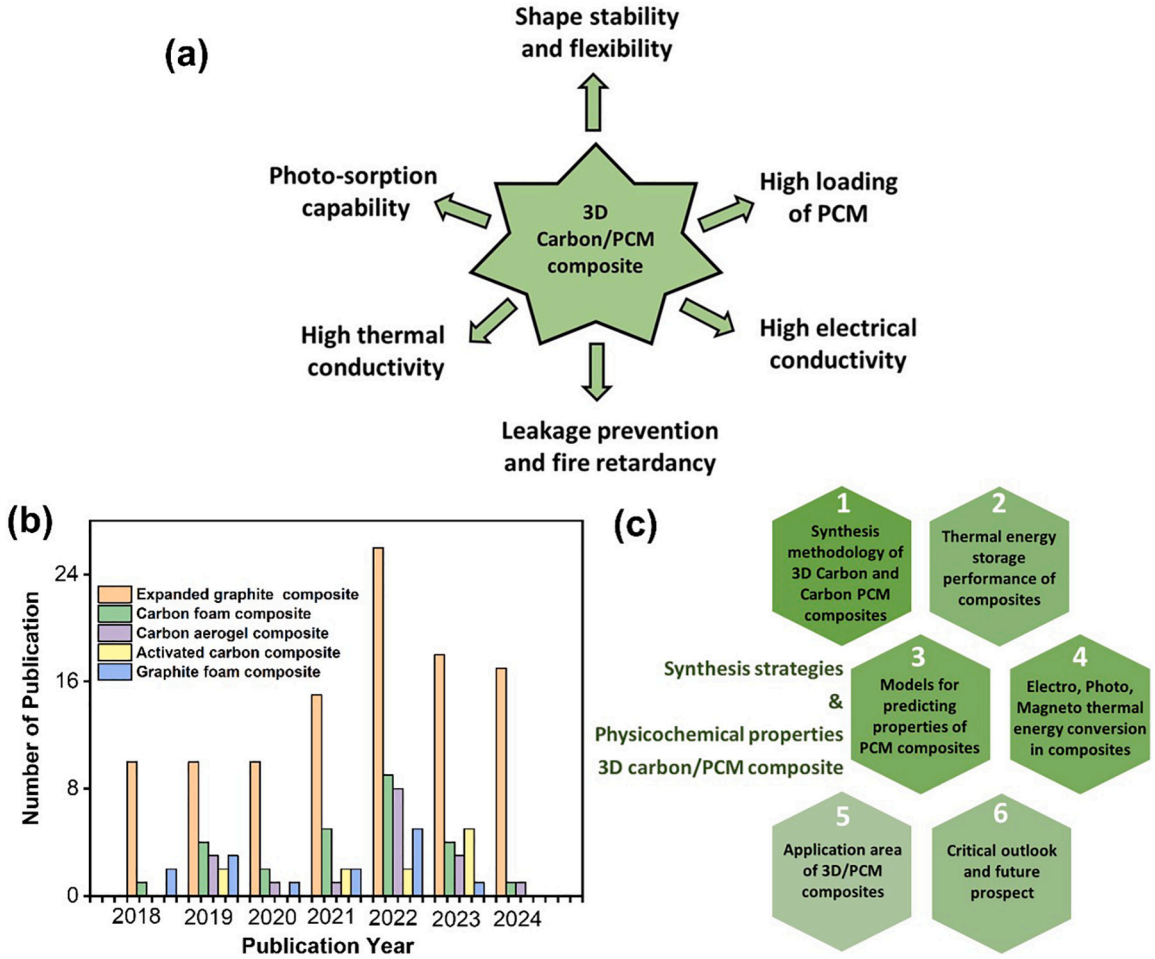

Fig. 1. (a) The general advantage of 3D carbon/PCM composite (b) The progress on 3D carbon-based composite for latent thermal energy storage (data obtained from Scopus search on 03.06.2024, Key hit: "EG/CF/CA/AC/GF based composites for latent thermal energy storage") (c) Outline of the proposed review indicating the main covered topic and the sequence of the sections.

PCM composite for LHTES application [49]. Here, porous CF was prepared via the templated replica method. Typically, copper oxide nanorods were deposited on Cu foam via oxidation reaction with ammonium persulfate and KOH. Then, an in-situ MOF (ZIF-67) structure formation on CuO foam was performed with 2-methylimidazole and cobalt nitrate as precursors. Finally, the carbonization reaction was carried out to prepare porous CF from ZIF-67/Cu foam structure, followed by vacuum impregnation with melted SA to obtain PCM composite, as presented in Fig. 2.

Wilson et al. prepared CF using three-carbon precursors, i.e., graphite, sucrose, glycerol, and intercalating agent (NaCl) via carbonization reaction at 750 °C for 2 h [50]. The presence of NaCl significantly increases the high porosity of CF with increased roughness that also affects the increased hydrophobicity of CF from 54° to 128° for the water contact angle. To compare the role of the microporous structure of CF, the authors also prepared the macro-porous composite using sucrose, graphite powder, and $Mg(NO_3)_2$ via the thermos-foaming procedure. Zhang et al. observed that the carbonization temperature significantly impacted the CF microstructure employed for the TES application [51]. The rise in the carbonization temperature substantially increases the porosity with enhanced void cells (%) of CF, as noticed by the authors. However, a very high carbonized temperature (1800 °C) significantly damaged the C-skeleton with the formation of an agglomerated structure. The high surface roughness of ultrathin-walled CF possesses significant hydrophobicity compared to pristine CF.

Jana et al. fabricated superhydrophobic CF from suspended graphite flake and sucrose precursor for seasonal solar thermal energy storage application [52]. The mixture was heated at 120 °C for 2 days during polycondensation of sucrose and release of water molecules. The rigid foam was then carbonized at 900 °C to obtain porous CF. The direct fluorination of CF using fluorinated organic compound formation of silane group at the surface of carbon was performed via the sol-gel process in the presence of silica, grafting of perfluoroalkyl chain, or attachment of fluorinated organic moiety via reduction of diazonium salt are the primary strategy to obtain hydrophobic CF. Ola et al. employed this method to fabricate CF/GNP-based 3D carbon for thermal management applications [53]. Carbon foam was utilized to support PCM as a 3D support to form interconnected hierarchical 3D architecture, which provokes the high loading of PCM with an efficient heat transfer pathway. In conjugation, graphene nanoplatelets were used as an additional 2D carbon support to decrease the thermal resistance between the CF macropores and create an additional heat transfer pathway between PCM and CF. Thermal conductivity is an essential quick-check parameter to analyze the status of the composite for thermal energy storage. The author also observed that the carbonization temperature and graphitization degree had a powerful effect on the improved thermal conductivity of the composite. In contrast, a high loading of GNP in the composite might not be an excellent strategy to increase the thermal conductivity of the composite.

2.2.2. CVD method

Recently, Cheng et al. adopted a unique strategy to fabricate a 3D

Table 1
A comparison study between our proposed review and recently published review articles in this field.

No	Year	Title of the Topics	The focus of the review	Ref
1	2020	Recent advances of polymeric phase change composites for flexible electronics and thermal energy storage system	• Overview of polymeric PCMs. • Overview of different modification strategies and applications.	[39]
2	2019	Graphene-based phase change composites for energy harvesting and storage: State of the art and prospects	• Overview of different PCM composite performances for thermal energy harvesting and storage. • Graphene-based allotropes are the central theme of this review.	[36]
3	2021	Preparation and application of a three-dimensional filler network towards organic phase change materials with high performance and multi-functions	• Overview of the fabrication strategies of 3D-organic PCM composites. • The composite's thermal energy storage, management, and conversion efficacy is discussed.	[40]
4	2022	Carbon-Based Composite Phase Change Materials for Thermal Energy Storage, Transfer, and Conversion	• Overview of the fabrication of different carbon-based composites. • Fundamentals of thermal energy transport and storage mechanism, • Discussion on the performance of the composite towards energy storage and conversion.	[8]
5	2022	Phase change material infiltrated 3D porous carbon interconnected composites for thermal energy storage.	• Discussion on the fabrication, thermal properties, and possible application of 3D porous carbon/PCM composite • CNT, carbon aerogel, graphene, graphite, biomass-derived carbon, and graphite foam-based composite are the central themes of the review.	[41]
6	2022	An overview on the use of additives and preparation procedure in phase change materials for thermal energy storage with a focus on long term applications	• The discussion on the effect of CNT, CNF, EG, graphene nanoplatelet in PCM materials towards the improvement of thermophysical attributes of the composite • Three necessary PCM composite preparation procedures were mentioned here, i.e., magnetic stirring, ultrasonication, and a combination of both. • The characteristics of sugar alcohol, Sodium Acetate Trihydrate (SAT) based PCM, and solid-solid PCM towards thermal energy storage efficacy was discussed. • A detailed description of the prototypes based on SAT for the TES application	[15]
8	2024	Thermally Conducting 3D Carbon based Phase Change Composites: A Review on Progress in Fabrication Strategies, Categories, Thermal Energy Storage-Conversion Efficacy, Numerical Models and Applications	• Discussion on the fabrication strategies of different 3D carbon (EG, GF, ExFG, CF, CA, other 3D carbon) and PCM infiltration process. • Discussion on the effect of different 3D carbon on the morphological attributes and thermal energy storage attributes of 3D carbon/PCM composite. • Different prototypes and simulation studies are discussed to co-relate the theoretical and experimental findings. • The various application areas based on such composites are also highlighted. • The critical outlook and prospects in this field are also discussed.	This review

Carbon fiber/CNT architecture-for high loading of PCM [54]. CNTs were grown on cleaned Carbon fiber via the CVD method in the presence of Co$(NO_3)_2$ and Fe$(NO_3)_2$ catalyst solution at 550-660 °C under N_2 and C_2H_2 flow. The observed wide pore distribution entirely depends on the applied synthesis temperature and the high annealing temperature that facilitates the homogeneous growth of CNT on Carbon fiber. Significantly, the formation of homogeneous 3D hierarchical architecture with improved porous geometry triggers efficient PCM adsorption and helps thermal transport between CF using CNT as a heat transport linker. Kholmanov et al. utilized ultrathin graphene foam (UGF)/CNT architecture for TES application [55]. Ultrathin graphene was grown on a Ni template using the CVD method. Next, the coating of the Fe catalyst was applied through the e-beam evaporation. An Al buffer layer was employed on top of this layer to grow CNT via a catalytic CVD process, see Fig. 3. Finally, oxygen plasma was applied to create void pores and defects that facilitate high PCM loading. Interestingly, ultrathin graphene foam and CNT enhanced the thermal conductivity of pure erythritol by 3 and 5 times higher, respectively.

Furthermore, the new architecture fabricated by the authors mitigates the thermal resistance issues of the composite, which can significantly decrease the surface-to-area ratio of UGF and increase contact resistance at the PCM-UGF junction. Both such parameters can remarkably change the thermal energy storage efficacy of the composite.

2.3. CA and its modified carbon skeleton

CA is generally fabricated via the consecutive three-step approaches associated with the polymerization of organic molecules, drying (supercritical drying, freeze drying, pressure drying), and carbonization/physical or chemical activation at high temperature (773–2773 K) under inert atmosphere [56]. Graphitic materials-based carbon aerogel is prepared via the sol-gel, template, spacer support, self-support, and substrate-based methods using carbon nanotube (CNT), graphene, carbide, and carbonitride-based precursors. The carbonization/physical or chemical activation (under the influence of a pore-forming agent, gaseous agent, or high temperature) step is the final step that governs the porosity and mechanical attributes of carbon aerogel [56].

2.3.1. Ice-templated method

In this process, the 3D-oriented structure of carbon is grown using ice as a template, followed by the freeze-drying process. Such a process easily achieves high thermal conductivity through the in-plane direction of the oriented 3D carbon. For example, Yang et al. fabricated 3D-oriented GO/boron nitride (BN) porous scaffold-based composites with

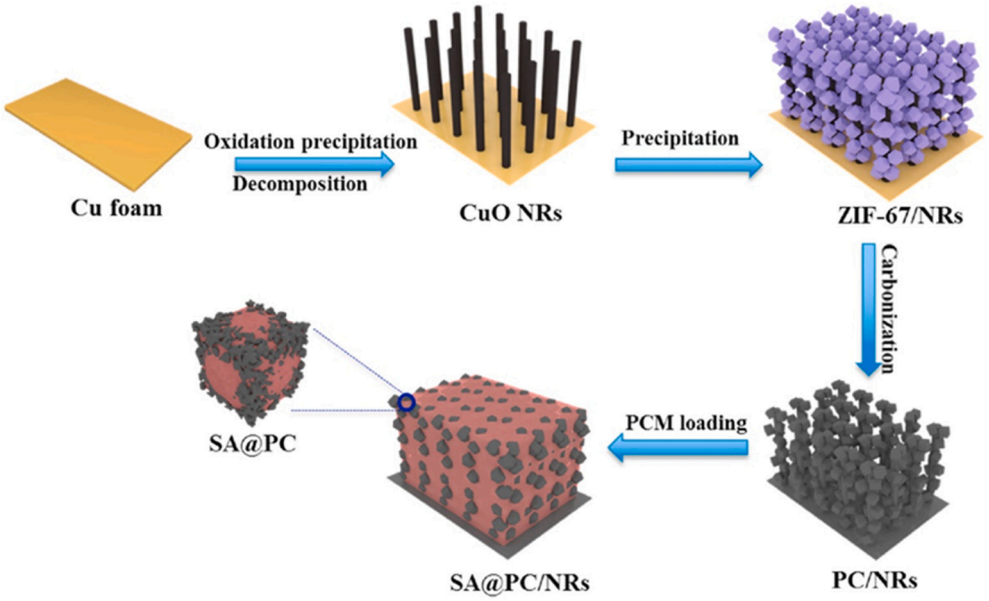

Fig. 2. The synthesis strategy of porous CF and SA@PC/NR composite [49].

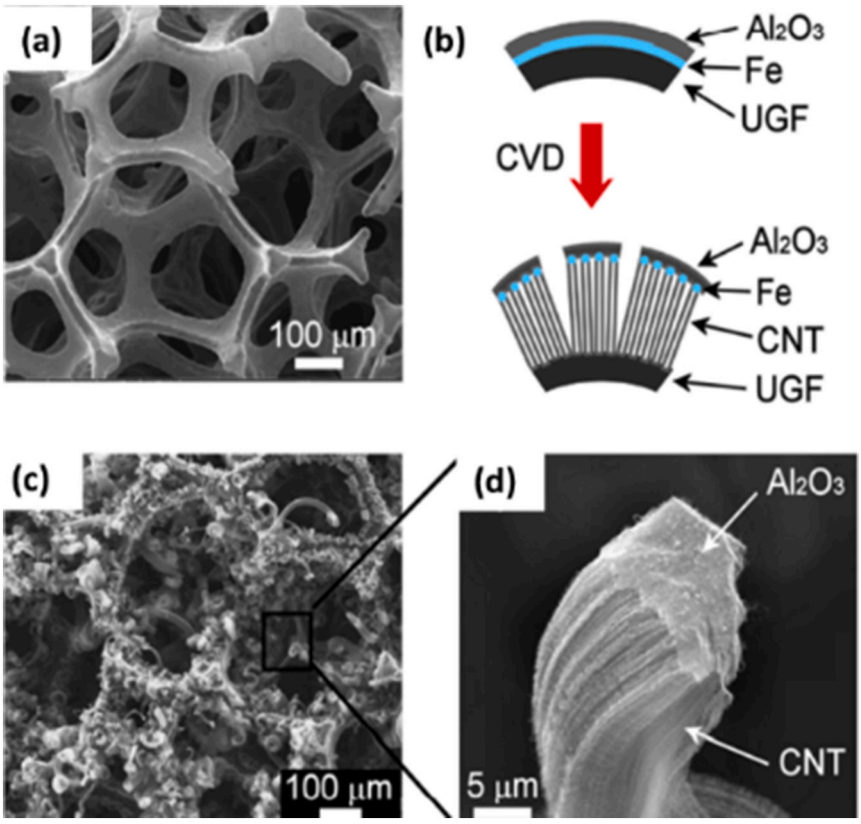

Fig. 3. (a-d) The typical architecture of UGF-CNT composite and pristine counterpart [55].

high thermal conductivity via such a process [57].

2.3.2. The combination of freeze-drying and carbonization/carbonization process

In 2023, Luo et al. fabricated highly aligned N-doped carbon aerogel/PEG composite for battery thermal management [58]. A directional freeze-drying method and carbonization process were adopted to obtain N-doped carbon aerogel. A sodium alginate monolith was prepared by mixing it with sodium alginate and ammonium chloride and adding a calcium chloride aqueous solution. The freeze-drying process of the mixture for 2 days was the final step to obtain the sodium alginate monolith. The monolith was calcined at 700 °C for 2 h. The presence of Ca ions facilitates the bond formation with alginate molecules to construct a 3D network structure. Ammonium chloride plays a dual role in the construction of N-doped aerogel. It acts as a pore-forming agent during the calcination process. The formation of different nitrogenous

species during its decomposition acts as a dopant to create an N-doped aerogel structure. The authors found that the surface area and porosity profile of aligned N-doped carbon was increased compared to non-nitrogen-doped carbon aerogel. The directional orientation of carbon architecture and the presence of a pore-forming agent is responsible for such observation.

Song et al. utilized kapok fiber aerogel for solar/magnetic to thermal energy storage applications [59]. To prepare CKF/Fe_3O_4 composite, the carbon fiber was immersed in dopamine/Tis-HCl buffer solution dispersion (2 gL^{-1}, pH = 8.5), followed by adding and stirring $FeCl_3$ solution. The obtained modified fiber was vacuum-filtrated and carbonized under argon flow. Zou et al. utilized natural resources, like pumpkins or carrots, to fabricate CA via the carbonization route at the operating temperature of 800 °C or 1000 °C [60]. The authors incorporated thiol-ene resin moiety into CA architecture to prevent PCM leakage during synthesis.

2.3.3. Chemical crosslinking

Zhang et al. employed 98 fiber/sodium alginate aerogel to create a stable, highly thermally conductive PEG- based composite [61]. Kapok fiber/BN aerogel was prepared via ultrasonication and stirring in the presence of oxidized kapok fiber, hydroxylated BN, and sodium alginate. Calcium chloride was utilized as a crosslinking agent. An extensive crosslinking was processed between the polyhydroxy compound (sodium alginate), oxidized kapok fiber, and hydroxylated boron nitride to create a 3D porous architecture. The idea of 3D aerogel formation between kapok fiber and BN arises from their potential beneficial attributes for TES application. Kapok fiber is a rich source of cellulose that possesses excellent mechanical stability, while BN is a good filler to enhance thermal conductivity in the composite.

2.3.4. The combination of hydrothermal and freeze-drying process

Kong et al. utilized large-size 3D graphene aerogel to load paraffin to revamp the thermophysical attributes of PCM [62]. Ultra-large graphene was prepared from GO slurry via hydrothermal and freeze-drying process followed by carbonization at 2800 °C. Ethylenediamine was used to link the adjacent graphite sheets through amide bond formation to fabricate large-size graphene aerogel. The same protocol was followed to prepare graphene aerogel without EDA to compare the effect of large-size graphene aerogel.

2.3.5. Sol-gel process

Du et al. fabricated a novel strategy to fabricate porous CA via a sol-gel process for TES management [63]. Here, nano-fibrillated cellulose and MWCNT were used as carbon precursors for the fabrication of CA. The alkylation of cellulose aerogel was accompanied by different acid

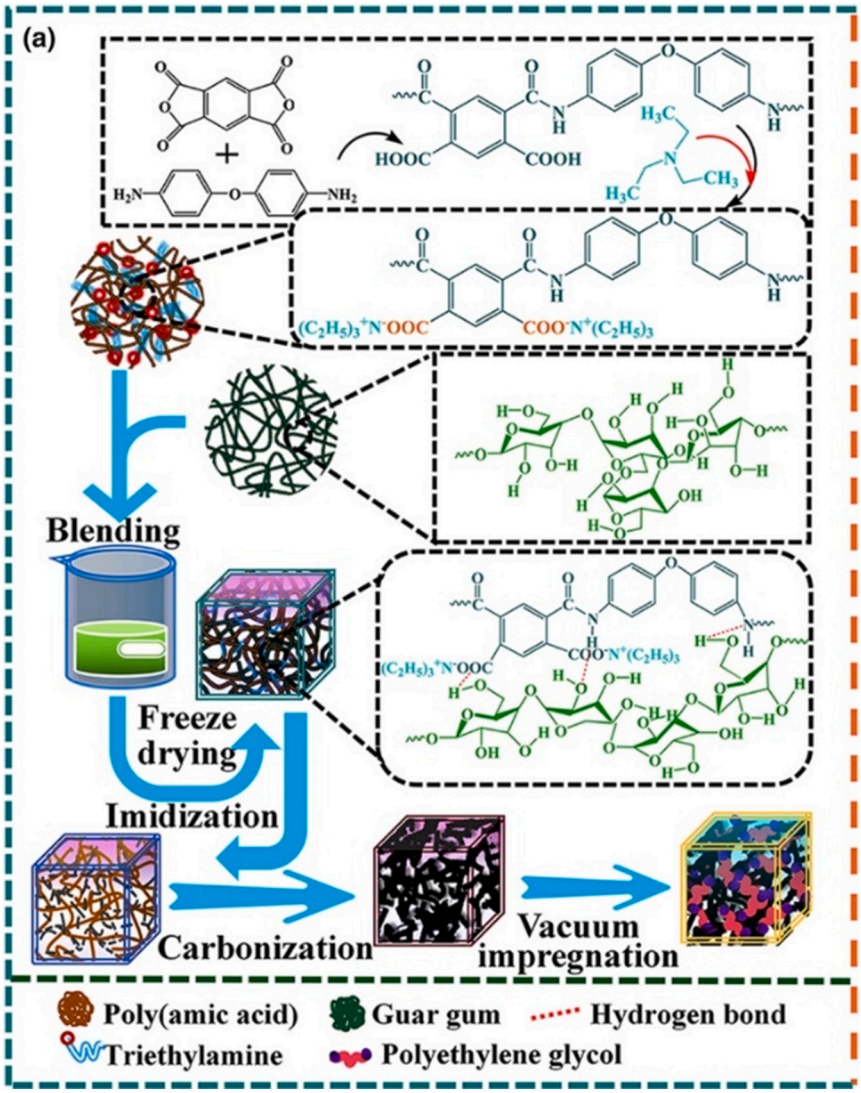

Fig. 4. The preparation process of mechanically stable guargum/poly(amic acid) aerogel PCM composite [64].

chlorides (hexanoyl chloride, lauroyl chloride, stearoyl chloride) and triethylamine. The smooth surface texture was apparent for surface-treated cellulose aerogel composite compared to untreated cellulose composite. The XPS spectroscopic result further corroborated the successful functionalization of the cellulose surface. The CO_x/C_a, peak intensity ratio, was higher for stearoyl chloride-treated cellulose composite than others, indicating increased aliphatic chains on the cellulose surface. Zhang et al. took advantage of the flexibility of guar gum and the mechanical stiffness of PI-derived carbon to construct and fabricate mechanically stable and flexible carbon aerogel via an environment-friendly, cost-effective strategy, followed by vacuum impregnation of PEG [64]; see Fig. 4. Wang et al. observed that the mechanical flexibility and strength of the graphene aerogel-based composite were lower than that of the CNT/graphene aerogel-based composite [65]. The effective transfer of applied force from loosely bound graphitic structure to CNT remarkably prevents the tilting of graphitic layers, hence preventing compression deformation.

2.3.6. Chemical reduction and wet spinning

Li et al. adopted the combination of chemical reduction of GO by vitamin C/HCl solution and wet-spinning (12 h, 50 °C) strategy to fabricate graphene aerogel fiber. Almost 84 % PEG incorporation in the presence of such newly developed carbonaceous architecture was reported by the researchers [66].

2.4. Porous carbon and its modified carbon skeleton

Yang et al. utilized wood as a natural resource to fabricate carbonized wood based PCM composite [67]. Interestingly, the carbonization of poplar wood significantly enhances the surface area and volume of the pores. Lv et al. (2023) adopted a unique approach to fabricating yeast-derived porous carbon-based PCM composite [68]. To achieve high PCM loading, porous yeast carbon was prepared from yeast powder via hydrothermal carbonization, followed by in situ growth of metal-organic framework (ZIF-8) and carbonization at 980 °C at 4 h. The carbonization of MOF can offer additional porous 3D architecture to the system, which facilitates better loading of PCM and improves thermal energy storage efficacy. Luo et al. designed an N-doped porous carbon from a metal oxide framework (MOF) in the presence of EG via a carbonization reaction under an N_2 atmosphere [69]. Here, nitrogen-doped carbon was grown between EG sheets, followed by carbonization, which enhanced the porosity and surface area in the final composite. Zhou et al. employed 3D activated carbon to fabricate a PEG-based composite for LHTES application [70]. The high carbonization temperature induces a high degree of porosity due to the corrosion power of KOH. However, it reduced the surface area of the composite from 2310.1 to 950.9 m^2g^{-1}. Nicholas et al. investigated the effect of porosity and surface area of AC on the LHTES efficacy of n-octadecane/AC-based composite [71]. It was apparent that with an increase in activating agent concentration, the surface area, pore size, and volume of AC increased.

2.5. Supplementary carbon skeleton

Apart from different conventional synthesis processes of 3D carbon, the researchers started to prepare a wide variety of supplementary 3D carbon to tune the surface area and pore geometry and introduce the surface functionality to revamp the active sites of 3D carbon.

2.5.1. The combination of carbonization and wet chemical method

Li et al. prepared GO/MOF-based 3D skeleton for high loading of PCM. GO-MOF composite was synthesized via a wet chemical method using zinc nitrate and phthalic acid as precursors of MOF in the presence of GO, followed by carbonization to induce porosity in the 3D architecture. The porous architecture arising from MOF and the high surface area of rGO along inter-connection between the conductive particles facilitate high PCM loading with enhanced thermal conductivity [72].

2.5.2. Covalent linking or the combination of crosslinking and wet-chemical method

Liu et al. designed a 3D hierarchical network structure of MWCNT by linking with melamine foam through azide polyacrylic acid as a linker [73]. These new design of synthesis strategies, especially the strong linking between melamine foam, CNT, and TD, offer low interfacial thermal resistance with enhanced thermal conductivity through the formation of the zig-zag pathway between melamine foam and CNTs of the materials along with high loading (%) of PCM. In 2022, Wu et al. adopted a dual encapsulation strategy to fabricate a 3D carbon-based PEG composite to mitigate low thermal conductivity and PCM leakage problems from the composite structure [74]. Crosslinked PU foam was first manufactured via crosslinking between PEG and HDIB in DMF solvent under mechanical agitation at 60 °C under N_2 protection. The obtained PU foam was then infiltrated with PEG solution via adsorption followed by vacuum distillation to remove residual solvent. To enhance the thermal conductivity of the composite, the PU/PEG composite was first fragmented with a freeze-pulverization process, and the obtained particles were mixed with EG under mechanical agitation at 120 °C to absorb liquid-free PEG into the EG matrix. Then, it was compressed to form a stable composite at 60 °C under a maximum of 20 MPa pressure, see Fig. 5a-b.

3. PCM infiltration strategies for the fabrication of 3D carbon/PCM composite

The thermophysical attributes of carbon-based PCM composites strongly depend on the loading, homogeneous distribution of PCM in carbon media, and the contact between 3D carbon and PCM. The research community has adopted various protocols to fabricate 3D carbon/PCM composites.

3.1. Vacuum impregnation and its associated modified method

Vacuum impregnation, a well-known popular strategy, offers an improved synergy between 3D carbon and PCM composites. Typically, this process exploits a pressurized vacuum environment to evacuate the air from the internal pores of 3D carbon, followed by infiltration of pre-melted or in situ melted PCM into the interior architecture of 3D carbon. To improve the homogeneous distribution of PCM inside 3D carbon, the researchers adopted the combination of vacuum impregnation and blending, melt blending, and ultrasonication, see the schematics in Fig. 6a. In such a process, before the vacuum impregnation process, 3D carbons and PCM are mixed under mechanical agitation or ultrasonic irradiation either at RT or the melting temperature of PCM. Vacuum impregnation offers the maximum loading of PCM into the worm-like pores and inter-layer spaces of the EG. For example, in 2020, Wang et al. adopted a vacuum impregnation strategy to prepare EG/paraffin composite at 130 °C under 0.1 Pa for 60 min [75]. Like EG/organic PCM-based composites, EG-embedded inorganic PCM composite has also emerged as a potential candidate for thermal energy storage applications. Among different inorganic PCMs utilized for LHTES application, salt hydrate is the most well-known appealing material owing to its high storage density and inflated thermal conductivity. However, the phase segregation and immediate cooling effect limit its potential application. Incorporating EG into such PCM mitigates issues, forming a form-stable composite without leakage. EG/PCM-based composites are powder in nature; therefore, to impart the composite structure's shape-stability, the researchers generally adopt the sintering-compressing technique after vacuum infiltration to obtain form-stable EG composite. Typically, mixing EG and inorganic PCM in a suitable solvent or melted PCM at elevated temperature under magnetic agitation is adopted for the impregnation process. The resulting mixture was heated at an elevated temperature for complete calcination for the pre-sintering operation. In

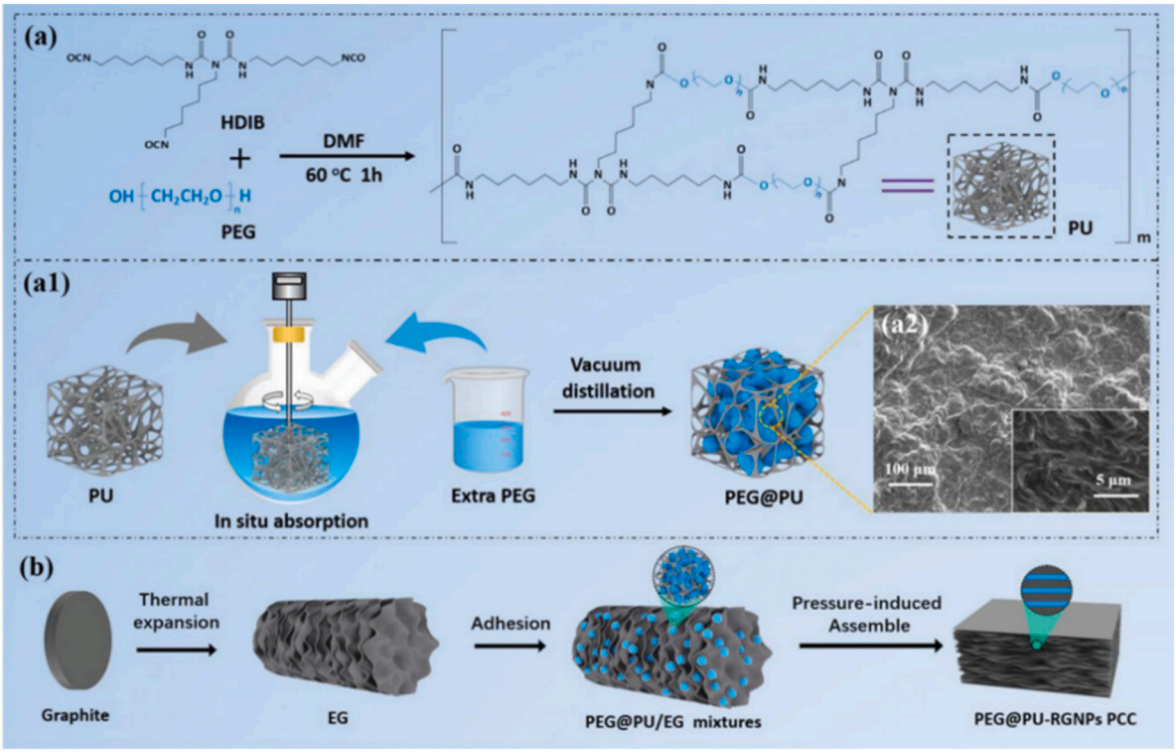

Fig. 5. (a-b) The synthesis strategy of highly conductive and liquid-free PEG-based polyurethane/graphite nanoplatelets hybrid networks [74].

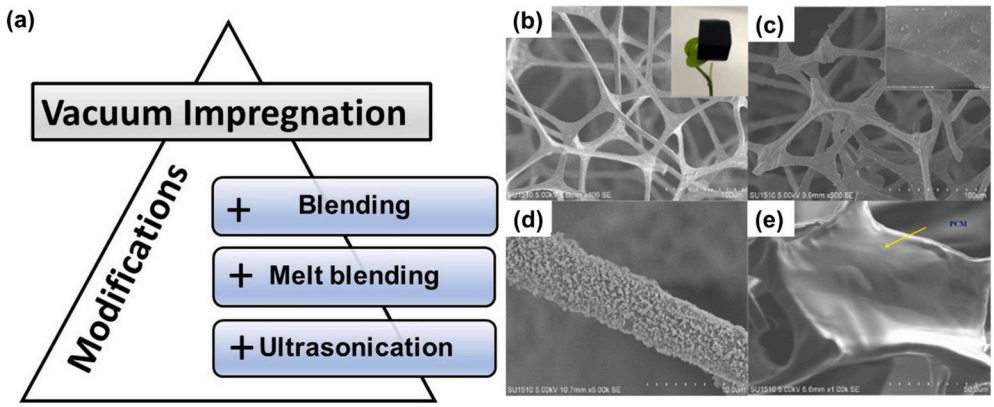

Fig. 6. (a) The classification of modified Vacuum impregnation process, (b-e) The SEM micrograph of Ti_2O_3/CF/PCM (n-eicosane)/polydopamine composite with pristine components [77].

the 2nd step, the obtained calcined mixture is compressed into a disc and then sintered at high temperatures or a step-by-step increase in temperature for a definite period. A step-by-step increase in sintering temperature is beneficial to restraining the composites' chemical composition, as Ren et al. observed in their study [76]. The absence of additional XRD peaks before and after sintering without changing the position of the peak confirmed the non- change in the chemical composition of the composite.

Wang et al. fabricated Ti_2O_3/CF/PCM (n-eicosane)/polydopamine composite via the same strategy [77]. From the SEM image in Fig. 6b-e, it was observed that the morphology of the network-like porous microstructure of CF/PDA changed to a rough surface texture-like microstructure. With the further addition of PCM, the smooth surface was changed to a rugged surface due to the presence of PCM at the Ti surface. In 2018, Li et al. fabricated Co_3O_4/EG/SA composite via in-situ deposition and vacuum impregnation [78]. From the SEM image, it was apparent that the three components of the composite were in close contact with each other, where the porous network microstructure of EG and cobalt oxide may trigger efficient heat transmission throughout the composite structure. 3D carbon foam has been broadly studied as a supporting carbon skeleton to enfold PCM due to its attractive porous architecture and alterable thermal and electrical conductivity [79]. Maleki et al. fabricated three different PCM-based CF composites for latent energy storage from solar light via vacuum infiltration at 60 °C and 70 °C, 80 °C for PEG, paraffin, and palmitic acid-based composites, respectively [80]. The crystalline arrangement was preserved after infiltration into CF, as observed from the XRD analysis. Interestingly, the infiltration of PCM into CF significantly influenced the crystallite size and peak intensity of pure PCM, especially for palmitic acid, due to improved confinement and solid physical adhesion. However, the

reverse phenomenon was apparent for the paraffin/CF composite. Wilson et al. also employed the same methodology to conduct conducting macro and microporous CF/paraffin wax composite [50]. A significant leakage within 30 min was found for macro-porous CF/PCM composite rather than microporous CF/paraffin composite. The larger pore size of macro-cellular CF is responsible for such leakage than microcellular CF.

Lan et al. did not follow the hard-core conventional strategy to prepare the composite [81]. However, their research group followed a modified process consisting of vacuum and pressure-mediated processes. Dynalene MS-XTT, a typical chloride salt blend, was utilized as an inorganic PCM with long-term stability and anti-corrosion attributes. The authors developed one infiltration chamber for this purpose. Typically, PCM powder was loaded onto the top of GF and placed in the infiltration chamber. For heating, the device was inducted into the oven. At first, the air was removed from the chamber, and PCM was melted at 360 °C under a vacuum. After melting PCM, the pressure was introduced into the system via nitrogen purging to force PCM to be successfully incorporated into GF. These two cycles continued until the complete impregnation took place. The infiltration efficiency of this process was found to be 93 %. The authors also reported a remarkable enhancement in thermal conductivity of inorganic PCM infiltrated GF (101 $Wm^{-1} K^{-1}$) compared to pristine PCM (2 $Wm^{-1} K^{-1}$).

Zou et al. synthesized a novel shape stable PCM/CA composite for thermal energy storage applications [60]. The authors prepared a form stable PCM via crosslinking of 1,3-Divinyltetramethyldisiloxane, 2,2′-(Ethylenedioxy) diethanethiol, 1-Trimethylolpropane(3-mercaptopropionat) with dicumyl peroxide and palmitic acid. The composite was fabricated using the conventional vacuum impregnation method at 120 °C for 4 h with 0.1 bar pressure applied for 10 min. Kong et al. fabricated a large-size 3D graphene aerogel/paraffin-based composite by vacuum impregnation [62]. The pressure, temperature, and time duration of the vacuum impregnation process were 1.4 MPa, 90 °C, and 30 min, respectively. No air gap was found between large-sized graphene aerogel and paraffin, as observed from the SEM image, indicating efficient filling of PEG into the pores of the graphene sheets with successful preservation of the 3D architecture of graphene aerogel. However, few pores with several cracks were evident in small-sized graphene aerogel, and the successful coverage of paraffin in small graphene aerogel is apparent from the SEM micrograph. Carbonized wood-based PCM composite preparation was proposed by Yang et al. [67].

Additionally, PCM such as TD was impregnated into carbonized wood via conventional vacuum impregnation for 3 h, significantly enhancing the pores' size and number. The complete filling of TD by the inner pores of CW was observed compared to poplar wood because of the non-opening of the channels. The internal structure also reminds many keratin-based natural materials, having excellent thermal insulation and mechanical properties [82,83].

The critical parameter for revamping the thermal energy storage performance of PCM composite is strongly connected to the high loading of PCM. To reduce the homogeneous dispersion and distribution issues of fillers and PCM, Zhang et al. adopted the combination of VI, ultrasonication, and melt-blending/blending process in sequence to fabricate PCM composite [64]. This process is especially suitable for 3D carbon in a powder state [84] or additional carbon filler with 3D carbon-based foam in a PCM matrix [85]. The melt blending, and steam explosion processes are relatively new compared to conventional methods for creating thermal energy storage materials. A melt-blending approach is adopted for the homogeneous contact between carbon media and PCM, followed by treating the mixture under a hot stream, typically high temperature and pressure, for a definite period, and the mix was rapidly depressurized at ambient atmospheric pressure. The high temperature and sudden decompression cause the exfoliation of agglomerated carbon filler, thus enhancing the excellent dispersion stability of the composite structure. According to Bigdeli et al., additive size and Kapitza resistance significantly affect the thermal conductivity of the nano additive -based polymer composite, as predicted by the Reverse Non-equilibrium Molecular Dynamic (RNEMD) simulation study [86]. The size of the additive, especially in the sub-micrometer scale, can improve the thermal conductivity of the composite. Increased horizontal overlap between miscellaneous carbon additives, reduction of the average distance between carbon additives, or introduction of crosslinker between fillers can significantly revamp the thermal conductivity of the composite. This effect is even more prominent in the reported literature of Hu et al. during the investigation of the thermal conductivity of CNT/PW/EG composite [87]. Almost double thermal conductivity enhancement was evident for melt blending and steam explosion-treated samples compared to only melt blending-treated samples. The more homogeneous distribution of fillers creates a uniform, synergetic heat transfer pathway in this process, which is the main reason for the enhanced thermal conductivity of the composite.

3.2. Melt-blending/blending

Adsorption via melt blending or blending is another energy-efficient and straightforward strategy to fabricate different 3D carbon-based PCM composites. In the blending process, 3D carbon is mixed with PCM in a suitable solvent, followed by continuous stirring at room or elevated temperature for a long time to complete the successful adsorption of PCM by 3D carbon. On the contrary, the melting of PCM is performed before mixing it with 3D carbon or in-situ melting of PCM during the adsorption process. Wang et al. exploited this method to combine caprylic-nonanoic acid and EG via simple mixing and stirring for 16 h at room temperature [88]. The strong adsorption efficacy of EG facilitates the formation of the composite under magnetic agitation via capillary condensation. A maximum of 90 % loading of the caprylic-nonanoic acid mixture into EG architecture was reported. However, EG is associated with low stability of porous structures due to the quantization of high energy [75], which limits the development of high-performance materials. Micro-encapsulating organic PCM by polymer composite is a relevant and promising approach to preventing PCM leakage during phase transition. However, the polymer coating poses low thermal conductivity and may be stimulated by EG. Zhang et al. proposed the synthesis procedure of n-octadecane/EG/PS-based composites for TES application [89]. Typical refluxing of the mixture consisting of PS, EG, and n-octadecane at 100 °C for 10 h, followed by solvent evaporation at 120 °C, yields the composite. The superior non-leakage property of the stable composite was revealed even after heating above the melting temperature of PCM. Among different inorganic PCMs utilized for LHTES application, salt hydrate has high storage density and inflated thermal conductivity. However, the phase segregation and immediate cooling effect limit its potential application. EG into such PCM mitigates such issues by forming a form-stable composite with no leakage, fabricated via mixing and adsorption methods at a suitable temperature and impregnation time [90,91]. The melt blending or blending process is also ideal for homogeneous dispersion of different organic-inorganic carbon additives and polymers before infiltration of PCM [92].

Li et al. adopted a mechano-chemical agitation strategy was adopted here to fabricate an SA-filled 3D carbon composite in the presence of an ethanolic solution of SA with different weight percentage ratios from 40 % to 90 % [72]. Interestingly, it was evident that the specific surface area (2726.9 m^2g^{-1}), pore volume, and pore diameter of the rGO/MOF composite were remarkably enhanced for carbonized MOF support. The leak maximum filling of SA into the composite structure was up to 90 %. In 2021, Wu et al. infiltrated PU foam with PEG solution via adsorption followed by vacuum distillation to remove residual solvent [74]. The final weight loss of PEG@PU, 10 %, 20 %, and 30 % PEG@PU loaded 3D compressed composite was 3.1 %, 0.6 %, 0.15 %, 0.09 %, respectively, signifying the successful entrapment of PEG with no leakage in the consolidated composite structure compared to pristine PU@PEG, see Fig. 7a-b. To improve PCM loading into the composite structure with a straightforward and low energy consumption strategy, the soaking process is designed to fabricate a 3D carbon/PCM-based composite. 3D

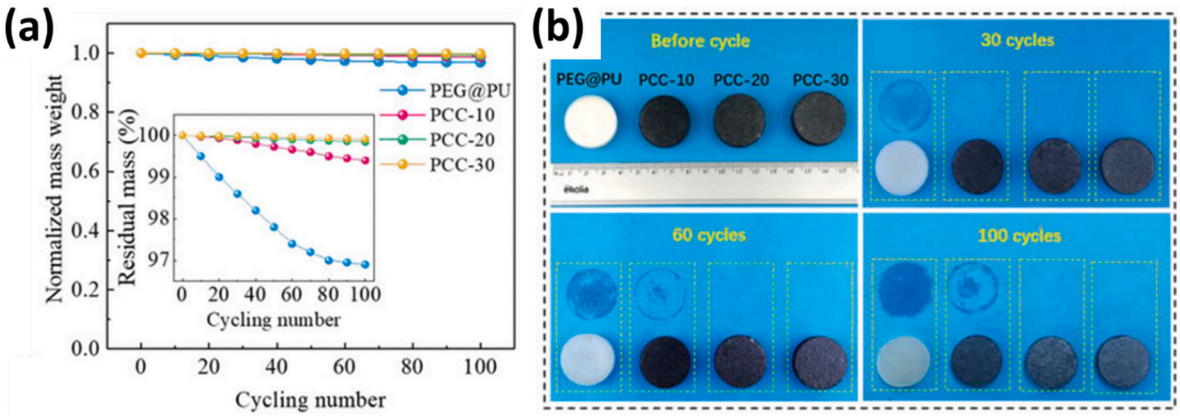

Fig. 7. (a-b) The synthesis strategy of highly conductive and liquid-free PEG-based polyurethane/graphite nanoplatelets hybrid networks (c) The weight loss of PEG@PU and PEG@PU- polyurethane/graphite nanoplatelets hybrid networks based at different cycling times. d) The digital picture of PEG@PU(10-30 %) loaded polyurethane/graphite nanoplatelets hybrid networks during 100 thermal cycling tests [74].

carbon is introduced into melted PCM, followed by the adsorption of PCM by the porous structure of 3D carbon through capillary action under normal atmospheric pressure. Wang et al. fabricated (1- hexadecyl amine) (HDA) and 1-tetradecyl amine (TDA)/graphene or all CA-based ultra-lightweight composite by the above-said methodology [65]. The impregnation was carried out by soaking melted PCM. Wang et al. also utilized this methodology for the efficient adsorption of PEG by epoxy resin moiety [93].

3.3. Hydrothermal treatment

The rapid assembly of organic PCM into the pores of EG under high pressure and temperature (hydrothermal synthesis) is another strategy for developing high-performance materials. For example, Zeng et al. fabricated TD/EG composite by exploiting the above-said approach [94]. The high loading of PCM (~80-85 wt.%) into EG, along with high thermal conductivity (5.71 W m^{-1} K^{-1}), could be achieved by this methodology.

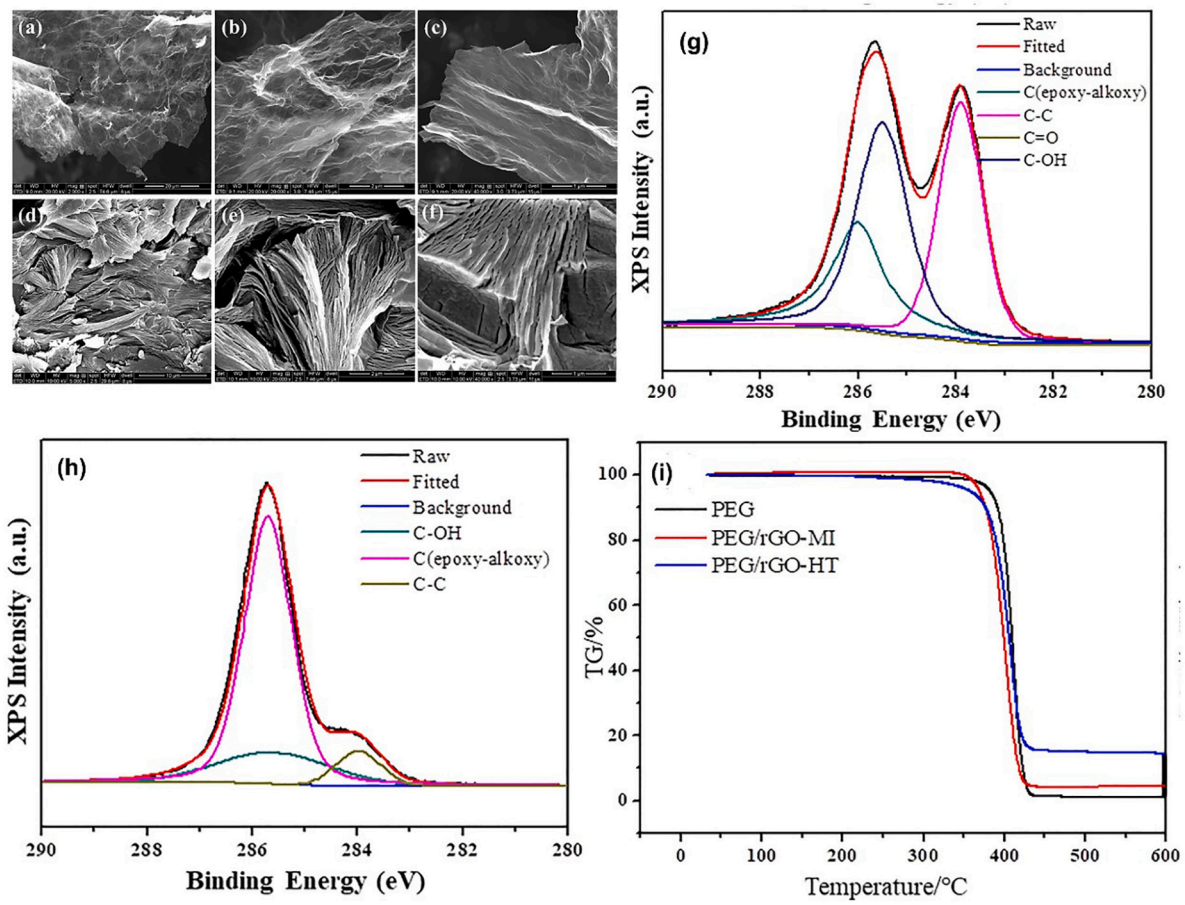

Fig. 8. (a-f) SEM images of PEG/rGO-HT and PEG/rGO-MI samples with different magnification (g-h) XPS spectrum of PEG/rGO-HT and PEG/rGO-MI samples (i) TGA curve of PEG, PEG/rGO-HT and PEG/rGO-MI samples [95].

3.4. Hydrothermal and vacuum impregnation strategy: a comparative approach

Ding et al. adopted two strategies to fabricate the 3D rGO aerogel-based composites to investigate the energy storage efficacy of the composite [95]. Primarily, the authors divided the synthesis strategy into two parts: (a) Hydrothermal strategy for simultaneous reduction of GO along with forming PCM/rGO aerogel composite and (b) chemical reduction of GO followed by vacuum impregnation of PCM. In the former process, an aqueous mixture of CTAC, GO, and PEG was subjected to hydrothermal treatment with in-situ thermal reduction of PEG. Later, after the chemical reduction of GO in the presence of ascorbic acid, the filling of rGO pores by PEG was carried out via a vacuum impregnation process. A more disordered arrangement of rGO sheets was observed for the first process due to the forming a more compact interface between PEG and rGO aerogel. During the hydrothermal procedure, the PEG molecules were inserted into the aerogel pores in the presence of surfactant, which reduces the surface tension between graphite sheets and the interface between PEG and graphite sheets. Later, PEG was adsorbed at the scutum of the graphite sheets, forming a smoother, ordered structure due to capillary action and hydrogen bonding, see Fig. 8a-f. It was observed that the C/O atomic ratio at the surface was increased from 2.03 % to 3.1 % for the composite prepared by the hydrothermal process, which signifies increased graphitization with the successive enhancement of C═O and C-OH groups, see Fig. 8 g-h. The result indicates strong bonding between PEG and graphitic pores of RGO gel. The mass loss occurred from 360 °C to 432 °C due to the presence of PEG, as apparent from the TGA curve see Fig. 8i. After the heating experiment, the final weight of the composite prepared by the 1st and 2nd processes was 15.3 % and 4.3 %. The result signifies the presence of 85.6 % and 96.6 % PEG in the composite structure, so up to 96.6 % PEG loading is possible with this synthesis methodology; the complete graphitization process and high PEG loading directly affect the thermal conductivity and latent enthalpy storage efficacy that we discussed later.

3.5. Core-shell/micro-encapsulation

Cast-molding-assisted micro-encapsulation strategy is a relatively new theme in preparing micro-encapsulated 3D carbon/PCM composites. In this process, PCM and 3D carbon dispersion are typically placed in the inner and outer parts of a specifically shaped core-shell mold. Finally, cast-mold microencapsulated PCM composite is obtained by heat treatment. Yu et al. fabricated octadecanol encapsulated nano copper silicon or eutectic inorganic alloy/EG composite macro-capsule [96]. octadecanol was impregnated into EG by suction treatment to form a hybrid composite. The eutectic $Bi_{31.6}In_{48.8}Sn_{19.6}$ alloy (EBiInSn) and EG were mixed with Ecoflex00-30 A and Ecoflex00-30 B separately at elevated temperature followed by mixing vacuum drying to obtain silicone elastomer shell composite. The authors used cast molding to prepare core-shell PCM/EG capsules. Mold 1 consists of octadecanol composite, which acts as a core. The core was incorporated into mold 2 with a silicon composite gasket, which was molded previously. The liquid silicon composite, which acts as a shell, was injected into mold 2. In the final stage, the microcapsule was obtained after curing at 50 °C. The detailed synthesis process is shown in Fig. 9a-d. The low melting alloy induced more latent heat storage and high heat conductivity. Thanks to the high concentration and adherence attributes of silicon elastomer, it also prevents the precipitation effect of eutectic alloys. The coating of PCM with an inorganic body and the addition of EG as an organic conducting filler are other options for fabricating microcapsule-based EG composite, as suggested by Wang et al. [97]. They manufactured paraffin/$CaCO_3$ core-shell microcapsule through self-assembly and added EG through compression. This strategy is the combination of three consecutive steps. 1st step: in this stage, paraffin was added to an aqueous surfactant solution to form paraffin micelle. 2nd step (self-assembly): calcium chloride was added to the solution. The positive charge of the calcium ion slowly interacts with the SO_3^- ion of the surfactant, forming a calcium ion-assembled paraffin micelle. Next, calcium was precipitated as $CaCO_3$ at the surface of PCM in the presence of Na_2CO_3. 3rd step (dry mixing stage): in this stage, EG was mixed with the obtained residue and compressed to form a block composite.

The high aspect ratio of core-shell PCM offers a high heat transfer area in the presence of EG, resulting in the fast promotion of heat through the structure. However, forming pores between EG and core-shell PCM due to the surface tension mismatch between two entities during the compression process may lead to high thermal resistance.

3.6. Combined approach

3.6.1. The combination of ultrasonication and melt blending/stirring process

The combination of melt blending and ultrasonication in the sequence is another methodology to ameliorate the homogeneous distribution of 3D carbon in solution and uniform filling of PCM into the internal pores of 3D carbon. Fang et al. exploited this strategy to create a

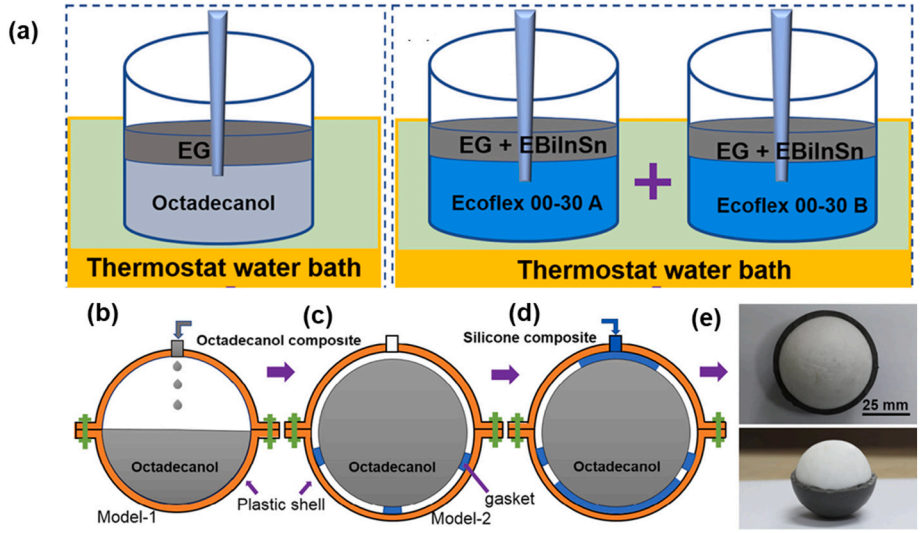

Fig. 9. (a) The schematic diagram of the preparation process EG-octadecanol composite, and EBiInSn-silicone-EG composite (b-e) The design architecture of core-shell-like mold for octadecanol encapsulated silicon elastomer/EG composite macro-capsule along with the schematic picture [96].

paraffin/EG composite [98]. Typically, in this process, after blending melted PCM and EG, the mixture was ultrasonicated, followed by stirring and cooling the mixture to form a compressed block. Here, EG consisted of flakes and rod-like, two distinct morphologies. The rods function as heat transfer junctions, while EG sheets help radiate the heat from one EG rod to another. This phenomenon is highly beneficial for a high amount of heat storage. Chriaa's research group also adopted a similar methodology for the preparation of styrene-b-(ethylene-co-butylene)-b-styrene (SEBS) tri-block copolymer/low-density polyethylene (LDPE)/EG/hexadecane-based composite for TES application [99]. The optimum loading of hexadecane arises in the presence of EG and polymer additives, facilitating the adsorption of PCM to form a stable composite under several heating cycles.

3.6.2. Ultrasonication followed by vacuum impregnation

Ultrasonication followed by VI is another strategy to obtain homogeneously distributed PCM in the powder-based 3D carbon. In this process, 3D carbon is added to melted PCM or PCM solution and ultrasonicated to obtain a homogeneous dispersion of PCM, followed by PCM impregnation under vacuum [100]. Interestingly, it is noted that most researchers prefer forming a compressed block of EG-based composite at the final stage, while this strategy was not observed for GF, CF, or CA-based composites. The above-said observation is due to the architectural stability of CF, GF, or CA-based PCM composite, mainly governed by the porous form stable structure of 3D carbon. However, enhanced structural stability of EG in the presence of PCM arises via the formation of a compressed block. At the same time, the vast, applied pressure during compact block formation provokes more interconnection between PCM molecules and EG molecules, resulting in the construction of more thermally conductive junctions along with better interconnection between PCM molecules.

3.6.3. Soaking, squeezing and vacuum impregnation: a comparative approach

Recently, Jing et al. investigated the effect of three different fabrication techniques, soaking, squeezing, and vacuum impregnation, see Fig. 10a, on CF/hydrated $CaCl_2$ composite's PCM impregnation efficiency. Interestingly, PCM loading efficiency, as seen in Fig. 10b, decreased with an increase in the carbonization degree of CF for the squeezing experiment. In contrast, consistent (>90 %) result was observed for the vacuum impregnation method. The distinct difference in outcome between the two processes may be accompanied by the combined effect of pressure difference during salt impregnation and decreased flexibility of CF with increased calcined temperature. However, a poor result was observed for the soaking process except for CF with a calcined temperature of 800 °C. As reported by the authors, the thermal conductivity of PCM was not improved by the presence of CF because of the open network structure of CF [101]. The typical benefits and drawbacks of different PCM infiltration procedures in 3D carbon are listed in Table 2.

Furthermore, an effort has been made to create a quick overview of the popularity of different PCM infiltration processes based on various literature reports, especially for the last 5 years. A closer look at Fig. 11 reveals that vacuum-impregnation and melt blending/blending are the two most popular methods to obtain 3D carbon/PCM composite. The main reason behind the popularity of the vacuum impregnation process for GF, CF, and CA-based composite lies in facile PCM adsorption inside the pores of the 3D carbon skeleton simply via capillary action. For EG/

Table 2
The benefit and drawback of different preparation methods of 3D carbon/PCM composite.

Type of Process	Advantage	Disadvantage
Vacuum Impregnation	• High loading of PCM • Minimum structural damage • High yield of production	• Homogeneous distribution of PCM issues • Only applicable for porous 3D carbon skeleton
Melt blending/blending	• Painless process • Easy control parameter • Facile Scale up	• Time consuming process • Agglomeration of 3D carbon
Melt blending/ blending+ Ultrasonication	• Homogeneous distribution of PCM • Painless and simple process • Less agglomeration of carbon media	• Often accompanied by the structural damage of carbon media
Ultrasonication+ Vacuum Impregnation	• High loading of PCM • Homogeneous distribution of PCM • Less agglomeration of carbon media	• Often accompanies by the structural damage of carbon media
Soaking	• Simple process • High PCM loading. • Low cost	• Only applicable for porous 3D carbon skeleton
Hydrothermal	• High loading of PCM	• Energy consuming process • Agglomeration of carbon media
Melt blending+ steam explosion	• Less agglomeration of carbon media • Sufficient loading of PCM in carbon matrix	• High cost • Issue with scale up
Squeezing	• Easy process • Low cost	• Only applicable for flexible foam like 3D carbon skeleton
Microencapsulation	• Low cost • Low operating temperature • Versatile synthesis process	• Uncoated PCM • Difficult to remove surfactant like impurity completely. • Agglomeration between microencapsulated particles

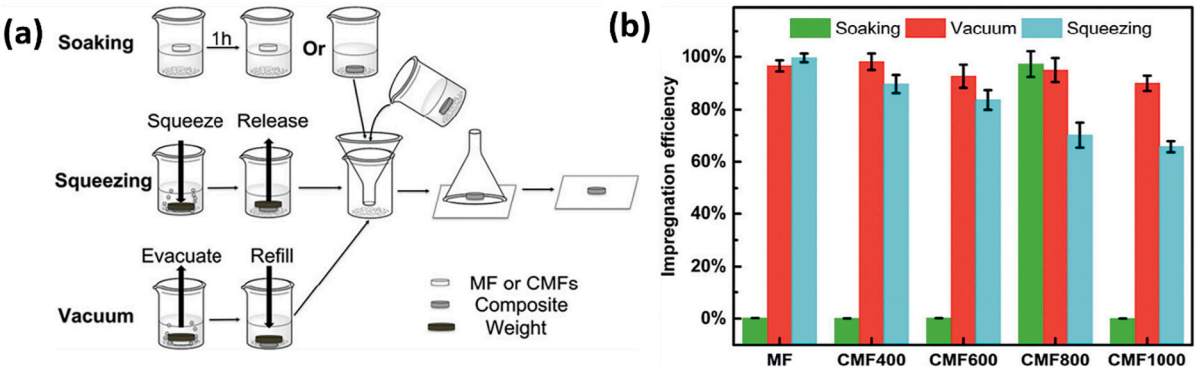

Fig. 10. (a) Typical synthesis process of CF/$CaCl_2$ composite (b) PCM impregnation efficiency performance of the composite prepared with different methods [101].

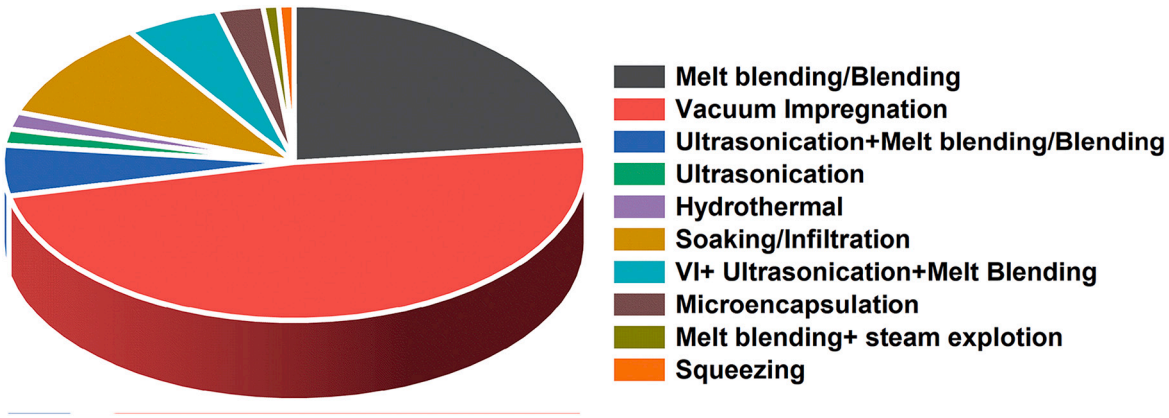

Fig. 11. A comparative pi-chart diagram demonstrating different methodologies' contribution to creating 3D Carbon/PCM composite, the graph is made based on literature reports.

ExFG/AC-based PCM composite, a high degree of homogeneous dispersion of PCM can be achieved via the blending/melt-blending process. However, the distribution of s-s PCM in 3D carbon is still challenging. Dai et al. fabricated solid-solid PCM/3D carbon composites via melt blending and ball milling. EG with PCM was milled together to enhance the dispersion stability, followed by heating at 200 °C to melt the PCM [102].

To guarantee a homogeneous connection between PCM and 3D carbon, especially for solid-liquid PCM, the operating temperature of melt blending and blending time played an essential role in avoiding the agglomerates. It often combines a few methods, such as ultrasonication and melt blending [103]. Notably, a large surface area of and size of 3D carbon, i.e., graphene aerogels or expanded GO, must be considered in the production process [62].

4. The effect of different 3D carbon media towards thermophysical attributes of PCM composites

4.1. EG and its modified PCM composite

Yang et al. fabricated a PEG/EG-based form stable composite for LHTES application [104]. Interestingly, the solid-liquid phase transition of PEG decreased after loading of EG, which signifies the decrease in crystallization integrity within PEG in the presence of EG. Compared to pristine PEG, the composite took a brief thermal storage and cooling period (time storage = 1810 s, time cooling = 2370 s). As the sugar-based PCM possesses a long nucleation process, Wang et al. mitigated such an issue by fabricating a galactitol/mannitol eutectic composite with EG [105]. The large specific surface area of EG and porous microstructure facilitate facile and rapid adsorption and nucleation of sugar alcohol. Besides the supercooling effect, EG's presence remarkably enhances the thermal conductivity of the composite. High latent heat of melting enthalpy reaching198.60 kJ.kg^{-1} and efficient thermal stability up to 20 cycles are the unique benefits of this report. The different EG loading (%) in the composite substantially affects the composite's thermophysical properties, as suggested by Fang et al. [98]. The authors incorporated EG from 0.5 to 4 % to investigate the heat storage capacity of paraffin/alkylated EG composite. The interfacial adhesion between alkylated EG and PCM is the primary reason for improved latent heat storage. The strong interfacial bonding arises from the same polarity and hydrophobicity between paraffin and alkylated EG. Therefore, more heat is required to cross the hindrance of the alkyl group present on EG during melting or freezing. Higher crystallinity restricts the molecular movement along the composite structure, facilitating heat transport. The poor adhesion of EG with the PCM and low degree of crystallinity was found for a high amount of EG-loaded composite, resulting in a sharp decrease in their thermophysical parameters. Similarly, Liu et al. fabricated a hyper-crosslinked polymer/EG-based 3D carbon skeleton for thermal energy storage [106]. In situ- formation of hyper-crosslinked polymers was taken in the presence of precursor and oxidant. Here, the segregation of crosslinked polymers was prevented in the presence of EG; thereby, efficient adsorption of PCM into its pore took place. About 20 mass fractions of crosslinked polymers are utilized to suppress the PCM leakage rate (0.52 %). The composite's high surface area (407.31 m^2g^{-1}) in the presence of cross-linked polymer is also co-related with the high filling of PCM (89.4 %) into the porous architecture. Inflated surface area is a potential attribute of the high-performance material for LHTES application, as it is directly conjugated with the heat adsorption efficacy of the material. Wu et al. also proposed the role of olefin block-copolymer towards improved leakage and flexibility during the fabrication of olefin block-copolymer/paraffin wax/EG-based flexible organic EG composite for thermal energy management [107].

Luo et al. incorporated N-doped porous carbon into SA/EG composite to boost the heat storage efficacy of the composite [69]. With decreasing SA mass fraction, the latent heat storage efficacy of the composite was also reduced. The lower crystallinity factor of the composite denotes a more vital interaction with a low phase preservation rate. The advanced melting process with delayed freezing was observed by adding 80-85 % SA. Also, the high thermal conductivity of the composite may prevent the crystallization process. The efficient heat transfer throughout the 3D network porous structure composite is also essential to eliminate the supercooling phenomenon. The combination of fast melting and delayed crystallization has unique benefits. Yuan et al. developed an erythritol/EG-based composite having 40 times higher thermal charging-discharging efficacy concerning pristine PCM [108]. The presence of EG significantly decreased the melting temperature of PCM from 116 to 98 °C while the freezing point increased significantly. The average charging time of PCM was reduced by 73 % after adding 12 wt% EG, and the supercooling degree of pure erythritol decreased from 39.5 to 15.3 °C after adding 15 wt% EG to the composite structure. Excellent thermal conductivity of the composite and high loading of PCM, induced by EG, helps the fast charging and discharging process, which is the main reason for the abovementioned observation. For high EG contents, no mass loss of PCM was observed from the 85th to 140th cycle, while negligible (0.4-0.5 %) mass loss was apparent from the 40th to 85th cycle. Therefore, the good cyclic stability of the composite, even after 140 cycles, is another good attribute of this report. The presence of EG facilitates easier nucleation of PCM molecules via adsorbing the PCM into its porous structure. In 2020, Wang et al. found that the increased density of bulk EG causes a significant effect on increasing the length of graphite sheets [75]. By increasing the applied pressure, the author fabricated compressed bulk EG with different densities. The increased density of EG bulk yields a higher degree of anisotropy due to the homogeneous and increased distribution of

paraffin in the EG microstructure. The high anisotropy and long graphite sheets facilitate the composite structure's extended heat transfer pathway with low thermal resistance. The author suggested that the microstructural integrity and the synergetic effect of bulk EG and paraffin provide high thermal conductivity (20.8 Wm^{-1} K^{-1} at 60 °C) in the parallel direction. Almost a two-order increase in the thermal conductivity of the composite was observed by Liang et al. for PW/EG@GO-based composites [46] see Fig. 12a,c. The facile and fast conduction of heat due to the presence of EG in the PW matrix and additional thermal conduction pathways offered by covered GO sheets are the main reasons for the dramatic improvement of thermal conductivity. Only ~6 % leakage rate was observed for the composite within 500 h, while the pace was fast for the first 300 h, Fig. 12b. The presence of two protective layers that arise from EG through capillary action and GO layers through the formation of the zig-zag pathway was responsible for such improved leakage attributes, see Fig. 12d-e.

Inorganic EG-based composites have emerged as superior candidates for the LHTES application. Huang et al. investigated the storage behavior of $LiNO_3$-KCl/EG composite [109]. The composite's excellent preservation of shape, melting, and freezing point in the DSC thermogram after 10, 50, 100, and 500 cycles signify excellent long-term stability under repetitive phase transition. The hydrophilic inorganic moiety can revamp the composite's heat storage efficacy, as Ren et al. claimed for Na_2HPO_4. $12H_2O$/EG/SiO_2 composite system [110]. The group observed that in the absence of SiO_2, Na_2HPO_4. $12H_2O$/EG did not demonstrate any heat storage efficacy due to the non-intercalating ability of PCM into EG pores. The silica originating in an alkaline or acidic environment modifies the pores of EG to permit PCM entry. In the presence of PCM, the porosity of the composite was abruptly reduced due to the triumphant entry of PCM, see Table 3. The thermal storage capacity of EG-DHPD-SiO_2 (prepared in acidic condition) is higher (224 Jg^{-1}) than that of EG-SiO_2 (prepared in the alkaline state)-DHPD due to increased pore volume occupied by SiO_2 prepared in alkaline condition, preventing PCM for encapsulation, see Table 3.

Table 3
The porosity, apparent density, and encapsulation ratio profile of Na_2HPO_4. $12H_2O$/EG/SiO_2 composite [110].

Sample	Porosity [%]	Apparent density [g m^{-1} L^{-1}]	Encapsulation ratio [%]
EG	96.25	0.84	/
EG-DHPD	81.02	3.38	95
EG-SiO_2(a)	96.47	2.94	/
EG-SiO_2(a)-DHPD	82.34	2.14 74	74
EG-SiO_2(b)	85.22	1.99	/
EG-SiO_2(b)-DHPD	71.98	2.04	49

Low supercooling temperature (5 °C) is another benefit of this composite. In 2020, Li et al. investigated the heat storage performance of EG/Na_2SO_4.$10H_2O$ composite [111]. The authors modified the PCM, Na_2SO_4·$10H_2O$, by employing borax decahydrate, CMC, and the octyl phenol polyoxyethylene ether (OP-10) as a coupling agent to improve the binding energy between Na_2SO_4·$10H_2O$ and EG. The DSC diagram shown in Fig. 13a demonstrates that pure and modified PCM possess high levels of supercooling. The freezing temperature of the composite was increased compared to unmodified PCM, while a slight increase in the melting temperature trend of the composite was observed. The pores of EG may form strong connections with PCM that facilitate the excellent flow of heat through the composite. The low supercooling value (5.99 °C) of modified PCM indicates the improved nucleation of PCM in the presence of borax decahydrate during the crystallization process. During melting and freezing, the latent heat of enthalpy for 7 % EG-loaded composite was 114 Jg^{-1} and 105 Jg^{-1}, respectively. However, increasing EG content decreases the composite's latent heat per PCM unit mass. The temperature vs. time curve shows the fast-thermal

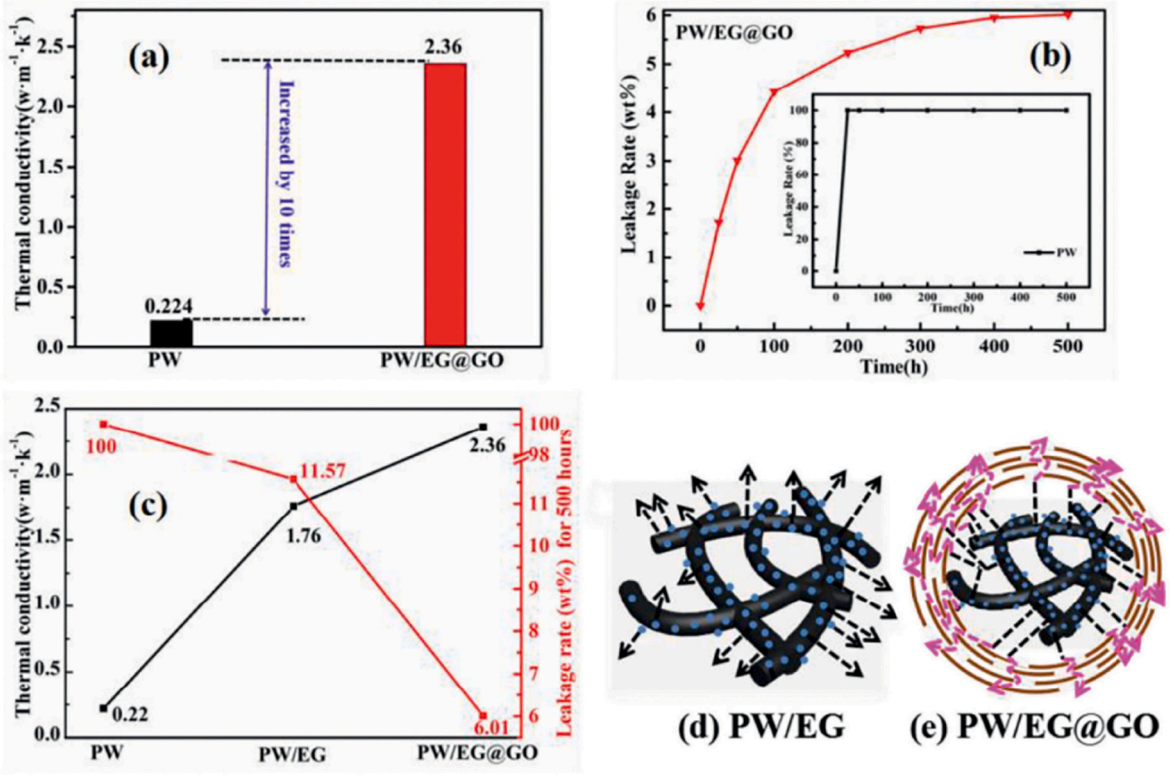

Fig. 12. (a) Thermal conductivity of paraffin wax (PW) and EG/GO-based PW composite, (b) The leakage rate vs. time profile of PW and EG/GO-based PW composite, (c) The comparison of the thermal conductivity and leakage rate of EG/GO-based PW composite with its counterpart part (d), (e) Plausible mechanism of the leakage paths for EG/GO-based PW and PW/EG composite [46].

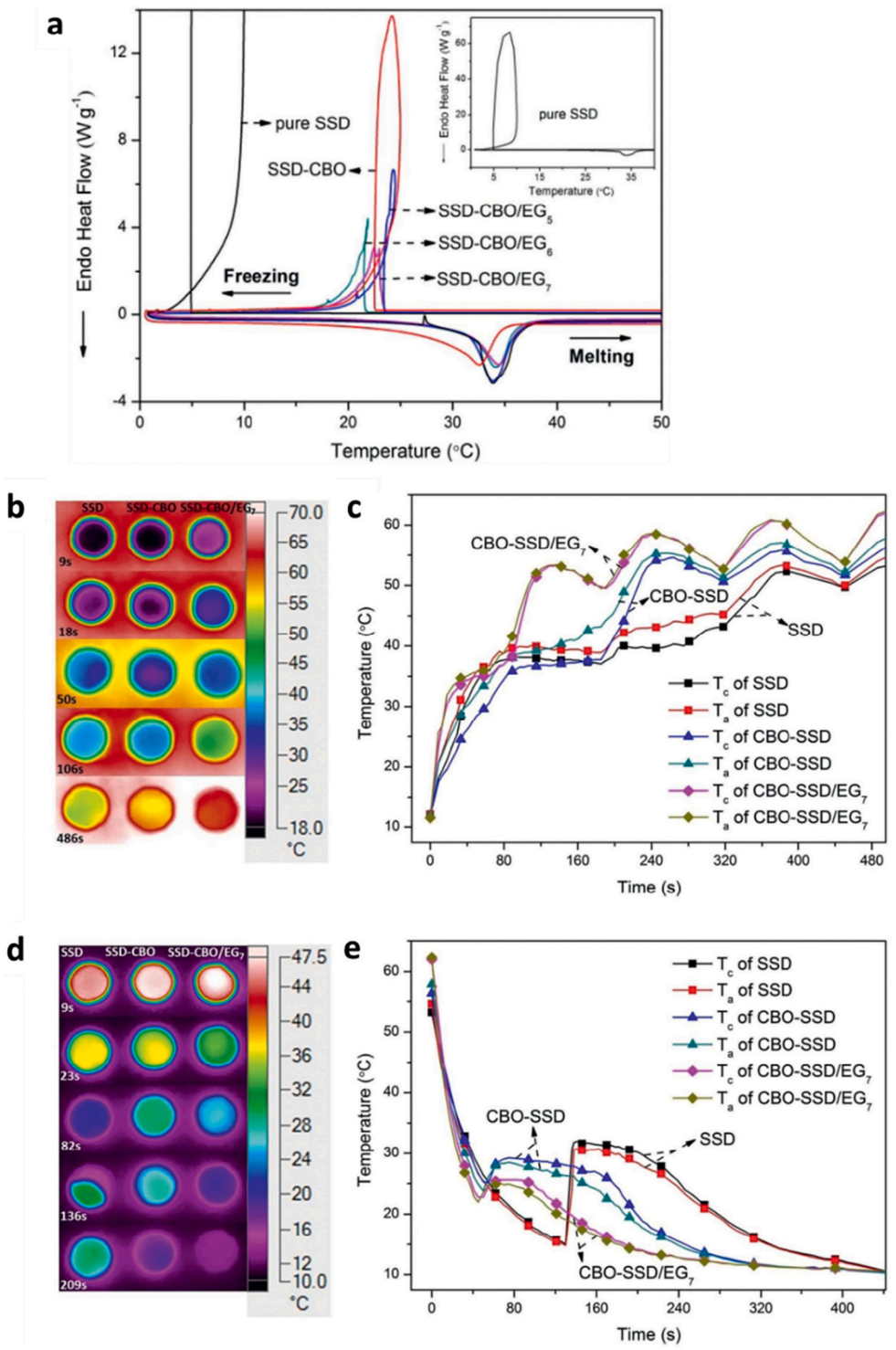

Fig. 13. (a) The DSC diagram of SSD-CBO (sodium sulfate decahydrate ($Na_2SO_4{\cdot}10H_2O$, SSD), borax decahydrate, $Na_2B_4O_7{\cdot}10H_2O$), octyl phenol polyoxymethylene ether ($C_{34}H_{62}O_{11}$, OP-10), carboxymethyl cellulose-based composite) (EG composite with varying EG loading (b-e) The visual appearance of the composite and pristine counterpart along with the change in temperature vs. time curve during the heating-cooling process [111].

response of 7 % EG-loaded composite. The temperature interval of the inflection point is lower for EG-based composite than pure PCM, which is in solid agreement with the experimental findings in the DSC thermogram.

Furthermore, the temperature difference between the sample's center and the sample's average value during melting or cooling for 7 % EG loaded composite is relatively low, which signifies excellent heat diffusion throughout the composite. The temperature response of the composite with time during the heating-cooling process is shown in Fig. 13b-e. In summary, the efficient suppression of supercooling of the PCM in the composite, near room temperature, melting and freezing point (T_{melt} = 31.06 °C, T_{cool} = 23.02 °C) along with fast thermal response is the uniqueness of this material that may be utilized in-floor heating system application. Recently, Bai et al. fabricated a PEG-VO_2-based dual PCM/EG composite via vacuum impregnation [112]. There were two phase transition peaks during the heating-cooling process in

the range of 30°-70° and 50°-70 °C. The presence of dual peaks from both PEG and VO_2 confirms the formation of a dual-PCM-based composite. The optimized concentration of EG loading in the dual-phase PCM composite was reported as 0.10 % to obtain high crystallinity and inflated latent enthalpy (112.79 Jg^{-1}). The composite possesses excellent thermal recycling stability even after 50 cycles. The only mild temperature difference and 0.59 % and 0.86 % changes in latent heat enthalpy value were observed during the first and 2nd phase heating-cooling cycles. The fast heat transfer (16 s for the heating response, 101 s for the cooling response) and high thermal response were apparent for the EG-based dual phase change composites compared to the new PCM due to the increased loading of PCM into the EG skeleton and high thermal conductivity. Yu et al. adopted an intelligent approach for preparing EG-based shape-stable microcapsules for TES application [96]. Here, the essential part of this report lies in the design of the material. As a shell, the author used nano-copper/silicon/EG-based elastomer or EBInSn alloy silicon/EG-based elastomer, which act as a protective layer of core material (octadecane of octadecane/EG) and take part in solid to liquid alteration phenomenon at the same time because of inherent phase change attributes of the inorganic copper or phase change alloy. The most significant advantage of such microcapsules lies in their shape and re-molded attributes.

Various conditions like a dumbbell, prolate ellipsoid, concave, and petal could be obtained for PCM microcapsule with no deformation of core PCM, see Fig. 14a-d. Thanks to a flexible shell in the microcapsule that helps restore its original shape even after heating at 120 °C with the successful volumetric expansion of octadecanol, see Fig. 14e. The fabricated shape stable elastic microcapsule (1 % EG loaded inorganic EBInSn/silicon-based elastomer) demonstrated a substantial latent heat density of 192.4 MJm^{-3} with high preservation of deformation up to 432 %. To understand the role of the thermal conductivity of the core and shell towards heat storage and release efficacy, the author fabricated four different samples, as depicted in Table 4. It shows the presence of EG significantly increases the thermal conductivity of the shell and core material. However, the heat charging and discharging time was improved in the presence of the core with high thermal conductivity due to the fast transfer of heat.

Table 4
The summary of the effect of thermal conductivity of PCM microcapsule by tuning the composition of core and shell [96].

No.	Material composition of core and shell	Thermal conductivity (Wm^{-1} K^{-1})		Latent heat density (MJm^{-3})
		Core	Shell	
1	Oct: Silicone	0.29	0.20	168.6
2	Oct: Silicone +80 wt% EBiInSn +1 wt% EG	0.29	1.98	213.4
3	Oct + 2 wt%EG: Silicone +80 wt% EBiInSn +1 wt%EG	1.16	1.98	211.6
4	Oct + 3 wt%EG: Silicone +80 wt% EBiInSn +1 wt%EG	1.53	1.98	210.1

Ao et al. reported that introducing BN and EG as carbon media can significantly revamp stearic acid's thermal conductivity and thermal energy storage efficacy. Adding combined BN and EG filler showed a significant decrease in the supercooling effect, indicating nucleation-induced crystallization of PCM molecules [113].

4.2. ExFG and its modified PCM composite

Jeong et al. investigated the thermal energy storage efficacy of two members of the paraffin group, i.e., octadecane and tetradecane/Na-MMT/ExFG -based composite [114]. The presence of ExFG significantly enhanced the PCM incorporation rate and latent heat of enthalpy for both PCM-based composites. The incorporation rate of PCM was also improved from 23.29 to 26.60 % and 21.24 to 31.82 % in the absence and presence of ExFG in n-Hexadecane/Na-MMT and n-Octadecane/Na-MMT based composite, respectively. The composite's high thermal conductivity and porous architecture in the presence of ExFG may be responsible for enhanced PCM incorporation and high thermal efficiency. The clay was mainly employed to induce fire retardant attributes and high PCM adsorption capacity into the composite structure. Zeng et al. fabricated erythritol-mannitol/ExFG composites varying the mole fraction of erythritol from 0.1 to 0.9, respectively [115]. The eutectic

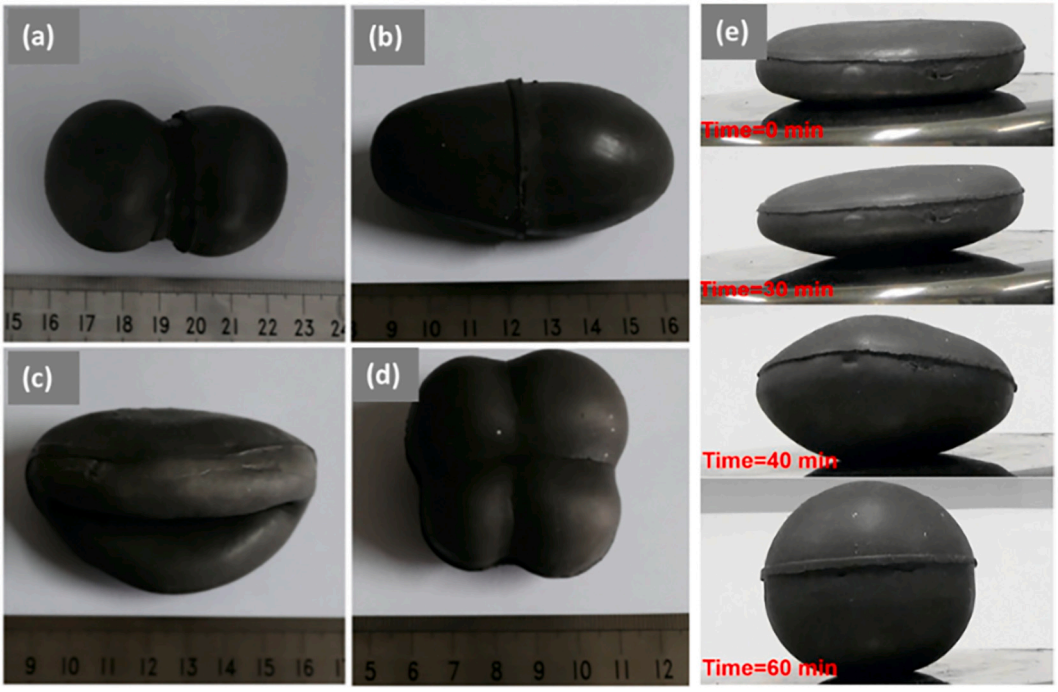

Fig. 14. (a-e) The different shapes of the remolded microcapsule like (b) dumbbell, (c) prolate ellipsoid, (d) concave and (e) petal (f) the restoration of the original shape of the microcapsule even after heating [96].

PCM with a mole fraction of mannitol and erythritol of 0.87 demonstrated high latent enthalpy with stable melting characteristics up to the 50th cycle. However, it lost crystallization during cooling cycles. The severe supercooling was mitigated after adding EG, as observed. With the increase in the loading percentage of ExFG from 1 to 3 %, the degree of supercooling decreased from 67.65 to 62.57, while the reverse trend was apparent at high graphite loading. The scenario worsens after 3 wt% graphite loading due to PCM's non-uniform mixing and lack of phase change transition. Liu et al. fabricated paraffin/ExFG composite with varying EG concentrations from 0.2 to 2.0 wt% in composite structure [116]. The melting enthalpy of the composite was increased from 140.66 to 170.3 Jg^{-1} with increasing graphite content from 0.2 to 1 %, but a further increase in loading concertation yielded a significant drop in melting enthalpy.

4.3. Carbon foam and its modified composite

Li et al. observed that the change in weight percentage of carbon precursor may significantly affect the thermal properties of PCM composite [117]. The high thermal conductivity after Al_2O_3@GF incorporation in PCM signifies the efficient contact between the composite structure's thermally conductive media, promoting an extended heat transport pathway with elevated thermal flux inside the composite structure [15]. From Raman spectra and TEM analysis, the authors concluded that the high degree of graphitization (high I_D/I_G), good crystallinity of the composite sintered at 1600 °C plays a pivotal role in enhanced thermal conductivity, significantly facilitating heat diffusion performance throughout the composite. Interestingly, the supercooling of paraffin decreased from 12.1 to 6.92 °C for the composite prepared with 30 % sucrose precursor. The inflated surface area and enormous heterogeneous pores in the composite structure facilitate the nucleation process of paraffin during crystallization. The latent heat of enthalpy of the composite was significantly reduced for the composite prepared with 40 % sucrose precursor. The high paraffin storage efficacy and optimized hierarchical porous architecture with an enhanced surface area were crucial to obtaining the best-performance composite. Lin et al. reported excellent efficacy of PEG/MWCNT-modified CF-based composite towards a light-to-thermal energy conversion and storage [118]. To investigate the effect of thermal attributes of PEG in the presence of CF and MWCNT, the authors proposed the terms "enthalpy efficiency" and "relative enthalpy efficiency." The mathematical expressions are given below:

$$\lambda\ (\text{enthalpy efficiency}) = \frac{\Delta H_{m(PEG/CFs)} + \Delta H_{f(PEG/CFs)}}{\Delta H_{m(PEG)} + \Delta H_{f(PEG)}} \times 100\% \quad (2)$$

$$\eta(\text{relative enthalpy efficiency}) = \frac{\Delta H_{m(PEG/CFs)} + \Delta H_{f(PEG/CFs)}}{\Delta H_{m(PEG)} + \Delta H_{f(PEG)\times w}} \times 100\% \quad (3)$$

The $\Delta H_{m(PEG/CFs)}$ and $\Delta H_{m(PEG)}$ is the melting enthalpy of PEG/CFs, and pure PEG, $\Delta H_{f(PEG/CFs)}$, and $\Delta H_{f(PEG)}$ is the freezing enthalpy of PEG/CFs and pure PEG, w is the weight percentage of PEG in the composite structure. The high λ (98.7 %) indicates the whole latent heat of PEG during phase transition is stored or dissipated via phase transition with no additional changes in the thermal attributes of pristine PEG after confinement into the pores of CF. The optimized MWCNT concentration to obtain maximum changes of latent enthalpy (170.9 Jg^{-1} for melting and 159.2 Jg^{-1} for cooling) was found to be 2 % during melting or cooling. The high cyclic stability, even after 1000 cycles of phase transition, is the additional benefit of this article. In 2018, Su et al. adopted a unique approach to preparing modified CF-based 3D composites [100]. 3D CF was generated using GO and MWCNT or SWCNT as precursors. According to the authors, MWCNT may enhance thermal conductivity, and GO can act as porous support to prevent leakage in the composite structure. The melting-freezing temperature latent enthalpy of the composite increased with increasing MWCNT or SWCNT contents in the composite structure. The authors suggested that MWCNT or SWCNT acts as a nucleating agent of PEG, and successful nucleation significantly reduced the crystallization rate of PEG by a change in its conformation. The continuous spherulite crystallization pattern changed to discrete small spherulite crystal morphology in the presence of high CNT contents in the composite structure. Yu et al. reported increased thermal energy storage efficacy of newly developed shape-stable 3D CNT/GF/PEG-based composites [119]. The optimized CNT concentration obtained better crystallization efficiency, encapsulation fraction, and heat storage capability of 80 %. The above-said composites demonstrated 91.6 % crystallization efficiency, 73.29 % encapsulation ratio, and 91.46 % heat storage capability. The supercooling effect is also low for the newly developed composite. High thermal conductivity, network-like microstructure with nano and micropores, and enhanced intermolecular association between GF, CNT, and PEG are responsible for the improved thermophysical attributes of the composite. The authors also investigated the effect of thermal resistance on heat storage efficacy and examined the temperature distribution of CNT/GF/PEG and PEG/GF composite. The interfacial thermal resistance of the CNT/GF/PEG composite was 67 % lower compared to the PEG/GF composite. The formation of a 3D network-like architecture between GF and CNT significantly facilitates enhanced heat transport during the phase change of PEG. At the same time, the presence of only CNT in the PEG matrix yielded a high accumulation of CNTs that formed different interfaces during phase change. Wu et al. also utilized GF and water-borne PU to encapsulate octadecanol to mitigate leakage issues successfully [120]. The presence of GF significantly reduces the supercooling effect of PCM, which may be correlated with the high thermal conductivity and rugged surface of GF. Fast temperature shifting between the environment and the composite and enhanced nucleation of PCM in the composite structure during the crystallization process play a pivotal role in removing the supercooling effect. Kholmanov et al. also reported the UGF/erythritol/CNT as an active composite for TES application [55]. A significant increase in thermal diffusivity and conductivity was apparent for the composite compared to its new counterpart. To assess the role of the continuous networking pathway formed in the presence of GF and CNT, the authors have grounded the composite in powder form to break the continuous pathway of carbon and measured the conductivity. The decrease in thermal conductivity and diffusivity signifies the role of a continuous carbon network towards enhanced thermal attributes. The authors also performed another experiment to investigate the role of bonded CNT. The non-bonded CNT composite possesses lower thermal conductivity than the bonded CNT/erythritol/UGF composite. This observation signifies the lower thermal resistance of the composite when CNT s is in bonded condition with UGF; see Fig. 15 a, b. From the DSC diagram, see Fig. 15 c-d; it was apparent that there was almost no change in the melting profile of the composite and pristine PCM. In contrast, a significant shift in freezing temperature was evident during the solidification process. The UGF/erythritol composite demonstrated $T_{sc} = 78 \pm 4$ K, while the CNT bonded composite simultaneously showed $T_{sc} = 67 \pm 4$ K. A further decrease in subcooling degree was observed for the powdered CNT/UGF/erythritol composite. The result signifies the role of increased surface area and heterogeneous surface sites of the composite for the successful crystallization of erythritol in the composite structure. Zhang et al. fabricated GF/erythritol composite for moderate temperature management application [121]. Interestingly, the supercooling degree was surprisingly low for high- and low-bulk-density GF/erythritol composites compared to pure erythritol. The L-GF composite's supercooling degree was higher than the H-GF composite. The infiltration rate of erythritol is crucial in obtaining the composite's different performances, as it has different bulk density graphite. As observed from the SEM micrograph, the smaller cell diameter of H-GF prevents high filling of PCM compared to L-GF. The 3D-ordered packed structure of the composite and its high thermal conductivity play another crucial role in reducing the supercooling degree. Zhang et al. proposed a plausible mechanism of heat transfer through the composite. The highly ordered

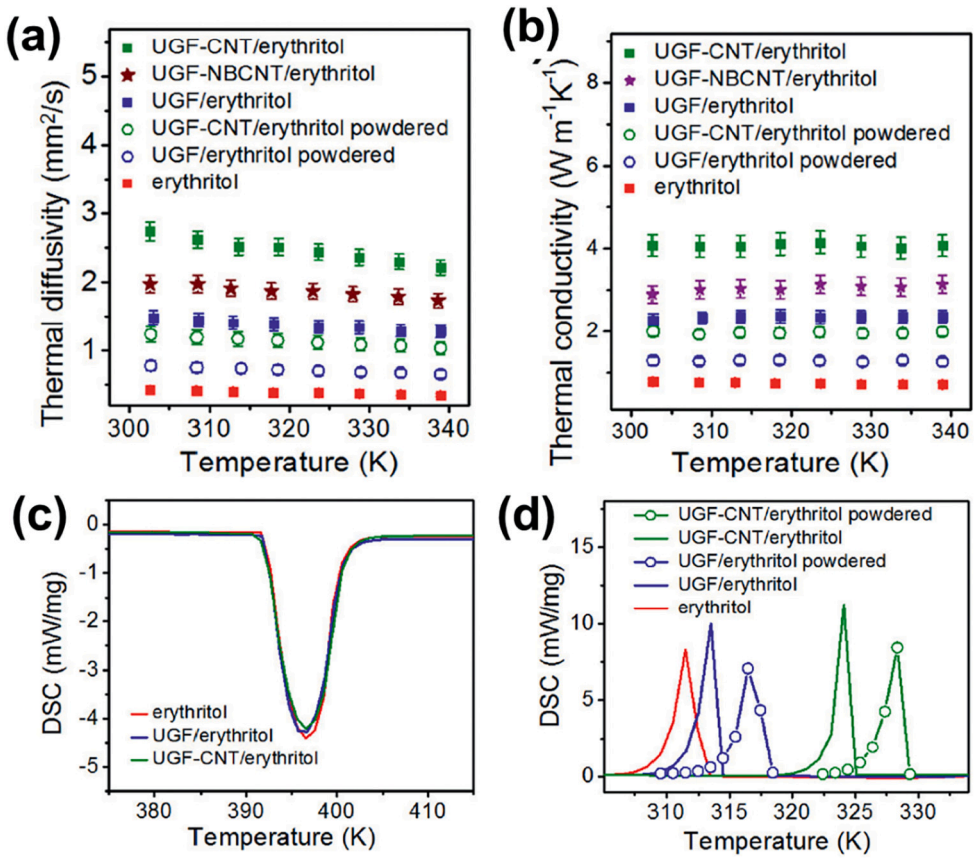

Fig. 15. (a, b) Thermal diffusivity and thermal conductivity of erythritol, UGF/erythritol, and UGFCNT/erythritol (c) DSC melting curves for erythritol, UGF/erythritol, and UGFCNT/erythritol. (d) DSC cooling curves for erythritol, UGF/erythritol, UGFCNT/erythritol, and powdered UGF/erythritol and UGFCNT/erythritol [55].

structure of the composite facilitates the rapid transfer of phonons. Furthermore, the strong adhesion of GF and erythritol reduces the interfacial thermal resistance. According to the authors, the critical radius is inversely proportional to the supercooling degree. Singh et al. investigated the effect of inorganic salt ($MgCl_2$) impregnation on high- and low-density GF for LHTES application [122]. The latent heat of fusion for LD foam/$MgCl_2$ composite (225.2–238.5 $KJKg^{-1}$) was higher compared to LD foam composite (353.6– 379.6 $KJKg^{-1}$). Wang et al. deployed Ti_2O_3/CF polydopamine-based miscellaneous carbon media for LHTES application [77]. The excellent compression-bending resilience attributes were apparent for the composite due to the high modulus of CF elasticity arising from the removal of long side chains from MF. However, the annealing temperature of CF severely affected the composite's mechanical strength. The high temperature may yield a fracture of the composite structure. The optimized annealing temperature was found to be 400 °C. In this report, polydopamine (PDA) was chosen for its strong adhesion with different organic or ceramic materials. At the same time, n-eicosane was recommended due to its high latent capacity and long-term stability. The excellent flexibility of the composite was observed from the optical image during the bending and compression stage.

4.4. CA and its modified PCM composite

Zou et al. synthesized a stable palmitic acid-based CA composite for thermal energy storage application [60]. The authors prepared CA from two biomass sources, i.e., carrot and pumpkin. The carrot-derived CA-based PCM composite shows enhanced latent melting heat compared to the pumpkin-derived composite. The calcined temperature of CA and curing temperature of PCM cause a significant effect on the melting point or latent heat energy of pure PCM. Although the surface area of pumpkin-derived CA was lower than carrot-derived CA, the rapid increase in temperature within 25 s on the composite surface was observed for cured PCM-loaded pumpkin-derived aerogel at high calcined temperature. This result signifies that the surface area has almost no effect on heat storage. The authors suggested that the high thermal conductivity of the composite solely increased the fast heat movement. However, the disorganized orientation of graphene sheets in aerogel structure may revamp boundary thermal resistance, significantly decreasing the composite's thermal conductivity. Anisotropic graphene aerogel is one of the potential approaches to mitigate this issue owing to the structural organization of graphene sheets and thick pore walls. In 2021, Li et al. reported excellent enhancement of longitudinal thermal conductivity (50–300 %) of paraffin in anisotropic reduced graphene oxide (rGO)/expanded graphite (EG) aerogel-based composite structure [123]. Zhang et al. reported that the combined effect of Ag nanoparticles and anisotropic graphene aerogel is quite promising to achieve remarkable enhancement of (~362 %) thermal conductivity of PCM composite.

A faster phase transition with a 74 % enhancement in heat storage-release efficiency is the unique benefit of this report [124]. Zhang et al. investigated the role of kapok fiber-based aerogel in the thermal energy storage efficacy of PEG [61]. It was observed that the presence of hydroxylated BN in the kapok fiber-based aerogel significantly affects the thermal conductivity of the composite. The hydroxylation of BN induces strong adhesion between boron nitride and kapok fiber, facilitating the reduction of the thermal resistance at the interface, which is beneficial for increasing faster heat transport through the composite structure. Adding pristine BN from 0 to 10 wt% decreased ~17 % latent heat of enthalpy of pristine PEG. However, a ~ 13 % decrease in latent

heat of enthalpy was apparent for hydroxylated boron nitride (0-10 %) based composites. The author suggested that the strong adhesion between PEG and hydroxylated kapok fiber aerogel through hydrogen bonding induces a more homogeneous distribution of PEG into the composite structure. Kong et al. investigated the effect of large-sized graphene aerogel on the thermal energy storage efficacy of graphene aerogel/paraffin composite [62]. The thermal conductivity of the large-sized graphene aerogel prepared at high calcination temperature (2800 °C) caused higher thermal conductivity compared to its pristine counterpart owing to the presence of a three-dimensional, defect-less, high surface area graphene network that promotes facile phonon transfer through the composite. From the I_D/I_G curve, the authors calculated the in-plane crystal grain size (L_a) for large- and small-sized graphene aerogels. The result reveals that an almost 135.5 % increase in L_a value for large-sized graphene aerogel signifies less grain boundary, which may facilitate improving the composite's thermal conductivity. The high I_D/I_G ratio for graphene aerogel calcined at 2800 °C compared to graphene aerogel calcined at 1000 °C signifies the high calcined temperature induces a high degree of graphitization. To analyze the 3D stacking profile of the composite, the authors fitted the 2D Raman peak of the composite. The G_{3DB}' (ordered AB Bernal stacking of graphene layers) was higher for large-sized graphene aerogel composite, indicating efficient arrangement in the graphitic structure of the composite. The fraction of AB Bernal stacking for large-sized graphene aerogel composite was found to be 63.32 %, while it appears as 56.1 % for large-sized graphene aerogel composite. The ordered 3D arrangement with a high degree of stacking of graphite sheets may help facilitate an efficient heat transfer process. Fast (30 s) and higher rise in temperature were observed for large-sized graphene aerogel composite compared to the pristine part. The high ratio of $\Delta H_{composite}/\Delta H_{PA}$ (98.1 %) and excellent retention rate of specific latent heat enthalpy (99.21 % for 15 cycles and 97.11 % for 30 cycles) are the most promising outlook of this report for the utilization of this functional material in thermal management applications in future. Song et al. prepared lauric acid/carbonized kapok fiber aerogel/Fe_3O_4-based composites [59]. The aerogel's superior mechanical stability (5.6 % deformation) in the presence of iron oxide particles under 60 % compressive strain at the 40th cycle signifies the perfect utilization of such newly designed CA for developing shape-stable and flexible engineered material for TES application.

In 2018, Li et al. introduced paraffin or PEG into the pores of graphene aerogel fiber via vacuum impregnation method at 80 °C for 3 h, followed by coating with fluorocarbon resin [66]. A decrease in fracture strain from 2.5 to 1.52 % was apparent for the composite fiber. The formation of a core-shell-like laminated structure and the presence of fluorocarbon resin significantly enhance the mechanical attributes of the composite. The novel composite's young modulus and fracture strength were 48 times and 775 % higher than graphene fiber aerogel. However, at the melting stage of PEG, fracture strength and young modulus (E) of the PCM/graphene aerogel fiber were lower than the solid state of PEG in the composite at 25 °C. It was caused by the softening effect of PEG during melting. However, the composite still preserves high toughness even after melting PEG compared to prepared fiber. The graphene aerogel fiber/PEG contact angle was <60°, at 9.4° and 124° for pristine PEG and graphene aerogel fiber. Du et al. found that the surface modification of porous CA precursor (nano-fibrillated cellulose) significantly impacts the adhesion property of PCM and the cellulose surface for TES management [63]. The highest loading of PCM for a higher degree of carbon-aliphatic chains grafted composite was observed than the new and other synthesized composite. The mismatching of hydrophobic n-octacosane with the surface of hydrophilic cellulose is responsible for such observation. The high hydrophobicity on the high aliphatic chain grafted cellulose facilitates efficient adhesion towards hydrophobic PCM, thereby increasing the PCM loading rate onto the cellulose surface.

4.5. Porous carbon and its modified PCM composite

Luo et al. observed that the presence of aligned N-doped porous carbon also enhances the thermal conductivity of the composites compared to pristine PEG and PEG/porous carbon composite [58]. The increment of 3D carbon volume fraction in the PCM composite structure significantly improved the composite's thermal conductivity. According to the authors, this enhancement in thermal conductivity is directly related to the following equation,

$$k_{PEG}/_{C} = \langle cos^2\Theta \rangle f k_C + (1 - f) k_{PEG} \quad (4)$$

$k_{PEG/C}$ is the thermal conductivity of the composite, and f and k_C are the carbon support's volume fraction and thermal conductivity, respectively. k_{PEG} is the thermal conductivity of PCM, θ is the angle between 3D carbon and the direction of thermal transport. For porous carbon composite, $\cos^2\Theta$ value was assumed to be 1/3 because of heat transfer through x, y, z direction, while for aligned carbon/PEG composite, the accepted value was 1, considering unidirectional heat transfer. In this situation, the volume fraction of 3D carbon becomes a predominant factor in controlling the thermal conductivity of the composite. The above model perfectly fits experimental results, signifying unidirectional heat transfer is the ultimate benefit of decreasing heat scattering. The improvement of thermal conductivity, reproducible thermal cyclic performance, and non-leaking form stable attributes of sugar alcohol or fatty acid-based PCM in the presence of EG was also reported by several researchers [125,94,126]. AC is one of the essential 3D porous adsorbents that can be conceived easily, and the source of the precursor is naturally abundant. Zhou et al. reported that the amount of PCM (PEG) could significantly change the melting and freezing point of the AC/PEG-based composite. The presence of AC efficiently encapsulates PEG without leakage [70]. However, the authors left the reason for the plausible decrease in the melting temperature of the composite with an increase in PEG content unexplained.

Han et al. fabricated mysteric acid/AC/diatomite-based composite for building applications [84]. The increase in thermal conductivity of the composite after the incorporation of AC signifies the role of AC in the composite. The presence of AC in the composite significantly increases by about 1.8- and 3.6 times thermal storage and release rate compared to non-incorporated AC composite. The closely connected thermal network structure in the composite and the porous architecture of AC facilitate the fast heat transport phenomenon. However, high AC loading is responsible for the tiny decrease in the latent thermal energy compared to low AC loaded composite due to restricted movements of mysteric acid in the presence of a more significant number of *meso* or micropores of AC. However, a rapid temperature change was found for high AC-loaded composite (330 s, 270 s) during heating-cooling cycles compared to pristine PCM and low AC-loaded composite. A high amount of AC loading can effectively transport the heat through the composite structure, which is beneficial for such observation.

4.6. Supplementary 3D carbon and its composite

Liu et al. fabricated a novel composite based on Tetradecanol/melamine foam grafted with MWCNT (via polyacrylic acid chloride) composite for TES application [73]. Interestingly, with increasing the polymerization initiator (ALBN) content, the extent of supercooling was drastically reduced while melting and crystallization enthalpy were increased. The increased concentration of AlBN effectively decreases the polymer chain linkers, enhancing the strong connection between MF and MWCNTs. This phenomenon reduces the contact resistance at the junction and facilitates the fast transport of heat, resulting in high thermal conductivity. With increasing MWCNT- MF contents, the temperature rose quickly. For example, 2 % MWCNT- MF loaded PEG composite takes 1590 s to raise the temperature to ~59 °C while 950 s was spent by 8 % MWCNT- MF loaded PEG composite to reach this

temperature. Fast cooling up to 690 s was observed for high MWCNT-MF loaded composite compared to low MWCNT-MF loaded composite reaching 1290 s. The strong connection between melamine foam and MWCNT through covalent bonding facilitates fast heat transport with low thermal resistance. Li et al. fabricated 3D-porous RGO/MOF-5-supported SA-based composites for thermal energy storage [72]. The extent of supercooling decreased from 27.5 to 9.8 % of pristine SA, with increasing SA contents in the composite from 40 wt% to 90 wt% of SA in the composite. Interestingly, the carbonized carbon can accommodate 56.9 ± 1.9 % SA, whereas the presence of rGO enhances the SA loading up to 90 %. The presence of micro and mesopores in the composite structures facilitates the accommodation of SA molecules. The presence of rGO and MOF inhibits the facile movements of PCM, which is why the composite's melting or freezing point decreased. This newly fabricated carbon support was auspicious in encapsulating a variety of PCM with a significant enhancement in latent enthalpy; see Table 5. The newly manufactured composite's thermal conductivity was higher than its pristine counterpart. For pure MOF-5/SA composite, the air bubble present in the pores of MOF prevents the facile heat transport while the scattering of phonon arising from oxygen-containing groups bonded to the graphene sheet in GO/SA/MOF-5 composite also inhibits facile charge transport. However, the significant reduction in thermal contact resistance between rGO and SA enhances the thermal conductivity of the composite. For 90 % SA-loaded GO/MOF-5 composite, the decrease in thermal conductivity was observed due to the adsorption of SA on MOF-5, which is far away from rGO, which is the leading media for heat transport. From the heat storage and release study, Pure SA and the composite took 320 s and 280 s to reach the melting temperature (70 °C) from 35 °C. The composite took 50 s to absorb heat after reaching the melting point, while for pure SA, delayed heat absorption (150 s) was reported.

Song et al. created PEG/nanofibril cellulose/graphene nanosheet-based novel shape-memory phase change composites [127]. The LED device integrated hybrid film system demonstrates efficient heat dissipation behavior for both folded and unfolded film. However, the unfolded film changed its bud to a flower-like shape after reaching 70 °C temperature, extending the active contact area of the film with air. As a result, better thermal management efficacy of the unfolded film was observed compared to the folded one. This research group achieved an almost 9-fold increase in the in-plane thermal conductivity of the composite after self-assembly of 5 composite layers. The different 3D/PCM composite performance in thermal energy storage parameters, thermal conductivity, and possible application domains is presented as a tabulated summary in Tables 6a–6h.

An effort has been made to create different thermophysical attributes (the melting enthalpy, thermal conductivity, and melting temperature) based on the 3D carbon/PCM composite profile. A careful observation of Fig. 16a reveals that most of the reported organic and hybrid EG/PCM-based EG composite possesses high latent melting enthalpy and high thermal conductivity with low melting temperature, signifying the perfect utilization of such composite in low-temperature LHTES application. However, inorganic PCM composite can be utilized for moderate and high-temperature management applications. Therefore, more effort should be put into developing hybrid and inorganic EG-based composites with enhanced thermal conductivity for medium- and high-temperature applications. Fig. 16b reveals that most PCM-based ExFG composites possess high latent melting enthalpy of 60 to 190 Jg^{-1} with a melting temperature range of 15 °C to 55 °C and thermal conductivity within 0.5 Wm^{-1} K^{-1}. Therefore, the researchers must develop ExFG-based composites for various thermal management applications in non-explored areas. Thermal conductivity enhancement is another crucial point for EXFG-based composites. Tuning the synthesis process and changing precursor types of ExFG-based composite can yield high-performance energy storage material, which the researchers have not explored. There is a vast scope to examine such areas to develop low-cost, high-caliber materials. Fig. 16c represents that most of the reported PCM-based CF composite possesses latent melting enthalpy in the range of 80-200 Jg^{-1} in the melting temperature ranges from 30 °C to 80 °C, signifying perfect utilization of such composite in low-temperature. The average thermal conductivity of CF-based composite lies in the 0.1 to 1.5 W m^{-1} K^{-1} range. Therefore, developing CF-based composites with high latent enthalpy for moderate and high-temperature applications with enhanced thermal conductivity remains a considerable thrust area for researchers.

Carefully observing Fig. 16d reveals that most PCM-based GF composites possess high latent melting enthalpy within 370 Jg^{-1} with melting temperatures in the low and high-temperature ranges, including thermal conductivity within 80 Wm^{-1} K^{-1}. Fig. 16e reveals that most of the reported CA-based composites possess melting points in the 32-70 °C range with melting enthalpy ranging from 150 to 250 Jg^{-1}, respectively. The thermal conductivity of the most reported composite lies between 0.05 and 0.8 Wm^{-1} K^{-1}. Therefore, developing CA-based composites with enhanced thermal conductivity for low- and high-temperature applications is needed. Fig. 16f reveals that other 3D carbon-based composites have melting points of 22-80 °C with melting enthalpy ranging from 100 to 200 Jg^{-1}, respectively. Thermal conductivity enhancement is another crucial point for other 3D carbon/PCM-based composites.

Table 5
The Change in Latent enthalpy, Melting and Freezing temperature for octadecane/rGO @MOF, PEG/rGO @MOF, Octadecanol/rGO @MOF Composite [72].

Samples	SA loading	T_m/T_f (°C)	$\Delta H_m/H_f$ (J g^{-1})	$\Delta H_m/H_f$ in theory (J g^{-1})
pure SA	100	72.5/62.3	196.1/187.5	
SA/rGO@MOF-5-C	90	71.6/62.4	168.7/162.2	176.5/168.8
SA/rGO/MOF-5-C	90	73.2/64.1	142.4/138.1	176.5/168.8
SA/MOF-5-C	85	70.3/61.5	87.5/81.5	166.7/159.4
SA/GO@MOF-5	65			137.3/131.3
SA/MOF-5	50			127.5/121.9

5. Designed prototypes and numerical models for predicting the properties of 3D carbon/PCM composites

5.1. Prototypes

Dinker et al. investigated the heat storage efficacy of beeswax/EG composite in a rectangular and helical-shaped thermal storage unit [133]. Beeswax is among the most essential long-chain organic fatty acid PCM members in diversified application fields, like drug delivery and candle manufacture [175]. The prototype comprises a rectangular shell with 610 × 360 × 450 mm teak wood (20 mm thick, k = 0.12–0.04 Wm^{-1} K^{-1}) with a helical coil with thirteen turns of copper went through the middle of the shell, stainless-steel hot water tank with an electric heater (2 kW), a glass rotameter, and a centrifugal pump with brass valves. The authors investigated the effects of three different inlet temperatures of HTF (60 °C, 70 °C, and 80 °C) and three melted fluid flow rates (0.25 LPM, 0.5 LPM, and 1 LPM) towards heat storage application. The charging time of PCM decreased with an increase in flow rate. The authors suggested that increased internal heat transfer at the high flow rate from fluid to the tube was responsible for such a result. However, the thermal heat storage efficiency deteriorated at the high flow rate due to the immense power consumption by the pump for water. The composite demonstrated improved heat storage efficiency with fast charging compared to pure beeswax. The interconnected conductive network of EG may facilitate enhanced and facile heat transfer throughout the composite. Zheng et al. proposed another similar prototype model with a spiral coil tube as a heat exchanger and EG/paraffin

Table 6a
Summary of synthesis strategies, thermal conductivity, and thermal performance of EG based organic composites.

Name of the Composite	Melting Point (T_m) [°C]	Freezing Point (T_f) [°C]	Latent Heat of Enthalpy (melting) [Jg^{-1}]	Latent Heat of Enthalpy (freezing) [Jg^{-1}]	Thermal Conductivity (Wm^{-1} K^{-1})	Synthesis strategy	Plausible Application	Ref.
Lauric/myristic/SA/EG	29.05	29.38	137.1	131.3	2.51	–	Energy Building, Condensation heat recovery	[128]
Capric–palmitic–SA ternary eutectic mixture/EG composite	21.33	19.01	131.7	127.2	5.225	Soaking/Infiltration	Building energy conservation, solar energy storage, low temperature refrigeration and indoor temperature controlling	[129]
n-octadecane/ polystyrene/EG composite (CPCM4)	27.52	27.28	98.05	88	1.012	Melt blending/ Blending	Solar thermal energy storage systems	[89]
n-octadecane/EG composite	26.37	25.79	184.8	182.1	1.848–2.085	Soaking/Infiltration	Building Application	[130]
Tetradecanol/EG composite	35.35	34.93	202.6	201.2	5.71 (7 wt% EG)	Hydrothermal	–	[94]
PEG/EG composite	18.89	19.09	98.59	97.56	–	VI/Melt blending/ Blending	Indoor energy saving and thermal comfort improvement	[104]
Galactitol/mannitol eutectic mixture//EG composite	152.3	101.1	242.06	175.96	9.439	VI/Melt blending/ Blending	Solar energy harvesting and thermal management electronic devices.	[105]
N-eicosane/EG composite	36.41	36.22	199.4	199.2	4.21 (30 % EG)	VI/Melt blending/ Blending	Electro driven thermal energy storage system	[131]
D-Mannitol/EG composite	151.82	–	267.7	–	11.39 (25 % EG)	VI/Melt blending/ Blending	Solar thermal energy storage or waste heat recovery applications	[126]
Paraffin/EG composite	85.4	–	225	–	20.8	VI/Melt blending/ Blending	Thermal management in the aerospace field.	[75]
Paraffin/EG composite	58.2–58.7	53–53.9	182.9–207.3	183–207.8	~2.3	Ultrasonication+Melt blending	Low-temperature solar thermal system with solar passive heating purposes	[98]
AA/EG composite	105.9	105	158.4	158	3.25	Melt blending/ blending	Medium temperature application	[132]
SA/N-doped Porous Carbon @EG	74.0	59.4	177.7	178.1	2.134	Melt blending/ blending	–	[69]
Beeswax/EG composite	57.3	–	198	–	–	Melt blending/ blending	Low temperature thermal storage application	[133]
Caprylic-nonanoic acid mixture/EG composite	6.94 [CPCM-1] 6.84 °C [CPCM-3]	9.42 9.34	115.29 108.75	115.13 107.67	0.2189 [CPCM-3]	Melt blending/ blending	Application in heating, ventilation, and air cooling (HVAC) systems	[88]
SEBS/Hexadecane/ LDPE/EG composite	–	–	189.84	187.654	1.2402 (Wm^{-1} °C^{-1}) 0.00452	Ultrasonication+Melt blending	Building insulation or the cooling of electronic backdating	[99]
Palmitic Acid-SA/EG composite	63.11	48.86	176.2	175.6	2.56	Melt blending/ blending	Building energy efficiency, solar energy storage, air-conditioning system, utilization of waste heat, and other low-temperature thermal energy storage systems.	[134]
Myristic acid/EG composite	58	48.1	189.5	187.8	2.1	Melt blending/ blending	Air-conditioning system, solar-energy storage, construction energy saving, and surplus-heat utilization	[135]
Capric acid-Paraffin/EG composite	26.3–26.4	22.57–23.1	27.2	25.69	0.455	Melt blending/ blending	Building energy saving, Low temperature solar thermal storage	[136]
Palmitic-SA/EG composite	53.87	54.23	167.47	168.17	4.43	Ultrasonication+Melt blending	TES application	[137]
Erythritol/EG composite	107	64	231.6	–	12.51 (10 wt%)	Melt blending/ blending	Middle temperature application	[108]
Sebacic acid/EG composite	128.19 (5 wt%)	129.4 (2 wt%)	188.4 (2 wt%)	186.2 (2 wt%)	5.353	Soaking/Infiltration	Middle temperature application	[125]
EG/Paraffin	68.3	–	126.87	–	2.418	Melt blending/ blending	–	[138]
EG/Paraffin/olefin block *co*-polymer	48.91	169.5	40.22 °C	162.2	32.8	Melt blending/ blending	Thermal management of electronics	[107]
Hyper-crosslinked polymer/EG/Paraffin	65.08	57.89	157.72	153.35	~5.8	Melt blending/ blending	Solar thermal energy conversion	[106]

(*continued on next page*)

Table 6a (*continued*)

Name of the Composite	Melting Point (T_m) [°C]	Freezing Point (T_f) [°C]	Latent Heat of Enthalpy (melting) [Jg^{-1}]	Latent Heat of Enthalpy (freezing) [Jg^{-1}]	Thermal Conductivity (Wm^{-1} K^{-1})	Synthesis strategy	Plausible Application	Ref.
Carbon fiber/Palmitic acid/EG	~ 63-64	56-57	174.7	176.7	–	Melt blending/ blending	Macroscopic heat transfer device to study its heat transfer behavior.	[139]
s-s PCM/EG	132 °C	–	230	–	21.3	Melt blending/ blending	Solar-thermoelectric generator device	[102]

Table 6b
Summary of synthesis strategies, thermal conductivity, and thermal performance of EG-based inorganic composite.

Name of the Composite	Melting Point (T_m) [°C]	Freezing Point (T_f) [°C]	Latent Heat of Enthalpy (melting) [Jg^{-1}]	Latent Heat of Enthalpy (freezing) [Jg^{-1}]	Thermal Conductivity (Wm^{-1} K^{-1})	Synthesis strategy	Plausible Application	Ref.
Eutectic salts/ ceramics/EG composite	470.6	–	91.32	–	5.10 (15 wt%)	Melt blending/ blending	High temperature solar TES system	[140]
$Ca(NO_3)_2$ -$NaNO_3$/EG composite	219.2/ 265.6	213.0/ 279.1	98.01	96.56	5.659 (7 % EG)	Melt blending/ blending	Middle and High temperature TES application	[76]
$LiNO_3$/KCl-EG composite	166.28	158.2	160.5	130.5	–	Blending	The utilization of waste heat from industries	[109]
$Na_2HPO_4{\cdot}12H_2O$/ SiO_2/EG composite	~9	~42	224 (Total)	–	–	Vacuum Impregnation	Thermal management application	[110]
$CaCl_2.6H_2O$/EG composite	27.11	21.67	118.7	115.7	3.2	Melt blending/ blending	Indoor thermal management	[141]
$Na_2SO_4{\cdot}10H_2O$/EG composite	31.06	23.02	114	105.5	1.96 (7 % EG)	VI or the combination of VI and melt-blending or blending process	Floor heating management	[111]
(KNO_3-$LiNO_3$-Ca $(NO_3)_2$-$CsNO_3$)/EG composite	113.09 ($CsNO_3$ = 0.38 %)	–	87.95	–	15.5	Melt blending/ blending	Medium temperature solar technology-based applications	[142]
Hydrated salt/EG	32.05	17.11	172.3	140.8	3.643	Melt blending	Greenhouse, building energy conservation, textile fibers and thermal protection of electrical devices	[90]

Table 6c
Summary of synthesis strategies, thermal conductivity, and thermal performance of EG-based hybrid composite.

Name of the Composite	Melting Point (T_m) [°C]	Freezing Point (T_f) [°C]	Latent Heat of Enthalpy (melting) [Jg^{-1}]	Latent Heat of Enthalpy (freezing) [Jg^{-1}]	Thermal Conductivity (Wm^{-1} K^{-1})	Synthesis strategy	Plausible Application	Ref.
SA/Co_3O_4/EG composite	69.38 (5%EG)	68.77 (5%EG)	212.91 (5%EG)	216.38 (5%EG)	2.53 (10 % EG)	VI/Melt blending/ Blending	Low-temperature solar energy storage	[78]
Paraffin/calcium carbonate/EG composite	47.5	–	122	–	25.81	Core-shell strategy	TES application	[143]
Paraffin/calcium carbonate/EG composite	48.42		137.4	–	~10.37	Core-shell strategy	Various TES application	[97]
Silicone elastomer containing eutectic alloy/1-Otadecanol/ EG composite	60 42	–	213.4 (MJm^{-3})	–	2.25	Core-shell strategy	Thermal management of device, solar energy utilization and thermoelectric energy harvesting, electric power generation.	[96]
Nano SiC//1-octadecanol/EG composite	61	56.6	219.6	210.8	1.674	The combination of VI, melt-blending/blending and ultrasonication process	Solar thermal storage system, thermal comfort clothing and waste heat recovery	[144]
PEG/VO_2/EG	50.15 67.56	34.73 64.13	104.3	95.13	0.31	VI/Melt blending/ Blending	Thermal management of lithium-ion batteries	[112]
PW/EG@GO	39.2	33.8	158.5	156.1	1.33	VI/Melt blending/ Blending	Temperature control in electronic devices	[46]
Encapsulated PW/EG/ CNT	60.54	54.08	133.78	137.55	2.11	Melt blending and steam explosion strategy	Waste heat recovery, thermos-electric power generation	[87]
Stearic acid/BN/EG	68.1	67.12	186.92	184.58	6.349	Melt blending	Building heating	[113]
Paraffin/EG/Cu	62	55	170	172	2.57	Melt blending	Solar thermal storage technology	[97]

Table 6d
Summary of synthesis strategies, thermal conductivity and thermal performance of CF based composite.

Name of the Composite	Melting Point (T_m) [°C]	Freezing Point (T_f) [°C]	Latent Heat of Enthalpy (melting) [Jg^{-1}]	Latent Heat of Enthalpy (freezing) [Jg^{-1}]	Thermal Conductivity (Wm^{-1} K^{-1})	Synthesis strategy	Plausible Application	Ref.
CF/Paraffin/graphite composite	58.1	47.63	177.69	180.57	3.7 (2 wt% graphite)	The combination of VI, melt-blending/blending and ultrasonication process	TES management	[85]
PEG/CF/MWCNT	67.3	37.3	139.3	138.7	0.597	VI/Melt blending/Blending	Building energy storage application	[48]
SA/porous carbon @ Cu foam	68.5	–	78.5	–	0.81	The combination of VI and melt-blending or blending process	Solar energy utilization and storage	[49]
Ti_2O_3/-eicosane/ PDA/CF	36.4	33.7	200.1	200.6	–	VI/Melt blending/Blending	Thermoregulation, Photo-thermal conversion, Thermal insulation	[77]
PEG/CF composite	66.14	44.18	155	149.83	1.535	The combination of VI, melt-blending/blending and ultrasonication process	TES application	[100]
CF/SA composite	67.4	67.2	149.3	151.2	1.725	VI/Melt blending/Blending	Thermal management applications	[51]
Paraffin wax or RT65/ MWCNT/CF	–	–	–	–	~1.1	The combination of VI, melt-blending/blending and ultrasonication process	TES application	[145]
Paraffin/EG/CF composite	44.68	48.71	113	111.4	–	VI/Melt blending/Blending	Low temperature (40 °C - 50 °C) TES application	[146]
Paraffin/CF composite	60.75	57.51	164.98 (Total)	–	1.198	VI/Melt blending/Blending	TES application	[147]
PAA/CF composite	64.08	58.56	198.2	198.5	–	VI/Melt blending/Blending	Solar thermal energy storage	[80]
PEG/Modified CF	65.7	37.2	170.9	159.2	0.68 (PEG/ CF10)	VI/Melt blending/Blending	Solar energy utilization	[118]
Paraffin wax/CF	59.7	–	110.9	–	5.23	VI/Melt blending/Blending	–	[50]
Superhydrophobic CF/Sugar alcohol	117.6	–	351 ± 15		3.2 (Mixed sugar alcohol)	VI/Melt blending/Blending	Solar thermal energy storage	[52]
SA/CF	71.6	63.7	176.6	179.7	3.23	VI/Melt blending/Blending	Waste heat utilization	[148]
Stearic acid/ graphitized CF	71.6	64	181.8	182.7	1.012	Vacuum impregnation	–	[149]
CF/$CaCl_2.6H_2O$	27.6 27.7 27.3	1.8 1.3 -1.1	173.0 230.5 180.2	156.1 208.9 162.8	0.23-0.42	Squeezing Vacuum impregnation Soaking	–	[101]
Activated carbon/PEG	61.1	37.6	95.4	88.9	0.29	Vacuum impregnation	–	[150]
CF@CNT/PW	40.01	44.69	81.94	80.74	1.548	VI	Smart wear and textile industries	[54]

as an active composite [176]. The configuration of the LHTES system with optimized inner and outer helix radius of the double spiral coil-shaped tube was evaluated by the quasi-steady state method and validated by the 2D numerical model. The area ratio of the inner and outer coil tubes affected the heat storage efficacy of the LHTES system. The change in coil pitch length for the outer and inner tube affects the heat transfer area of the outer and inner tube coil, which is one of the main reasons for high or low heat storage efficiency. The heat storage efficiency and homogeneous heat distribution (13.3 % reduction in melting time during 95 % melting of EG/Paraffin composite) were higher in the LHTES system with double spiral tubes than in single spiral tubes owing to the large surface area of the double spiral tube.

5.2. Numerical models for predicting heat transfer process between 3D carbon and PCM in composite structure and thermal conductivity evaluation

The severe issue associated with predicting the characteristics of phase-change systems is the non-linear nature of the solid-liquid interface. Recently, Mhiri et al. explored the combined effect of graphite and CF in PCM composite on thermal energy storage efficacy through experimental and numerical investigation [85]. A 3D model was created from numerical simulation to validate the experimental data. The general equation based on fluid momentum and Carman–Koseny relationn was utilized to evaluate the liquid fraction of PCM during phase transition to model the change in thermophysical attributes of PCM during phase transition. The energy equation was used to understand the heat transfer between PCM and CF. The authors employed the Krieger-Dougherty model, the Maxwell-Garnett type practical medium theory (EMT) to evaluate the dynamic viscosity and the role of carbon media towards enhanced thermal conduction. The equations are presented in Table 7.

From the melting profile diagram, see Fig. 17a; PCM at the center of the heat source melted first, then PCM at the frame and middle of the CF, respectively. Gradually, PCM melted throughout the framework of the composite. The enhanced heat transfer through CF facilitates the easy melting of PCM. During PCM melting progress, the velocity distribution, see Fig. 17b, was increased due to the convection effect, and this effect became much more promising at the front of the heated wall. The concentrated circulation of heat at the carbon ligament zone indicates efficient heat transfer between the different components of the composite with carbon skeleton rather than a conduction-based heat transfer pathway.

About 2 wt% loading of GNP and the incorporation of CF enhanced

Table 6e
Summary of synthesis strategies, thermal conductivity, and thermal performance of ExFG based composite.

Name of the Composite	Melting Point (T_m) [°C]	Freezing Point (T_f) [°C]	Latent Heat of Enthalpy (melting) [Jg^{-1}]	Latent Heat of Enthalpy (freezing) [Jg^{-1}]	Thermal Conductivity (Wm^{-1} K^{-1})	Synthesis Strategy	Plausible Application	Ref.
Na-MMT/Paraffin (n-hexadecane)/ExFG composite	20.96	12.13	68.95	65.85	1.113	VI/Melt blending/ Blending	Various TES application	[114]
Na-MMT/Paraffin (n-Octadecane)/ExFG composite	30.31	22.8	80.16	78.78	2.119			
Paraffin/ExFG	56.31	60.11	200.2	179.8	0.47 (2 wt% graphite)	Ultrasonication process	LHTES application	[151]
Paraffin/ExFG nanoplatelet		–		–		Melt blending+ Ultrasonication	LHTES application	[152]
ExFG/erythritol/mannitol eutectic composite	115.37	47.72	308.7	123.8	1.66 (10 wt% graphite)	Melt Blending/Blending	Long term TES application	[115]
Paraffin/ExFG sheets	38.9	–	169.02	–	0.46	Melt blending/blending	–	[116]
Capric-myristic–palmitic acid/ExFG composite	17.1	9.7	142.2	139.5	0.180	Ultrasonication+Melt blending	Low temperature heating and cooling application	[103]
Hexadecane/diatomite/ ExFG composite	22.09	17.14	120.8	120.1	~0.4199	VI/Melt blending/ Blending	Indoor air temperature management	[153]
Octadecane/diatomite/ ExFG composite	30.2	24.13	126.1	112.7	0.3510			
Paraffin/diatomite/ ExFG composite	54.87	49.92	63.77	62.83	0.4128			

Table 6f
Summary of synthesis strategies, thermal conductivity and thermal performance of GF based composites.

Name of the Composite	Melting Point (T_m) [°C]	Freezing Point (T_f) [°C]	Latent Heat of Enthalpy (melting) [Jg^{-1}]	Latent Heat of Enthalpy (freezing) [Jg^{-1}]	Thermal Conductivity (Wm^{-1} K^{-1})	Synthesis process	Plausible Application	Ref.
Alkali and alkaline salt/GF	–		–		101 @RT	VI/Melt blending/ Blending	High temperature latent heat storage application	[81]
GF/wood alloy	–		29.2	–	193.74	VI/Melt blending/ Blending	TES application	[154]
Erythritol/GF	118		251.2	–	3.77	Soaking/Infiltration	Several TES applications	[155]
Paraffin wax/GF	–		160	–	2.66	Soaking/Infiltration	Various low temperature TES application	[156]
Erythritol/GF/ CNT	118.85		~313	–	4.1 (1.8 wt% graphite)	Soaking/Infiltration	–	[55]
Paraffin/Porous Al_2O_3@GF	49.3	41.6	115.92	114.39	0.76	VI/Melt blending/ Blending	Various TES application	[117]
$NaNO_3$/GF			162.6		–	–	High temperature application	[157]
Paraffin wax or erythritol/GF	58.9	–	98.2 (for wax)	–	3.61	Soaking/Infiltration	High performance TES application	[158]
Erythritol/GF	125.5	67.6	178.4	123.6	68.71	VI/Melt blending/ Blending	Medium temperature TES application	[121]
High density GF/ $MgCl_2$ Low density GF/$MgCl_2$	708.8	699	225.2-238.5 353.6-379.6	–	269.8 ± 31 37.7 ± 5.4	VI/Melt blending/ Blending	High temperature LHTES application	[122]
Octadecanol/GF	56.3		130	–	5.55	VI/Melt blending/ Blending	Thermal energy storage and conversion	[120]
PEG/GF/CNT	50.31	37.59	128.7	126.52	0.665	Ultrasonication+Melt blending	Solar thermal utilization systems and air-conditioning applications	[119]

27.5 times higher effective thermal conductivity compared to pure PW. The efficient heat transfer pathway created by CF and the introduction of an additional heat transfer pathway by graphite particles help to overcome the percolation threshold. The general equation based on fluid momentum and the Carman–Koseny relation was utilized was also utilized by Fang et al. to investigate the melting and solidification process of paraffin/EG/Cu composite [177]. Wang et al. utilized Maxwell, Maxwell-Eucken, Hamilton Crosser, and Agari-Uno models to evaluate the thermal conductivity of EG/paraffin-based microcapsules [97]. The thermal conductivity was derived from the consideration of the above models; see Table 8, for the relationship between thermal conductivity with volume and mass fraction of the composite. The authors considered EG and PCM and its composite block as the continuous phase having the thermal conductivity of K_1 and the air inside the block as a dispersed phase with thermal conductivity of K_2. is given below,

Table 6g
Summary of synthesis strategies, thermal conductivity, and thermal performance of carbon aerogel-based composite.

Name of the Composite	Melting Point (T_m) [°C]	Freezing Point (T_f) [°C]	Latent Heat of Enthalpy (melting) [Jg^{-1}]	Latent Heat of Enthalpy (freezing), [Jg^{-1}]	Thermal Conductivity ($Wm^{-1}\ K^{-1}$)	Synthesis strategy	Plausible Application	Ref.
LA/CKF@Fe_3O_4	44.5 [CPM-5]	41.5 [CPM-5]	169.4 [CPM-5]	170.6 [CPM-5]	0.467	VI/Melt blending/ Blending	Solar/magnetic energy utilization, magnetocaloric diagnosis, thermal management/ electromagnetic stealth of electronics.	[59]
SA or 1-tetradecanol/ carbon nanofiber aerogel	38.9371.42	32.05 66.79	223.1 262.2	257.4 221.6	0.6206 ± 0.01 0.3727 ± 0.01	VI/Melt blending/ Blending	Thermoelectric devices fabrication to utilize waste heat and solar energy	[159]
CA/Eicosane	35.03	34.36	211.66	209.8	0.48–0.53	VI/Melt blending/ Blending	Various TES application	[160]
Biomass-derived (carrot) CA/Palmitic acid	62.9 60.1	–	196.31 103.22	–	0.253 0.149	VI/Melt blending/ Blending	Thermal management and renewable energy utilization	[60]
HDA/Graphene aerogel	56.8	–	284.5	–	0.263	Vacuum impregnation	Industrial waste heat recovery	[161]
CA/PEG	58.2	37.4	171.5	169.5	0.82	Vacuum impregnation	–	[64]
RGO/EG aerogel/ paraffin	~46.75	–	242.27	–	0.5	Soaking	–	[123]
Paraffin/Ag/Graphene aerogel	~52-53	~45	149.6	–	1.2	Vacuum impregnation	–	[124]
PEG/Kapok fiber/BN aerogel	63.92	–	172.3	–	0.684	VI/Melt blending/ Blending	Moderate temperature TES application	[61]
Graphitized GO erogel/Paraffin composite	41.6	–	225.7	–	~0.91	VI/Melt blending/ Blending	Thermal management application.	[62]
PEG/RGO-HT aerogel	61.12	33.73	175.7	139.4	0.1	Hydrothermal	TES management in complex environment	[95]
PEG/rGO-MI aerogel	60.91	38.24	223.4	205.2	0.15	Vacuum Infiltration	TES management in complex environment	[95]
Graphene aerogel/ octadecanoic acid	~56-57	51	181.8	–	2.635	VI/Melt blending/ Blending	TES application	[162]
Cellulose aerogel/n-octacosane	68.5	48.3	252.9	252.3	0.583	VI/Melt blending/ Blending	Heat storage and thermal regulation	[63]
Graphene aerogel/PEG	63.0 48.9 43.9 35.4	36.5 42.1 34.3 13.0	116.5 176.4 186 94.2	105.4 172.4 183.1 64.6	–	VI/Melt blending/ Blending	Smart thermo-regulating textile	[66]
PPy/CNT-aerogel/PW	58.5	40.4	167.7	165.4	0.64	VI/Melt blending/ Blending	Thermal management	[163]
1-hexadecanamine or Tetradecanamine/ CNT/Graphene aerogel	48.1 ± 0.4 (HDA composite) 41.2 ± 1.6 (TDA composite)	40.1 ± 0.2 (HDA composite) 28.9 ± 0.6 (TDA composite)	248 ± 1.5 (HDA composite) 243.9 ± 1.3 (TDA composite)	248.3 ± 0.9 245.3 ± 0.9	0.532 (TDA composite) 0.524 (HDA composite)	Soaking/ Infiltration	Solar energy conversion and storage	[65]

$$K_1 = \varnothing_{EG} K_{EG} + \varnothing_M K_M \tag{5}$$

$$\varnothing_{EG} = \frac{1}{1 + \left(\frac{1}{\omega_{EG}} - 1\right)\frac{\rho_{EG}}{\rho_M}} = \varnothing_{vol} \tag{6}$$

$$\varnothing_M = 1 - \varnothing_{EG} \tag{7}$$

$\varnothing_{EG}$, $\varnothing_M$, ω_{EG} denotes the volume fraction of EG, the volume fraction of capsule, and mass fraction of EG, respectively. The computational thermal conductivity values of EG/PCM composite derived from the Maxwell-Eucken model and Agari-Uno model are higher than the experimental values because the porosity in the model calculations was not considered. In comparison, the computational values derived from Maxwell and Hamilton-Crosser models are lesser than the experimental values with a high mass fraction of EG loading in the composite structure. The main reason for such observation is the non-continuous matrix structure under consideration and neglecting the effect of thermal conductive chains.

To explain the effect of PPy on improved thermal conductivity of CNT aerogel/PW composite, Tao et al. adopted a molecular simulation study, considering the heat flux and temperature difference at the interface of CNTs before and after the introduction of PPy between CNT aerogel structure [163]. The following equation simulated the inter-tube thermal conductance of CNT,

$$G = Q/_{L\Delta T} \tag{8}$$

where ΔT is the variation in temperature at the interface of CNTs, Q denotes heat flux, and L is the length corresponding to the overlapping zones of two CNTs. The nosé-Hoover method was chosen to evaluate the temperature gradient. Furthermore, the heat transfer attributes of the composite were simulated by considering phonon-overlap energy, the

Table 6h
Summary of synthesis strategies, thermal conductivity, and thermal performance of another 3D carbon-based composites.

Name of the Composite	Melting Point (T_m) [°C]	Freezing Point (T_f) [°C]	Latent Heat of Enthalpy (melting) [Jg^{-1}]	Latent Heat of Enthalpy (freezing) [Jg^{-1}]	Synthesis strategy	Thermal Conductivity (Wm^{-1} K^{-1})	Plausible Application	Ref.
1-TD/carbonized wood	36.92	36.9	165.8	159.8	VI/Melt blending/ Blending	0.669 [axial direction@50 °C]	Thermal management application	[67]
MWCNT/Melamine foam/ Tetradecylamine	38-40	25-32	183.7	201.58	VI/Melt blending/ Blending	0.5715	Building application	[73] [73]
3D RGO/SA/MOF	71.6	62.4	168.7	162.2	Melt-blending or blending process	0.60 ± 0.02	TES storage	[72]
3D porous AC/PEG	58.5	–	51.5	–	Melt blending/blending	–	Building application	[70]
palmitic acid/AC/ graphene nanoplatelet	65.5	174.98	59.6	175.31	VI/Melt blending/ Blending	0.551	Solar thermal energy storage application	[164]
Myristic acid-hybridized diatomite/AC composite	53.62	124.3	53.3	119.4	The combination of VI, melt-blending/ blending and ultrasonication process	0.58	Building applications, low temperature solar thermal energy application	[84]
n-Octadecane/AC	24.8	55.10	28	54.90	Melt blending/blending	–	Building industry, textiles industry, microelectronics	[71].
SA/GHPC composite	72.4	64.1	194.7	192.5	Melt blending/blending	0.970	Low-temperature latent heat storage applications, especially for solar energy storage and waste heat utilization systems	[165]
CF/Paraffin wax/ GNP	58.11	53.15	131.52	126	The combination of VI, melt-blending/ blending and ultrasonication process	~0.75	Energy and environmental applications	[53]
PEG/PU/EG	46.5	34.8	163.5	160.8	VI/Melt blending/ Blending	~27	Lithium-ion battery thermal management	[74]
Activated garlic peel/PW	60.2	53	52.5	51.9	VI/Melt blending/ Blending	–	Waste heat recovery	[166]
N-doped mesoporous carbon/PEG	52.8		133.2		VI/Melt blending/ Blending	4.5	Battery thermal management	[58]
Porous carbon/PEG	52-54	32-34	153.1	147.8	VI/Melt blending/ Blending	–	Multifunctional application	[167]
Yeast derived porous carbon/D-Mannitol	165.23	120.47	173.68	132.37	VI/Melt blending/ Blending		Medium temperature application	[168]
CNT-sponge/PEG	~80		116-117		Soaking/Infiltration	0.31	Thermal therapy	[169]
Hierarchical porous carbon/PW	~49-50		152.21	139.32	VI/Melt blending/ Blending	0.48	Solar-thermal energy conversion and storage	[170]
Carbon coated Cu foam	61.9	56.8	103.3		Soaking/Infiltration	3.94	Thermotherapy	[171]
Silica@graphite	53.36	53.86	95.76	96.04	VI	0.21	–	[172]
Yeast@porous carbon/Mannitol	165.23	121.31	193.45	149.35	VI	1.17	–	[68]
Coconut shell biochar/PEG	~40	~25	153.1	146.3	Ultrasonication	0.515	Low temperature waste heat recovery, thermoregulation comfort in buildings, electronic cooling system	[173]
CNTs@PC(Zn_xCo_{1-x})	~55	~35	~130	~120	Melt Blending	0.96	Waste heat recovery, thermoregulation of body temperature	[174]
Nanofibril Cellulose/ Graphene nanosheet/PEG	~58-60	~32-35	–	–	Magnetic agitation	~19.37	Shape changes induced thermal management	[127]

interactive force between atoms. From the simulated result, there was about 77 % improvement in thermal conductivity at the interface after the introduction of PPy, see Fig. 17c. PPy at the interface acts as an additional inter-tube heat transfer media during the heat transfer process because of the significant temperature difference between inert tube CNT and PPy, as represented in Fig. 17d. As the simulated result shows, the excellent vibrational matching energy between PPy and CNT shown in Fig. 17e, which signifies the enhanced inter-tube heat transfer with negligible phonon scattering. Therefore, the generation of add-on heat transfer media in the presence of PPy and improved heat transfer between CNT with less phonon scattering, induced via interatomic resonance between CNT and PPy, is the sole reason for the enhanced heat transfer mechanism.

5.3. Numerical models for predicting heat transfer process between 3D carbon/PCM composite with environment for building application

Jinshah et al. utilized a simplified temperature transforming numerical model to investigate the thermal performance of EG/organic PCM(OM37) composite slab for the thermal management of building rooftop [178]. The Fourier-Biot heat conduction (assuming latent heat enthalpy for the PCM composite), Robin boundary condition and change in enthalpy with time was considered for this work. According to this condition, the outer surface of the slab will be exposed to the ambient environment, considering the solar radiation. Two different systems, such as, concrete – PCM – Gypsum and PCM – Concrete – Gypsum, was utilized for this study. Considering the 1-D heat transfer model, the Fourier-Biot heat conduction is mathematically expressed as,

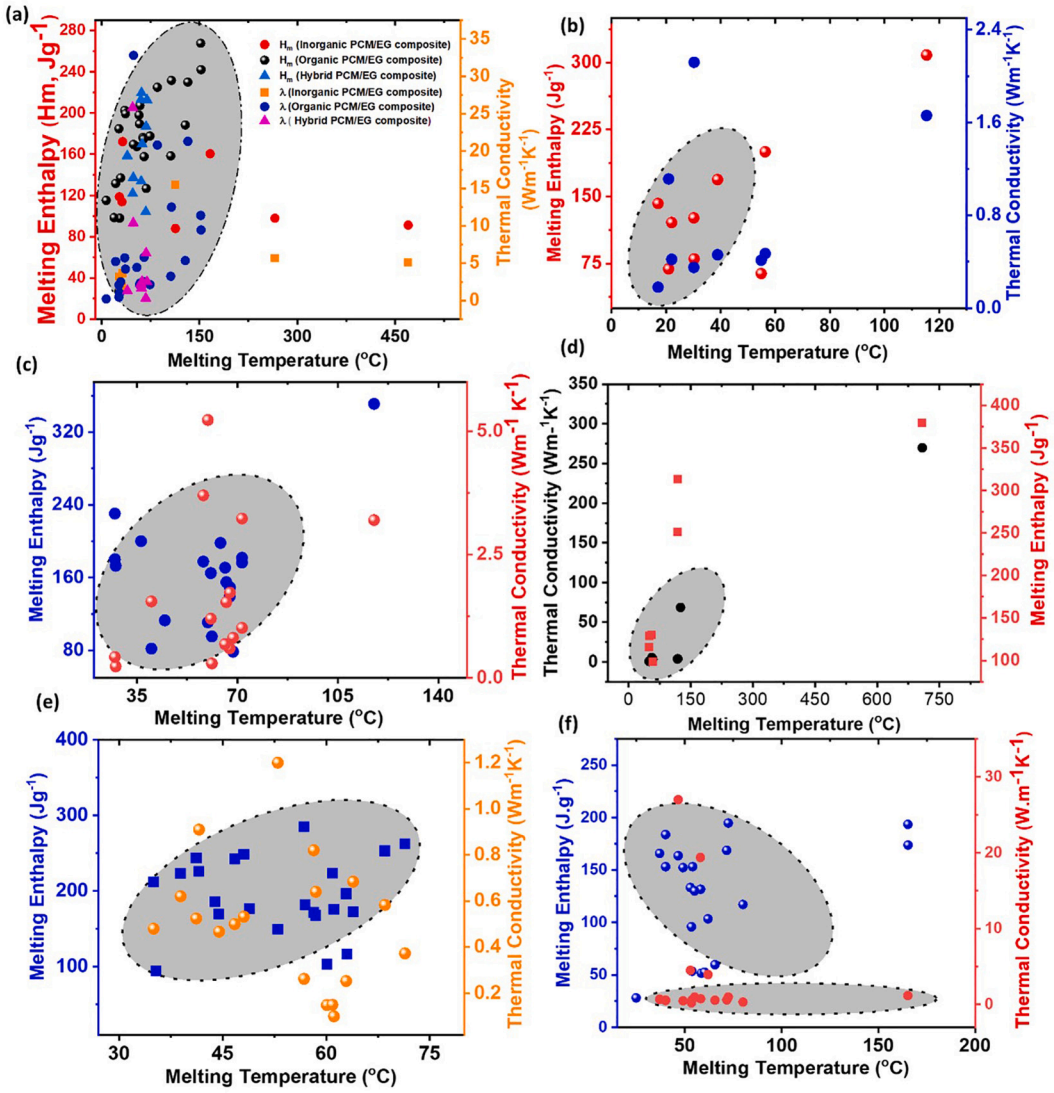

Fig. 16. Phase change enthalpy and thermal conductivity vs. melting temperature based comparative graph for (a) EG (b) ExFG (c) CF (d) GF (e) CA (f) another 3D carbon-based PCM composite. The graph is created based on Tables 6a–6h.

$$\frac{\partial(CT)}{\partial t} = \frac{1}{\rho}\frac{\partial}{\partial x}\left(k.\frac{\partial T}{\partial x}\right) - \frac{\partial \Delta H}{\partial t} \tag{9}$$

The summarization of all types of heat transfer can be written as,

$$\left(k.\frac{\partial T}{\partial x}\right) = q_r + q_{ca} + q_{ins} \tag{10}$$

At$i = 1$ (considering heat exchange occurs with the environment)

$$\left(\mathrm{k}.\frac{\partial T}{\partial x}\right) = q_{cr} \tag{11}$$

Ati = N (considering heat exchange occurs with the room).

The convection to the room and convective heat loss to the environment (q_{cr}, q_{ca}) was evaluated with Newton law of cooling. The radiation heat-transfer co-efficient (q_r) is modeled using a Stefan Boltzmann equation. Eq. (3) is integrated over each control volume. The terms are linearized to obtain the algebraic equation using discrete control volume method, considering the computational domain consists of 'N' number of non-overlapping control volumes. The numerical model is utilized to investigate the effect of the thickness of the PCM slab, wind velocity, and location of PCM for the two above said systems. The temperature rise significantly reduced for both systems with an increase in thickness from 5 mm to 35 mm. With the increase in solar irradiation load from 350 W/m^2 to 1000 W/m^2, the inner surface temperature increment was observed for both systems. The prolonged charging time for the 1st system was due to the heat transfer phenomenon through concrete to PCM.

In contrast, for 2nd system, PCM is directly melted under solar irradiation and stored the heat at the top layer. The high velocity of wind significantly affects the surface temperature of PCM at the top layer. In contrast, wind flow rate almost had minimal impact on the surface temperature when a PCM layer with the same thickness was situated between concrete and Gypsum. At a high wind flow rate, the melting rate of PCM at the top layer was decreased due to rapid convection heat transfer. In 2017, Ye et al. utilized the unsteady energy equation and heat conduction equation of PCM to analyze the thermal performance of EG/$CaCl_2.6H_2O$ composite for energy saving in buildings [141], considering isotropic and constant physical attributes of the material with only convective heat transfer between materials and environment. The governing equation for numerical modeling is given by,

$$\rho C_P \frac{\partial T}{\partial t} = \lambda \times \left(\frac{\partial^2 T}{\partial x^2} + \frac{\partial^2 T}{\partial y^2} + \frac{\partial^2 T}{\partial z^2}\right) \tag{12}$$

Table 7
The corresponding equation utilized for the numerical modeling and purpose of such equation modeling proposed by Mhiri et al. [85].

Name of the Equation	Equation	Purpose
Carman–Koseny relation	$A(T) = \frac{C(1-B(T))^2}{(q+B^3(T))}$ B(T) is the liquid fraction which is associated with change in specific heat during phase transition from solid to liquid. B(T) increases from 0 to1 during phase transition.	The investigation of thermophysical attributes of PCM during phase transition
Energy equation	$\rho_{nf}C_{Pnf}\frac{\partial T_{nf}}{\partial T}+\rho_{nf}C_{Pnf}\underset{u}{\rightarrow}\underset{\nabla}{\rightarrow} T_{nf} = -\underset{\nabla}{\rightarrow}\left(-k_{nf}\underset{\nabla}{\rightarrow}T_{nf}\right)$ *nf* is associated with nanocomposites. *Cp* is specific heat capacity; *k* is thermal conductivity and ρ is the density of PCM composite	Heat transfer of solid and liquid regions within PCM composites
Krieger-Dougherty model	$\mu_{nf} = \frac{\mu_{PCM}}{(1-\varnothing)^{2.5}}$ ∅ is the volume fraction, and *nf* is associated with nanocomposite.	Evaluation of effective dynamic viscosity of the composite
Maxwell-Garnett Effective Medium Theory (EMT)	$k_{nf}=k_d+k_o$ $k_o=k_{PCM}\frac{k_{GNP}+2k_{PCM}-2\varnothing(k_{PCM}-k_{GNP})}{k_{GNP}+2k_{PCM}+\varnothing(k_{PCM}-k_{GNP})}$ k_o is the motionless thermal conductivity of the composite and k_d is the thermal conductivity associated with the Brownian motion of particles under temperature stimuli.	Evaluation of thermal conductivity of the composite

$$\rho_{PCM}\frac{\partial H}{\partial t} = \lambda_{PCM}\times\left(\frac{\partial^2 T}{\partial x^2}+\frac{\partial^2 T}{\partial y^2}+\frac{\partial^2 T}{\partial z^2}\right) \quad (13)$$

T, ρ, C_P, λ, H is temperature, density, specific heat, thermal conductivity, and enthalpy respectively. The finite volume method was used to quantify the equation above using ANSYS FLUENT.

The four pieces of the PCM panels were substituted with one of the four pieces of plasterboard at each insulated test room wall to investigate the thermal management attributes of PCM layers. The effect of change in the location of the PCM panel in the test room was used to analyze the thermal performance of the test room. The test rooms with the PCM panel located at different outside positions were marked as L1 (the PCM panel closer to SIP), L2, L3, and L4. The indoor temperatures of all the rooms were altered periodically with the change in outdoor temperature, and the experimental results agreed with the numerical simulation result. The temperatures in the climatic chamber varied from 10.5 °C to 49.8 °C, while for the reference room, they became 36.5 °C and 18.0 °C, respectively. The decreases in the temperature amplitude signify the low thermal conductivity of the boards used to construct the reference room. However, a PCM panel significantly decreased temperature amplitude compared to the reference room. The significant decrease in maximum temperature and increase in minimum temperature indicate efficient heat absorbed during the daytime and its consecutive release at night. The authors also investigated the effect of the PCM composite panel's position on the room's thermal management. For that purpose, the authors adopted the frequency of thermal comfort and temperature decrement factor concept, and it is mathematically expressed as:

$$\varphi_{PCM} = \tau_{PCM;max} - \tau_{air;max} \quad (14)$$

$$f_{PCM} = \left(t_{PCM;max} - t_{PCM;min}\right)/\left(t_{air;max} - t_{air;min}\right) \quad (15)$$

where φ_{PCM} is the temperature-time lag of the PCM room compared with the reference room; $\tau_{PCM,\ max,}$ and $\tau_{air,\ max}$ are the times when the interior surface maximum temperatures of the PCM room and reference room reach their own highest values, f_{PCM} is the temperature decrement factor of the PCM room compared with the reference room; $t_{PCM,\ max}$ and $t_{PCM,\ min}$ are the maximum and minimum temperatures on the interior surfaces of each PCM room, and $t_{air,\ max,}$ and $t_{air,\ min}$ are the maximum and minimum temperatures on the interior surfaces of the reference room.

$$FTC = (P-\tau_D)/P, \quad (16)$$

where τ_D is the time under discomfort conditions, as the position of the PCM panel changed from outside to the inside of the room, the maximum temperatures of the PCM rooms gently dropped. In contrast, the minimum temperatures hiked minutely. An increased temperature lag, frequency of thermal comfort, and decreased temperature decrement factor were observed for the PCM rooms at varying locations of the PCM panel; see Table 9. Interestingly, the test room with the PCM panels in the nearest positions displayed the best thermal performance. The heat loss to the surroundings during the movement of PCM from inside to outside is the plausible reason for such observation. The authors also compared the performance of such inorganic composite with commercially available RT27/EG composite. The fabricated composite demonstrates improved heat storage performance compared to the commercial RT27/EG composite. The energy-saving rate of the test room with $CaCl_2.6H_2O$/EG and RT27/EG panel was found to be 13.4 % and 12.7 %, respectively. The authors have performed numerical simulations based on unsteady energy and heat conduction to validate the experimental findings. The experimental average relative error of the test room containing PCM was 2.1 %, signifying strong agreement with the practical result. The optimum thickness of the PCM panel was 8-10 mm to obtain the best outcome.

5.4. Numerical models for predicting thermal cooling performance for battery thermal management

Greco et al. introduced a one-dimensional (1D) computational model using the thermal circuit method to investigate battery cooling paraffin/compressed EG-based composite [179]. In this work, the authors used the closed contact between two cylindrical-shaped geometries containing the battery and PCM/EG composite. This model explored the battery's internal heat generation rate per volume and convection on the external surface. The PCM/EG was modeled by one equation with effective physical properties considering the efficient surface contact between PCM and carbon architecture, leading to fast heat transfer rather than natural convection-based heat transfer. The final equation is given below,

$$(\rho C_P)_{eff} = \varepsilon(\rho C_P)_{PCM} + (1-\varepsilon)(\rho C_P)_g; \sigma = \Delta T/2 \quad (17)$$

ΔT represents the melting temperature range of the PCM. ε and C_P is the porosity and specific capacity of the composite.

The analytical solution of the thermal cooling of the battery by PCM/EG with a constant heat generation rate per unit volume, considering the anisotropic thermal conductivity in the battery and cooling of PCM/EG in the radial direction, is given below,

$$T_1(r,t) - T_{amb} = \sum_{n=0}^{n=\infty}\frac{q_1}{\lambda^2{}_{1,n}\alpha_1}\frac{F_n}{H_n}\left(\frac{J_0(\lambda_{2,n}r_1) - \pi(\lambda_{2,n}r_2)Y_0(\lambda_{2,n}r_1)}{J_{0(\lambda_{1,n}r_1)}}\left(J_{0(\lambda_{1,n}r)}\right)\right) \times\left(1-exp\left(\left(-\lambda_{1,n}{}^2\alpha_1 t\right)\right)\right) \quad (18)$$

$$T_2(r,t) - T_{amb} = \sum_{n=0}^{n=\infty}\frac{q_1}{\lambda^2{}_{1,n}\alpha_1}\frac{F_n}{H_n}\left(J_0(\lambda_{2,n}r) - \pi(\lambda_{2,n}r_2)Y_0(\lambda_{2,n}r)\right) \times\left(1-exp\left(\left(-\lambda_{1,n}{}^2\alpha_1 t\right)\right)\right) \quad (19)$$

r_1 denotes the position of the interface battery/CENG in the PCM/EG

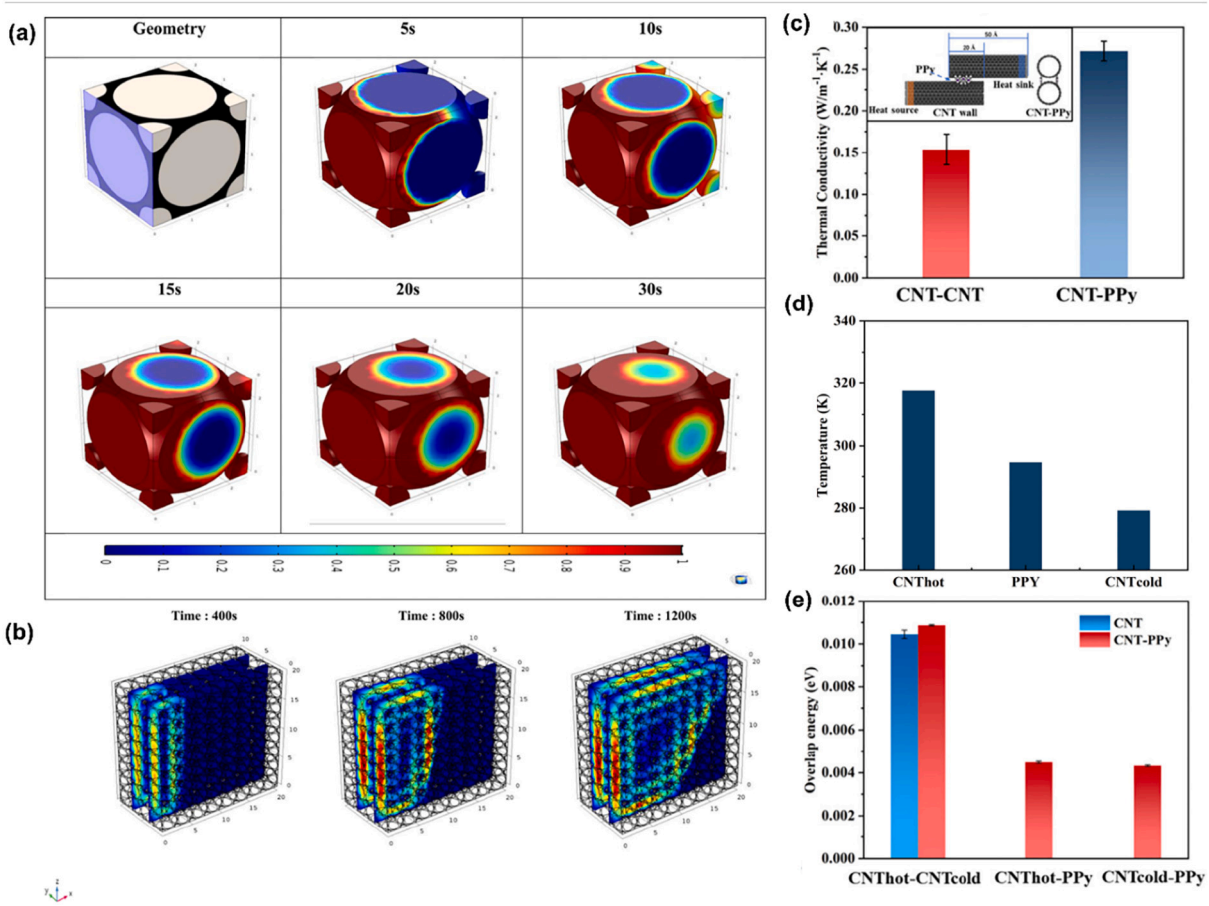

Fig. 17. (a) The simulated heat distribution pictures during melting of PCM in CF architecture (b) The simulated melting profile diagram of CF/graphite nanoparticle/PCM composite [85] (c) A comparative interfacial thermal conductivity diagram of CNT-CNT and CNT-PPy (b) temperature difference of PPy, CNT at the interface during heat transfer (d) overlap energy match level between inter-tube of CNT and PPy-CNT interface during heat transfer (data obtained from molecular dynamics simulations study) [163].

Table 8
The corresponding equation utilized for the numerical modeling by Wang et al. [97].

Name of the Equation	Equation
Maxwell	$K=K_1\frac{K_1+2K_1+2\varnothing_{vol}(K_2-K_1)}{K_2+2K_1-2\varnothing_{vol}(K_2-K_1)}$
Maxwell Eucken	$K=K_1\frac{K_1+2K_1+2\varepsilon(K_2-K_1)}{K_2+2K_1-\varepsilon(K_2-K_1)}$
Hamilton Crosser	$K=K_1\frac{K_1+(n-1)K_1+(n-1)\varnothing_{vol}(K_2-K_1)}{K_2+(n-1)K_1+\varnothing_{vol}(K_2-K_1)}$
Agari-Uno	$K=\frac{2K_1+K_2+2V_{af}(K_2-K_1)}{2K_1+K_2-V_{af}(K_2-K_1)}+V_fV_f^{V_f-2/3}C^2K_2$

Table 9
The temperature profile of the room in the presence of EG/$CaCl_2$. $6H_2O$ composite Panel at the different positions [141].

Location	τ_{max}(h) (PCM room)	Ψ_{PCM} (h)	PCM room temperature (°C)		f_{PCM}	FTC (%)
			Max	Min		
PCM(L1)	18.1	0.7	30.7	21.7	0.486	47.4
PCM(L2)	18.2	0.8	30.5	22.0	0.459	48.7
PCM(L3)	18.5	1.1	30.2	22.4	0.422	53.5
PCM(L4)	18.8	1.4	29.6	22.6	0.378	56.1

cooling case [m], r_2 is the position of the external surface of the PCM/EG composite in the radial direction[m], J_0 is the zero-order Bessel function of the first kind, Y_0 is the zero-order Bessel function of the second kind, α_1 is the thermal diffusivity of the solid, q is the internal heat generation in the battery. The configuration of the battery cell surrounded by the composite and the model describing the battery cooling is presented in Fig. 18a and b.

A 1D computational model based on the thermal network method was developed to introduce the temperature-dependent phase change of the PCM. The domain was divided into a couple of nodes corresponding to the small volume, and the nodes were connected using the thermal conductance parameter. The transient behavior of PCM was modeled by calculating the thermal capacity of each node. In addition, the 1D computational model and 1D analytical solution, considering the latent heat, could predict the temperature rise in the battery. The buffering temperature of PCM was maintained at under 40 °C for 2.9 h while attaining a steady state after 18,000 s, as evaluated using the computational model, while 8000 s were needed to reach the equilibrium as evaluated from the analytical-PCM/EG model. The PCM/EG can decrease the maximum temperature and skin temperature from 75 °C to 45.9 °C and 61 °C to 31.1 °C during battery cooling compared to forced convection cooling.

Moreover, a 3.8 times higher convection coefficient was needed for the forced convection cooling to attain a similar temperature profile to the PCM/EG cooling system, indicating a high energy-consuming process. This observation implies that the PCM/EG may be effectively used in the battery cooling system. The 1D computational model was used to

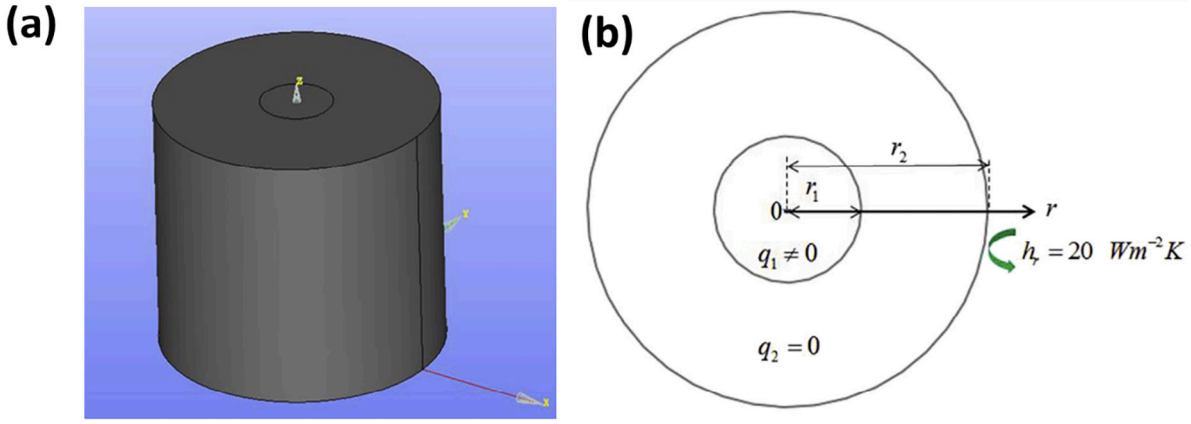

Fig. 18. (a) The configuration of battery coated with PCM/EG composite chosen for numerical modeling and analysis (b) The model used to evaluate the battery cooling phenomenon by the composite [179].

design the PCM/EG from the bulk density. The high bulk density reduces the porosity, decreasing the PCM loading capacity in EG. The reduction in the length of the phase change plateau is the ultimate proof of the ineffectiveness of high bulk-density carbon media. So, the bulk density of carbon media significantly optimizes the cooling performance of PCM/EG composite.

6. Photo, electro, and magneto-thermal energy conversion efficacy of 3D carbon/PCM composites

Researchers continuously strive to design and develop the energy conversion PCM composite that simultaneously converts and stores thermal energy from different sources. To date, carbon-based media is becoming of growing interest to researchers for fabricating energy-conversion PCMs, considering the insulating and weak photo absorption attributes of pristine PCMs. The generation and release of joule heat during the movement of electric current through electrically conductive PCM and released heat storage by PCM are the primary mechanisms of electro-thermal energy conversion and storage by PCM composite [25]. Photo-thermal energy conversion and storage by PCM composite is generally co-related with absorption and transformation of irradiated light energy to heat energy via a couple of photophysical effects (localized plasmonic heating, nonradiative relaxation thermal vibration followed by the storage of heat by PCM [180].

3D carbon foam has been broadly utilized as a supporting media for thermal energy storage and conversion because of enough available pores to accommodate high PCM, excellent electrical conductivity, and photo-sorption capability. Lin et al. reported superior efficacy of PEG/modified CF-based composite towards a light-to-thermal energy conversion and storage [118]. Different CNT concentrations (0 to 10 %) were also introduced into the system to increase the composite's light adsorption and mechanical strength. From the temperature variation curve, the composite reached its melting temperature within 100 s, while >600 s was required for pristine PEG. After 650 s light irradiation, the maximum temperature of the composite reached 87.8 °C, while it was found at 53.8 °C for pristine PEG. Recently, Wang et al. fabricated lightweight and flexible n-eicosane/CF/Ti_2O_3/polydopamine composites to convert photon energy to thermal energy and storage efficiently [77]. The optimized PCM loading (%) to get higher latent enthalpy (200.1 and 200.6 $kJkg^{-1}$ for melting and crystallization) was 84 %. With an increase in Ti_2O_3 nanoparticles from 2.5 % to 7.5 %, a rapid rise in temperature with time was observed under solar light illumination,

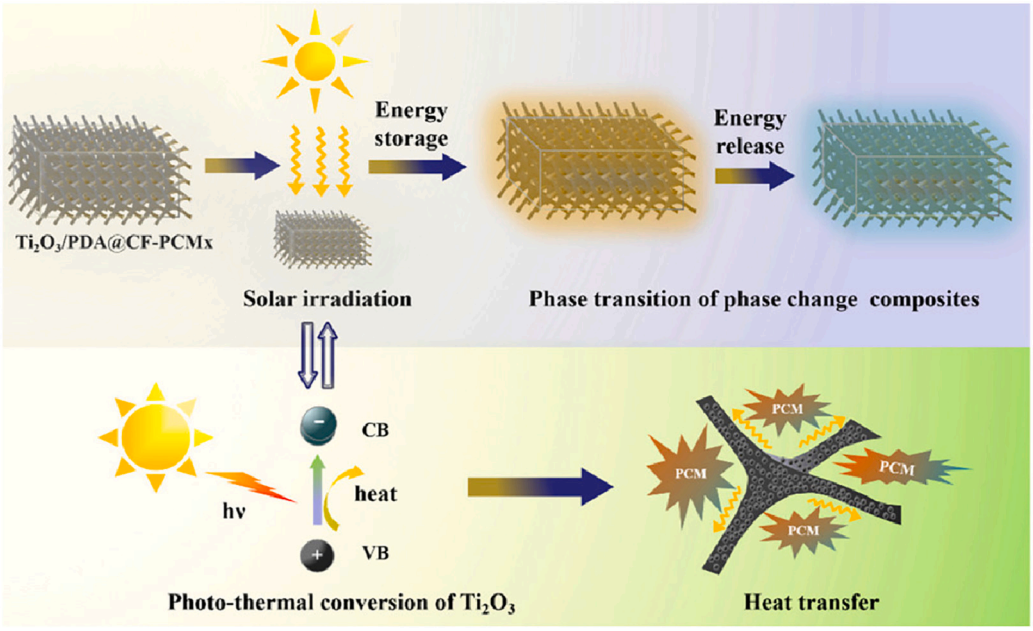

Fig. 19. The plausible mechanism for photothermal energy conversion by n-eicosane/CF/Ti_2O_3/polydopamine composites [77].

indicating efficient conversion of photon energy to thermal energy with an increase in Ti_2O_3 particles owing to its solar energy absorption capability. In the presence of 7.5 % titania particles, the energy storage efficiency of the composite reaches 88.2 %. In the presence of solar light, the generation of e-hole pairs between the valence band and conduction band of Ti induces the conversion of photon energy to heat energy via thermalization. The in-situ generated heat energy is transferred to the inner Ti loading and structure of the composite via titania and stored by PCM. The plausible energy storage mechanism is shown in Fig. 19.

Wang et al. reported enhanced light-to-thermal energy conversion efficacy after combining functionalized CNT with graphene aerogel/Tetradecylamine or hexadecyl amine (TDA or HDA)-based PCM-low D carbon composite [65]. The DSC study revealed that the melting point of PCM did not change, but the supercooling degree significantly reduced in the presence of carbon material. The formation of 3D network architecture offers relatively fast heat transfer and facile crystallization of PCM. The obtained crystallization fraction of CNT/graphene aerogel/HDA with varying CNT/graphite aerogel ratios was reported as 75.6 %, 83.5 %, 84.8 %, 84.1 %, 82.9 %, and 83.3 %, respectively. The observed result signifies the robust cooperation between PCM and the carbon material. In conjugation, the composite demonstrated excellent light-to-thermal conversion efficacy. In the presence of light, PCM did not melt because of its non-IR light absorption attribute. However, the color of porous carbon filler (black) helps absorb IR and UV light simultaneously.

The temperature of the material was increased after reaching the melting point of PCM (23.7 °C – 34.7 °C for HDA and 37-40 °C for TDA). UV–visible graphite aerogel/CNT spectra demonstrate excellent phonon trapping efficacy, consistent with the explanation. After switching the light source, the heat dissipation by the composite started until it reached a crystallization state. The CNT/graphite aerogel ratio shallowly affected the temperature change. A careful observation of the time-dependent heating curve reveals the formation of a plateau during the exponential rise of temperature under light irradiation. This observation signifies the successful transition of PCM from solid to liquid phase in the composite structure. A similar statement was found in the cooling curve due to the reverse phase transition process. The photothermal conversion efficacy for graphite aerogel/HDA-1 and graphite aerogel/CNT/HDA-1 was reported as 72.36 % and 82.33 %, while it appeared for graphite aerogel/TDA-1 and graphite aerogel/CNT/TDA-1 as 74.98 % and 79.36 % respectively. The composite's high thermal conductivity, surface area, and black color facilitate fast and enhanced energy conversion and storage. The excellent chemical stability and repeatability, even after 200 cycles, are another asset of this report. Niu et al. investigated the solar-to-thermal energy conversion and storage performance of two organic PCM-based carbon nanofiber aerogel composites (SA and Tetradecanol)[159]. Under heat treatment, the two organic PCM composites demonstrate a linear and rapid temperature increase observed after the corresponding PCM's phase change temperature.

However, PCM's phase transition time depends entirely on CA's loading, and the high loading of CNFA inhibits the facile melting-cooling process. The thermal energy storage efficiency was 28.9 % and 39.4 % for SA and TD/CNFA composite. The melting and freezing point of SA-based composite was slightly decreased compared to pristine SA due

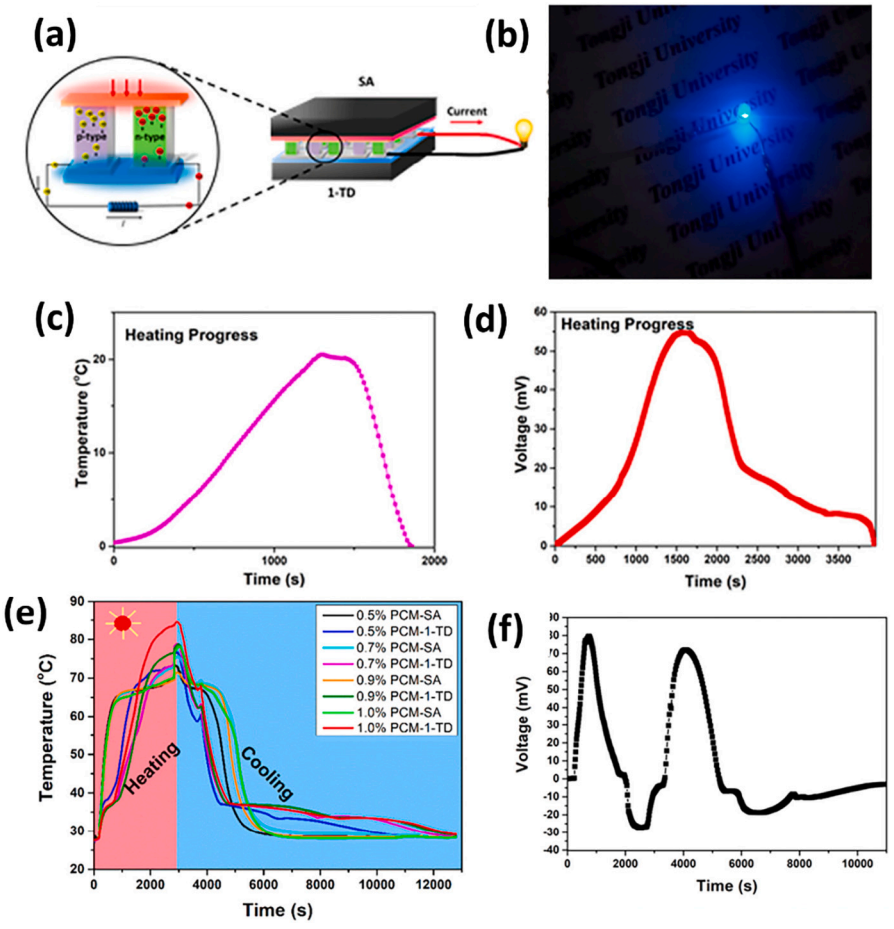

Fig. 20. (a) The structure of energy storage device (b) Turned-on LED light using the harvested electric energy (c, d) Temperature difference between the 0.9 % PCM-SA and 0.7 % PCM-1-TD and generated voltage by the energy harvesting device under heating process (e) Solar-to-thermal energy conversion curves of the PCM-SA and PCM-1-TD samples with different TD or SA loading under sunlight irradiation. (f) The energy harvesting device generates Voltage and short-circuit currentsuring sunlight irradiation and natural cooling progress [159].

to the segregation of CNFA fiber with reduced crystallinity and crystallite size of SA. The author fabricated an energy harvesting device by placing the two different PCM composites on each side of the N and P semiconductor to initiate the temperature difference between the two sides of the device. In the presence of heat, TD-based composites started to melt first due to their low melting point compared to SA-based composites. As a result of the temperature gradient between the two ends, the electrons from the N-type semiconductor move to the other ends, forming the electron concentration gradient.

In the same way, holes also move towards the cold side from the hot side, generating electric current due to e-hole movement. The maximum temperature difference between 1-TD and SA-based composite was 20 °C in the melting process and 15 °C in the cooling process. An LED lamp was inserted into the device to check its employability, and the device's successful conversion of electrical energy is shown in Fig. 20a, b. The device's voltage increased due to temperature differences during the cooling or heating process, see Fig. 20c, d. The lower voltage increment was observed during the cooling process compared to the heating process due to the inferior-temperature gradient. During the cooling or heating, the device generates a short-circuit current due to the lower turn-on voltage of PN junctions (40 mV for the heating and 15 mV for the cooling). The device displayed a maximum power output of 450 μW and 350 μW during the melting and cooling, respectively. The temperature of the PCM composite increased rapidly under solar light irradiation with an increase in CNFA concentration in the composite structure, see Fig. 20e. Thanks to CNFA's excellent phonon scavenging capability and thermal conductivity, such improved composite performance. The authors observed that the significant change in temperature of the two different integrated PCM composites under solar light irradiation was beneficial to the integrated device's rapid voltage increment. The maximum voltage reached by the device during the melting and cooling process was about 80 and 72 mV, respectively. After reaching the cooling point, the device's voltage increased in the negative direction due to the formation of the reverse temperature gradient; see Fig. 20f. Under sunlight, irradiation, and cooling processes, the maximum current generated by the composite reached 13.5 mV and 12 mV, with no negative current during the cooling process due to lower applied voltage than the turn-on voltage of the PN junction. The sunlight-driven power output by the device was reported as 1080 μW while it became 865 μW under the cooling process. Under solar light irradiation, the device demonstrates the successful conversion and storage of solar energy to thermal energy.

Among different fabricated composites, 1 % 1-TD embedded CNFA material shows the maximum rise in temperature of 85 °C within 3000 s. About 96.2 % solar energy conversion was apparent in the presence of 0.7 %-TD embedded CNFA material. This report opens a new strategy to fabricate the semiconductor device for efficient storage of green energy and successful conversion to thermo-electrical energy. Tao et al. observed that the in-situ deposition of PPy on CNT-aerogel/PW significantly revamped the composite's electro-thermal and photo-thermal energy conversion and storage efficacy [163]. Under simulated solar light irradiation (300 W), the hybrid composite demonstrated 90 % photo-thermal energy conversion efficiency, while 91.5 % electro-thermal energy conversion efficiency was apparent under 1.8 V applied bias. The anisotropic architecture of CNT in aerogel structure and the good photo-sorption capability of PPy are responsible for such observation. The successful conversion of magnetic energy to heat via Néel relaxation or Brownian relaxation by magnetic media in the presence of an external magnetic field and storage of released heat in PCM is the primary mechanism associated with magneto-thermal energy conversion and storage by PCM composite [181]. Song et al. fabricated carbonized kapok fiber (CKF)/Fe_3O_4/Lauric acid (LA) based composite for solar/magnetic to thermal energy storage application [59]. Iron oxide and kapok fiber were utilized for their excellent microwave absorption capability, high thermal conductivity, and remarkable photo-thermal conversion efficacy. Altering the Fe_3O_4 content in the composite structure can significantly tune the magneto-thermal conversion efficacy. The fabricated composite displayed efficient conversion and storage of solar energy to thermal energy under different intensity solar light illumination ranges from 700 to 100 Wm^{-2}.

The increase in the light source intensity and content of iron oxide particles in the composite significantly enhances the surface temperature of the material up to 60 °C. The melting and freezing breakup point was apparent for the composite in temperature (°C) vs. time curve, but this breakup point was not evident for pristine PCM.

The black color of the composite plays a pivotal role in the strong absorption of solar energy. The maximum solar energy to thermal energy conversion of fabricated hybrid material is 95 %. Sun et al. manufactured eicosane/porous CA/iron oxide-based composite for thermal energy storage [160]. From the DSC diagram, two exothermic peaks of eicosane were merged for CA/eicosane composite, signifying the change in crystallization of PCM in the composite structure. The maximum eicosane encapsulation ratio (84.09 %) was evident for 20 wt% eicosane-loaded CA composite with iron nitrate concentration, utilized in CA, was about 2 g.

Interestingly, the composite displayed multichannel thermal energy conversion, such as solar-thermal, electro-thermal, and magneto-thermal energy conversion efficacy. The illumination of the DICP character in the circuit board in the presence of PCM composite signifies the efficient electro-thermal conversion efficacy in Fig. 21a. The surface temperature of the composite was changed from 61 to 152 °C with increasing current input from 0.12 to 0.2 A within 200 s under an indigenously current power supply unit. After switching off the current supply, there was immediate temperature dissipation, signifying the fast-cooling process possessed by the composite, see Fig. 21b. The electro-to-thermal conversion efficiency was increased from 47.89 % to 94.83 %, with an increase in current input from 0.12 to 0.2 A. The corresponding IR image of the composite during heating under different current inputs and cooling process under 0.2 A current input during heating is shown in Fig. 21c, d. The higher conversion efficiency of solar to thermal energy for the composite increased from 60.63 to 93.32 %, increasing the IR source's intensity from 200 to 300 $mWcm^{-2}$. The IR image of PCM/CA/Iron oxide composite under 300 mW cm^{-2} solar light irradiation during heating is presented in Fig. 21e. Incorporating PCM and magnetic particles into the composite has a unique attribute towards magneto-thermal energy conversion and thermal energy storage. The magnetic particles can generate heat under magnetic stress and transfer heat to PCM to successfully store the converted energy. The author exploited an alternating current device to generate an alternating magnetic field to explore the magnetic-thermal conversion efficacy of the composite. The simple comparison study of the composite and pristine eicosane with magnetic beads reveals the inherent magnetic attributes of the composite. The composite demonstrated a linear increase in temperature from 47 to 111 °C with an increase in alternating current from 10 to 14 An under the magnetic field irradiation for 350 s, see Fig. 21f.

7. Application area

The variation in phase transition temperature of different PCM and tunable thermal conductivity of other 3D carbon/PCM composites has been exploited in the diversified application arena for the last decades. This section will focus on the possible application area of 3D carbon/PCM composite, including thermal management of batteries, buildings, waste heat recovery, and wearable gadget applications.

7.1. Battery thermal management

In 2022, Bai et al. fabricated PEG/VO_2/EG-based composites for battery thermal management [112]. Thermal conductivity and phase transition temperature are pivotal for battery thermal management applications. The presence of dual-PCM with two melting temperatures

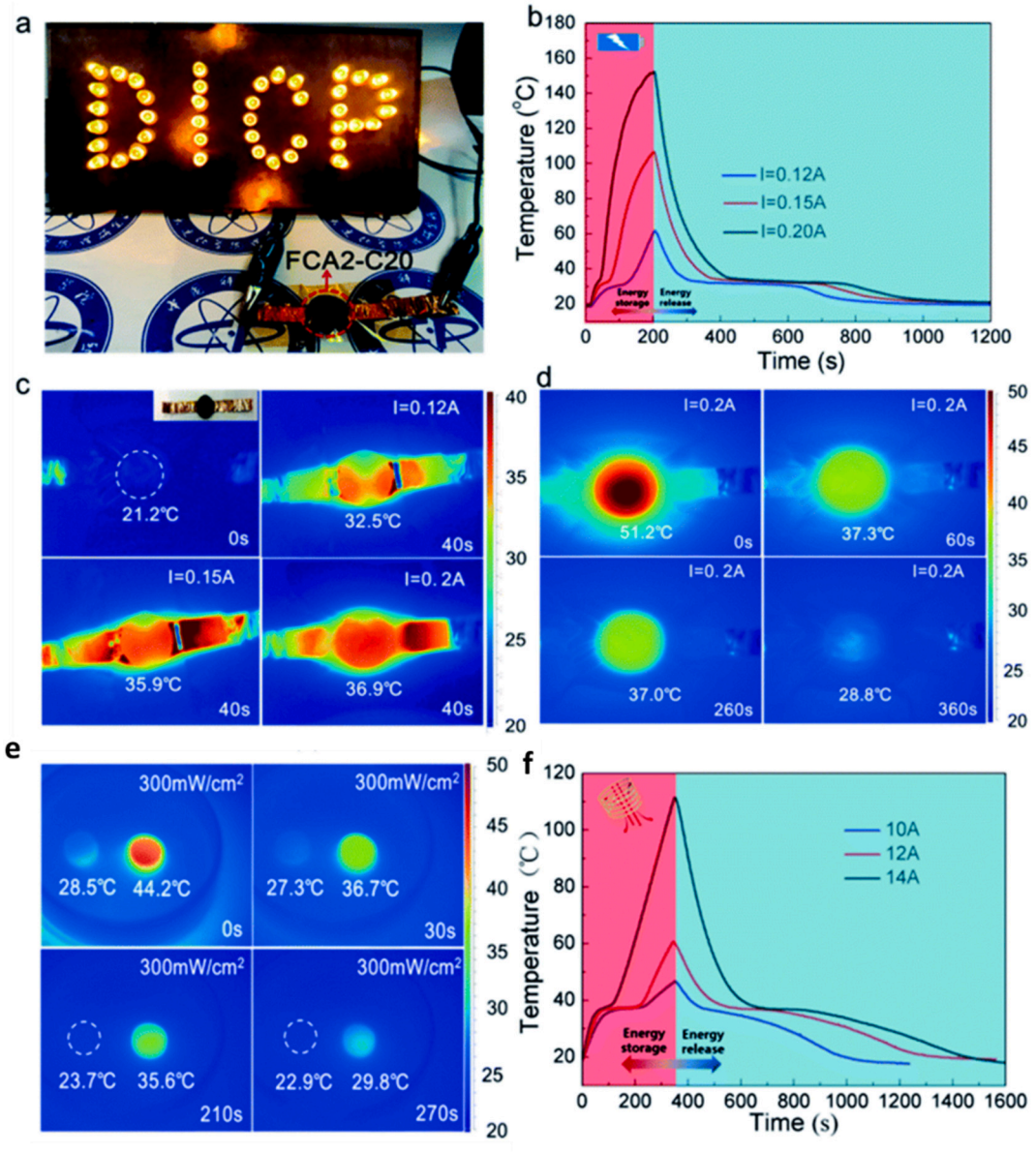

Fig. 21. (a) the illumination of the DICP symbol in the presence of CA/Iron oxide/PCM composite under LED light (b) temperature vs time curve of CA/Iron oxide/PCM composite under different current input, IR image of CA/Iron oxide/PCM composite (c) during heating under different current input (d) during cooling (e) IR image of CA/Iron oxide/PCM composite under solar light illumination (f) temperature vs. time curve of CA/Iron oxide/PCM composite under different alternating current input [160].

of 50.1 °C and 67.56 °C see Fig. 22a, will be beneficial for first and 2nd line defense to induce efficient thermal balance without overcoming its limiting value to explode. The bare lithium-ion battery was kept in a heat-insulating chamber, connected with two T-type thermocouples directly attached to the DC load, see Fig. 22c. The temperature of the empty battery increased linearly up to 165 s. After that, there was a significant increase in the battery's temperature due to the explosion, see Fig. 22b-d. However, the presence of EG-dual PCM composite significantly delays the explosion temperature, indicating an excellent cooling effect of the composite. The temperature difference between the two curves within 260 s is about 20 °C. About 93.75 % increment in thermal conductivity after introducing EG also facilitates dissipating the heat generated during battery heating. Luo et al. reported excellent battery thermal management capacity by newly fabricated N-doped porous carbon/PEG composite [58]. By exploiting the above composite, the author achieved an almost 13 °C reduction in battery pack temperature with a 28 % increment in charge−discharge efficacy. Enhanced PCM loading with high thermal conductivity (up to 4.5 W m^{-1} K^{-1}) induced by N-doping in porous carbon is the potential reason for its improved thermal management.

7.2. *Waste heat utilization/thermo-electric power generation*

Zhou et al. reported the excellent thermoelectric conversion efficacy of SA/CF-based composite [148]. For that purpose, the SA/CF composite was connected at the top surface of the thermos-electric conversion device, and an ice bag as a sink was put under the device. A thermo-electric conversion device, including a fan, was connected to the motor to exploit the fan-induced change of electric energy rotation. From the discharge curve, the device's voltage reached 1.27 V within 34.3 s, followed by a slow decrement of voltage up to 600 s. The thermoelectric conversion device integrated with SA/CF can rotate the fan for over 40 s. The above example may open a new door for successfully utilizing waste heat.

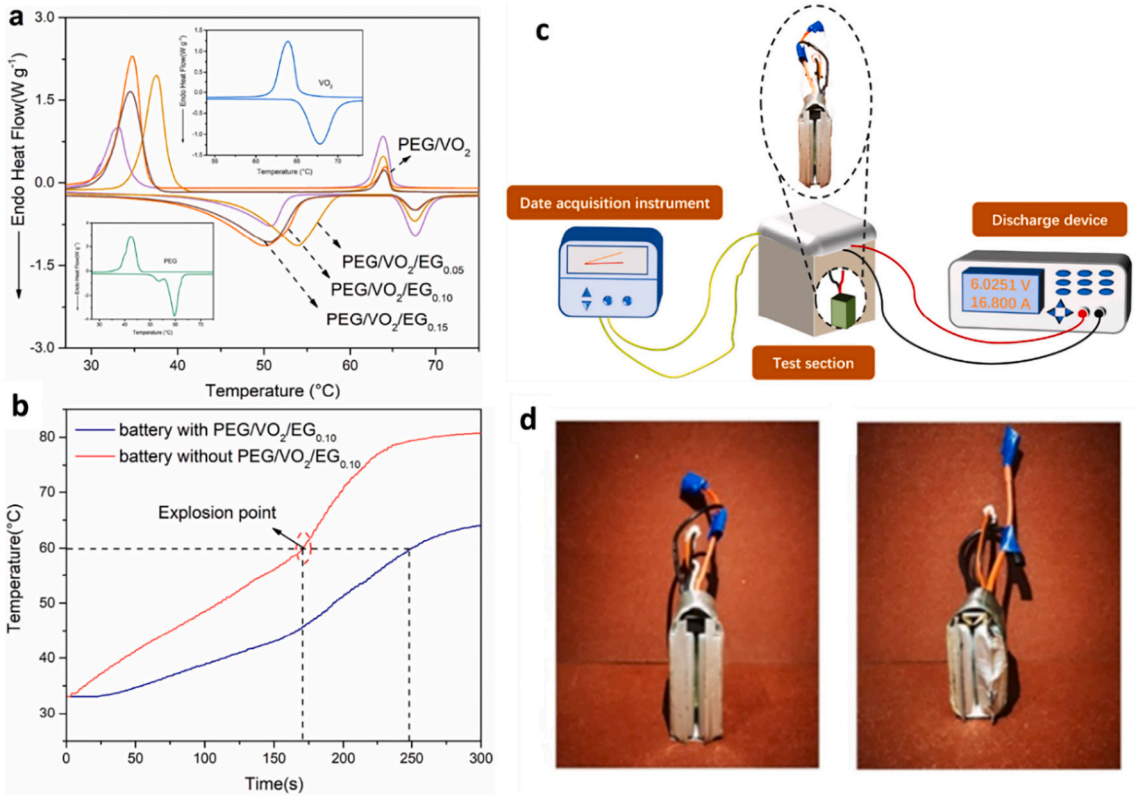

Fig. 22. (a) DSC diagram of EG/PEG/VO_2 based composite with the pristine component (b) Temperature vs. time curves of battery with and without PEG/VO_2/$EG_{0.10}$ composite (c) Indigenously developed experiment setup for the thermal management of lithium-ion battery (d) The photograph of bare battery before and after the explosion [112].

In 2019, Yu et al. integrated the EG-based PCM microcapsule with the thermoelectric generator (TEG) to generate thermoelectric power [96]. For that purpose, the soaked microcapsule was tightly integrated with the hot side of the TEG module for heat discharging and electric power generation.

In contrast, the Al heat sink was attached to the cold side of the TEG module without other power input. As a result, a maximum of 32.1 J current output was obtained from this system. In 2022, Hu et al. exploited a CNT/EG/encapsulated PW-based shape stable composite for efficient waste heat recovery, generating electricity to run a toy car by integrating the composite with a thermoelectric device [87]. In recent, Tang et al. fabricated a high-performance solar thermoelectric device based on 1D/3D hierarchical CNT/porous carbon@Zn0.5$Co_{0.5}$/PEG based composite with the maximum output voltage of 180 μV at a solar light irradiation intensity of 150 $mWcm^{-2}$ [174].

7.3. Thermal management in buildings

Fei et al. incorporated capric-acid-paraffin/EG composite into gypsum board for indoor temperature management [136]. Interestingly, the high amount of EG loading in the composite structure significantly reduces the water absorption capability of the gypsum board. The compressive and flexural strength of the composite decreased at high EG loading in the composite structure. In the presence of a far-infrared heater, the gypsum board's surface temperature was increased from room temperature to ~43 °C for a definite time. However, the maximum change in temperature of the inner and outer surface of the pristine gypsum board and 20 % EG-loaded composite incorporated gypsum board was found at 4.1 °C and 7.4 °C, respectively, due to the temperature difference induced by the source eater exposed to both the inner and outer surface. A slow increase or decrease in temperature during heating or cooling was apparent for high EG-loaded composite compared to pure gypsum or low EG-loaded composite/gypsum. This observation signifies the powerful heat storage capacity of the composite owing to the high thermal conductivity of the hybrid and compact architecture between PCM and EG in the composite structure. The temperature-damping rate is an essential parameter for assessing the heat storage efficacy of any material. High EG loading and IR source with high power intensity significantly enhance the temperature damping rate, which is directly related to the material's solid heat storage and insulation properties. High heat-storing efficacy with modest mechanically stable attributes of such hydrophobic engineered EG material is ideal for indoor application. Maleki et al. fabricated a CF-based PCM composite using different PCM materials, i.e., polyethylene glycol (PEG), palmitic acid (PAA), and paraffin, respectively [80]. Among these three composites, the palmitic acid/CF composite demonstrates high latent heat storage efficacy (198 Jg^{-1}) along with fast thermal response (162 s) and recovery (42 s) compared to others. The authors prepared two wooden test rooms to validate the role of CF/PCM composite for building thermal management, and a heater was inserted into the room.

Almost 75 % of the heater surface in the 2nd room was coated with fabricated composite material, while another in the 1st room was not covered with the material and was considered a reference. Thermocouples were used to measure the temperature of the room and heater surface. The authors also fabricated a solar heating chamber to exploit the composite's excellent solar-thermal energy conversion efficacy. The Cu coil was inserted into the composite, and the two ends of the Cu coil were fitted with the pump and water tank. The whole set-up for water heating and temperature management in the room is shown in Fig. 23a-

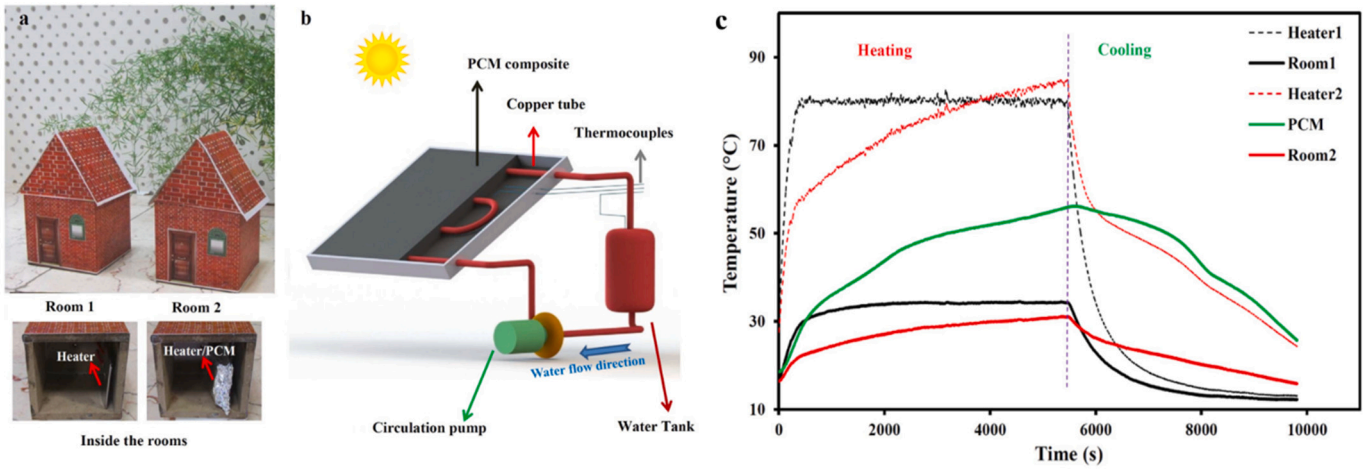

Fig. 23. (a, b, c) The whole set-up for water heating and temperature management in the room using a PCM composite panel [80].

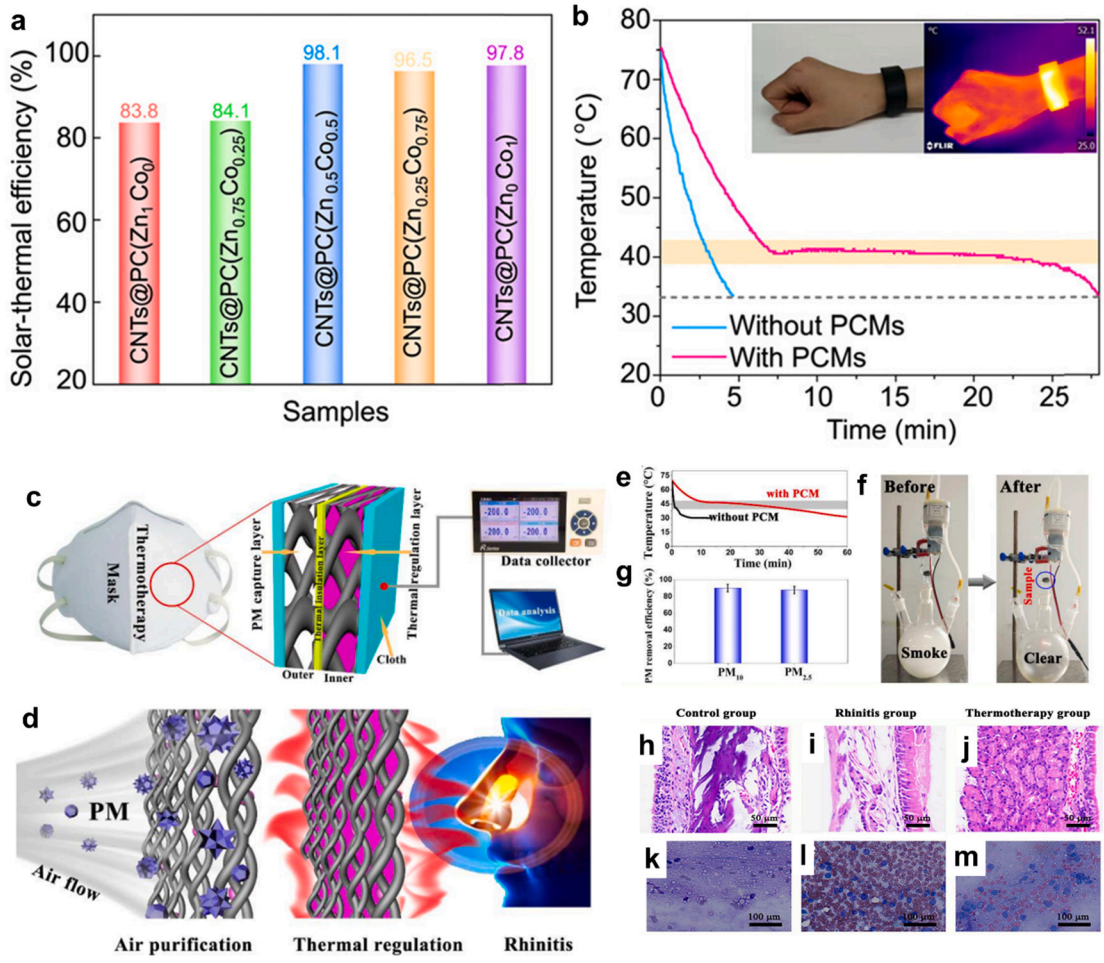

Fig. 24. (a) Solar-thermal energy conversion efficacy of CNT@porous carbon ($Zn_{0.25}$ $Co_{0.25}$)/PEG composite (b) Thermoregulating capability of PCM strip on human skin after solar light irradiation [174], (c) Architectural design of the thermotherapy mask, (b) Thermotherapy and air filtration effect scheme, (d) Heat release performance of the thermoregulatory mask with the control sample, (e) Air purification test with CNT sponge, (f, g) PM removal efficiency of the CNT sponge, (h-m) Optical image consisting nasal tissues of mice with different groups after HE and Wrights staining [169].

b. For the temperature vs. time profile curve of the two-test room, see Fig. 23c, which signifies the improved temperature control efficacy of the composite in the room. The hybrid integrated system demonstrates 88.1 % thermal efficiency with significant heat gain by water from 15 °C to 30 °C.

7.4. Thermotherapy

In 2018, Ye et al. adopted a natural infiltration process to fabricate carbon-coated Cu foam/PW composites for human comfort and thermotherapy-based applications [171]. Carbon coating on Cu foam

was performed via oxidation of Cu foam, followed by PDMS/carbon nanoparticle deposition. The oxidation of Cu foam was carried out to exploit the rough surface of Cu foam for efficient adsorption of carbon nanoparticles. Both PCM (PW) and carbon-coated Cu/PW were charged to 70 °C, followed by cooling at 35 °C, nearly equal to human skin temperature, to investigate the thermal comfort efficacy of the composite on human skin. From IR images, the sharp temperature drop of pristine PCM near the bottom of simulated human skin was eventuated more than the middle or upper side of PCM up to 300 s. Excellent thermal conductivity (3.94 Wm^{-1} K^{-1}) of C-coated Cu foam/PCM heat pack due to the in-situ formation of the thermally conductive network between Cu foam and carbon particles in the composite structure is responsible for homogeneous heat release from the composite structure rather than pristine PW. About 18 times longer healing time was achieved for the composite compared to pristine PW to reach a healing temperature (40 °C). The observed result signifies the potentiality of such a novel composite for thermotherapy-based applications. Recently, Tang et al. developed a unique 1D/3D-CNT/porous carbon@Zn_xCo_{1-x}/PEG-based heterostructure for thermo-regulation of body temperature. The potentiality of this composite lies in its excellent phonon capture capability under solar light irradiation. Excellent solar light absorption capability of 1D/3D carbon heterostructure, fast energy transfer from low D carbon to PCM, phase transition induced thermal energy storage by PEG, and local heating caused by Co nanoparticle via LSPR effect is the primary mechanism of excellent solar-thermal energy conversion efficacy of the heterostructure composite. The high concentration of Co nanoparticles may destroy the core-shell architecture of the system, and the segregation-induced reduction of the localized surface plasmon resonance effect of Co nanoparticles is responsible for poor light-thermal energy storage efficacy, see Fig. 24a. This attribute offers a comparatively more cost-effective and environment-friendly approach to charging the composite strip before utilizing body temperature regulation.

Interestingly, the PCM composite can maintain ~40 °C for 20 min compared to its pristine counterpart, see Fig. 24b [174]. Chen et al. designed and fabricated a CNT sponge/PEG-based mask to treat allergic rhinitis [169]. The architecture of the mask possesses two layers, where the inner layer (CNT sponge/PCM) maintains the thermal balance. In contrast, the outer layer (pure CNT sponge) was associated with air purification, see Fig. 24 **c**, **d**. A cotton insulating layer was inserted between these two layers for effective thermal balance during the crystallization of PEG. The prolonged thermal buffering time (33 min) at 43.5 °C for the PEG/CNT sponge composite compared to the pristine CNT sponge, as seen in Fig. 27c, signifies the tremendous potential of such material in thermotherapy treatment.

Interestingly, the low conductivity of this PCM composite also facilitates preserving the heat inside the nasal area. In conjugation, the excellent PM removal efficiency (89.8 % and 87.5 %) of the CNT sponge was observed in Fig. 24 **e-g**. This observation is mainly attributed to the facile adsorption of PM into *meso* and micropores of the CNT sponge through solid adhesion between the C—N functional group of PM and the C—F group of PVDF in the CNT sponge. An animal experiment was performed on mice to validate the mask's potential efficacy under natural field conditions. The result from the medical trial was also corroborated by a reduced number of eosinophils of nasal mucosa in the presence of a newly fabricated PCM/3D carbon-based mask, Fig. 24h-m.

8. Conclusion and future prospect

This review systematically addresses the recent synthesis strategies of different 3D carbon-based composites and their effect on the prepared composites' morphological and various physicochemical aspects. The different synthesis processes of different 3D carbon and the infiltration processes of PCM in 3D carbon architecture are explored. The role of different 3D carbon towards thermal energy storage and its performance in TES application is also highlighted. Furthermore, different simulation models and the design of varying prototype construction of the reported literature are also discussed to exploit more in-depth heat transfer mechanisms through the 3D network in the composite structure and different application purposes. The summarization of the primary temperature range, highest achieved thermal conductivity, possible application, advantage, and non-explored section of 3D carbon/PCM -based composite is presented in Fig. 25a, b and Table 10 as investigated from several literature reports to obtain a clear-cut idea about on-going research, success, drawback associated with this research topic. The following conclusions and drawbacks are made from the rigorous study and in-depth analysis of the above topic.

- Fig. 25a shows that only GF, EG-based composites were utilized for high-temperature thermal management applications. The maximum thermal conductivity is reported for GF-based PCM composite. At the same time, ~30 W m^{-1} K^{-1} is the typical maximum thermal conductivity of different 3D carbon-based composites, achieved by the researchers, see Fig. 25b. Many materials are still yet to be explored for high-temperature applications. The highest thermal conductivity of the composite appeared for the GF-based PCM composite. So, effort should be put into synthesizing GF-based PCM-based composites with tunable architecture to fabricate high-performance thermal energy storage materials. A careful look at Table 10 reveals that most 3D carbon-based PCM composites possess lightweight, compressible, flexible attributes and low supercooling with high PCM loading capacity. The non-explored section in Table 10 is also beneficial to the readers for the designing and synthesis of

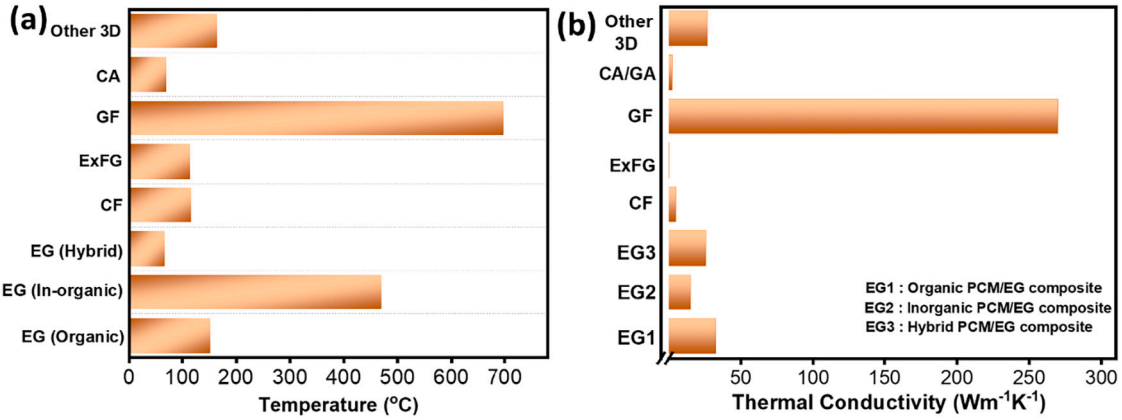

Fig. 25. (a) The average temperature range for which different 3D carbon-based PCM composite was explored for thermal energy storage (b) The maximum thermal conductivity of 3D carbon-based PCM composite achieved based on the literature report.

Table 10
The summary of temperature range, possible application, advantage, and non-explored section of 3D carbon-based composite.

3D Carbon	Advantages of TES Application	Possible TES Application Domain	Non-explored Section
EG	1. Compressible nature, 2. Non-leakage 3. Low supercooling	1. Indoor thermal management, Solar thermal energy storage 2. Thermal management of electronics (Organic EG composite) 3. Floor heating, solar system, waste heat utilization, High-temperature thermal management (Inorganic EG composite) 4. Waste heat recovery, thermos electric energy harvesting, thermal management of electronic devices, and electric power generation	1. High temperature thermal management for organic EG, medium and low-temperature application for Inorganic EG-based composite. 2. Medium and high-temperature applications for Hybrid EG composite are missing. 3. Thermal energy conversion from the different energy sources is explored less for inorganic EG composites.
CF	1. Excellent loading capacity with non-leaking attributes 2. Flexible, lightweight 3. Low supercooling	1. Low-temperature TES application 2. Solar thermal energy storage 3. Building applications	1. High-temperature application. 2. The conversion of thermal energy from different energy sources rather than solar power has been explored less for CF composite.
ExFG	1. Compressible, good loading capacity 2. Simple synthesis process	1. Indoor thermal management, 2. Low and medium temperature application	1. High-temperature application. 2. Thermal energy conversion from different energy sources has been explored less for ExFG composite.
GF	1. Excellent PCM loading capacity with non-leaking attributes, 2. Flexible, lightweight, low supercooling 3. Long-term stability, compressible	Several TES applications (GF)	The conversion of thermal energy from different energy sources rather than solar power has been explored less for GF composite.
CA	1. Excellent PCM loading capacity. 2. Non-leaking attributes, 3. Lightweight, 4. Low supercooling 5. Long-term stability 6. Compressible (CA)	1. Renewable energy utilization 2. Low to medium-temperature application	The report lacks the utilization of carbon aerogel-based composite for high-temperature applications.
Other 3D Carbon	1. Lightweight, 2. Low supercooling 3. Long-term stability depending on the types of other 3D carbons	1. Building, thermos regulating textile, 2. Thermal management of electronics 3. Waste heat utilization and solar thermal energy application	The report lacks the utilization of another 3D-based composite for medium and high-temperature application

engineered 3D carbon/PCM-based composite for several applications.

- The latent energy storage performance of 3D carbon/PCM composite depends entirely on several factors, i.e., latent heat offered by PCM, the thermal resistance at the interface of fillers, PCM-filler junction, and the adherence attributes of PCM with 3D carbon. The adherence attributes of PCM and 3D carbon may be manipulated by surface treatment of 3D carbon. Although it is also challenging to say which is the suitable PCM for fabricating 3D carbon composite, paraffin is the most widely explored PCM to couple with 3D carbon for LHTES application. Hydrophobic-hydrophobic interaction between paraffin and 3D carbon may be exploited for efficient PCM adsorption during the adsorption process. The abundant source of the primary precursor (graphite), its cheap cost, and its simple synthesis procedure are the main benefits of using 3D carbon fillers for LHTES applications. From the literature study, it is observed that high thermal conductivity (maximum ranges from 30 to 269 Wm^{-1} K^{-1}) achievement is possible with 3D carbon/PCM composite compared to other inorganic (Ag nanowire, Fe_3O_4, Cu, ZnO, AlN nanoparticles) or 1D/2D organic filler (carbon fiber, MWCNT, SWCNT) based PCM materials [182–187]. The rigorous data analysis from the literature report shows that vacuum impregnation and adsorption-based methods are the two most popular strategies for fabricating 3D carbon filler-based composite due to their high PCM storage capability and simple, straightforward approach. However, the ultrasonication-assisted adsorption method is slowly arising in this field for LHTES application, but more effort should be put into this synthesis strategy soon. The homogeneous distribution of PCM into the composite is the main achieving point of this approach. It is also noted that the high surface area, the 3D architecture of the 3D carbon fillers, and the porous architecture facilitate PCM loading, which is the essential requirement of high-performance materials employed for TES application.
- Another TES application advantage is the high mechanical strength and flexibility of 3D carbon-based composites. The excellent contact between PCM materials and 3D-carbon decreased the contact resistance and facilitated the heat transport pathway. The high photon absorption capability and electrical conductivity of the 3D carbon are responsible for improved photo-thermal and electro-thermal energy conversion.
- However, some challenges in this research arena are still addressed and must be resolved. The main drawback of such 3D fillers is associated with their synthesis procedure. Most 3D fillers are produced via chemical treatment with a strong inorganic acid or hazardous organic solvent, heat treatment, or a combination of both. Tremendous heat treatment (700 °C -900 °C) is needed to obtain carbon foam or aerogel. As a result, the evolution of many hazardous gases, like CO_2, SO_2, and SO_3, poses a poker-faced request to the environment. Although the composite preparation method is simple and economically efficient, the mass-scale preparation of 3D fillers is still challenging for researchers.
- It is still challenging to compare the effect of different synthesis strategies on the performance of each 3D carbon/PCM composite. The reason behind this is the deployment of different PCMs for fabricating each 3D carbon-based composite, even using a similar synthesis strategy.
- Another essential thrust area in this research is the investigation of the thermal energy storage efficacy of 3D carbon filler/electrospun fiber-based composite. Some literature reports regarding synthesizing 3D carbon-based electrospun fiber are found [188,189] but exploring the phase change fiber towards thermal energy storage using 3D carbon was scarce. The above manufacturing method offers a comparatively higher surface area [190]. This method allows the production of polymer fibers and nonwoven mats in various configurations using co-axial [191] or side-by-side [192] nozzle or multi-nozzle to create composite meshes [193]. The core-shell fibers

have been reported to be effective in absorbing/releasing thermal energy, especially in intelligent textile applications [194,195].

- Although the researchers reported the improved thermal conductivity of the composite in the presence of 3D carbon, the in-depth mechanism of the thermal transport phenomenon through the PCM-3D filler architecture of the composite is still missing. Different numerical models explain the phenomenon; however, the composite system's boundary conditions and exact geometry limit its actual field implementation.
- Compared to the photo-thermal and electro-thermal conversion of energy using 3D carbon filler-based composites, magneto-thermal conversion is not so mature to date, and more research is needed to explore this area. Most literature reports only demonstrate the composite's efficacy in DSC and heating-cooling experiment analysis. The applicability of the materials should be checked in an ambient environment for real-time application purposes. For the fabrication of high-performance 3D carbon-based materials, developing the environmentally stable porous composite with low thermal resistance between 3D carbon and PCM with high surface area is imperative for thermal management.

Optimistically, this review provides an in-depth understanding and a convenient escort for the targeted blueprint of high-caliber 3D-based composite for numerous LHTES applications.

CRediT authorship contribution statement

Madhurima Das: Writing – review & editing, Writing – original draft, Visualization, Validation, Formal analysis, Data curation, Conceptualization. **Urszula Stachewicz:** Writing – review & editing, Writing – original draft, Visualization, Validation, Supervision, Resources, Project administration, Funding acquisition.

Declaration of competing interest

The authors declare that they have no known competing financial interests or personal relationships that could have appeared to influence the work reported in this paper.

Data availability

Data will be made available on request.

Acknowledgment

This study was a part of the BioCom4SavEn project funded by the European Research Council under the European Union's Horizon 2020 Framework Program for Research and Innovation (ERC grant agreement no. 948840).

References

[1] S.C. Peter, Reduction of CO_2 to chemicals and fuels: a solution to global warming and energy crisis, ACS Energy Lett. 3 (2018) 1557–1561, https://doi.org/10.1021/acsenergylett.8b00878.
[2] EIA: World energy consumption to increase 28% by 2040 | Oil & Gas Journal (ogj.com), https://www.eia.gov/todayinenergy/detail.php?id=32912.
[3] https://www.enerdynamics.com/Energy-Currents_Blog/How-Much-Primary-Energy-Is-Wasted-Before-Consumers-See-Value-from-Electricity.aspx.(accessed January 16, 2024).
[4] https://escapewaste.com/electricity-waste-misuse-abuse-at-home-energy-wastage-facts-tips/.
[5] S.P. Neill, A. Angeloudis, P.E. Robins, I. Walkington, S.L. Ward, I. Masters, M. J. Lewis, M. Piano, A. Avdis, M.D. Piggott, G. Aggidis, P. Evans, T.A.A. Adcock, A. Židonis, R. Ahmadian, R. Falconer, Tidal range energy resource and optimization – past perspectives and future challenges, Renew. Energy 127 (2018) 763–778, https://doi.org/10.1016/j.renene.2018.05.007.
[6] J. Wang, P. Nie, B. Ding, S. Dong, X. Hao, H. Dou, X. Zhang, Biomass derived carbon for energy storage devices, J Mater Chem A Mater 5 (2017) 2411–2428, https://doi.org/10.1039/C6TA08742F.
[7] M. Yu, S.H. Hong, Supply–demand balancing for power management in smart grid: a Stackelberg game approach, Appl. Energy 164 (2016) 702–710, https://doi.org/10.1016/j.apenergy.2015.12.039.
[8] X. Chen, P. Cheng, Z. Tang, X. Xu, H. Gao, G. Wang, Carbon-based composite phase change materials for thermal energy storage, transfer, and conversion, Adv. Sci. 8 (2021), https://doi.org/10.1002/advs.202001274.
[9] M. Sun, T. Liu, X. Wang, T. Liu, M. Li, G. Chen, D. Jiang, Roles of thermal energy storage technology for carbon neutrality, Carbon Neutrality 2 (2023) 12, https://doi.org/10.1007/s43979-023-00052-w.
[10] C. Li, B. Xie, Z. He, J. Chen, Y. Long, 3D structure fungi-derived carbon stabilized stearic acid as a composite phase change material for thermal energy storage, Renew. Energy 140 (2019) 862–873, https://doi.org/10.1016/j.renene.2019.03.121.
[11] H. Nazir, M. Batool, F.J. Bolivar Osorio, M. Isaza-Ruiz, X. Xu, K. Vignarooban, P. Phelan, A.M. Kannan Inamuddin, Recent developments in phase change materials for energy storage applications: a review, Int. J. Heat Mass Transf. 129 (2019) 491–523, https://doi.org/10.1016/j.ijheatmasstransfer.2018.09.126.
[12] C. Li, B. Xie, J. Chen, Z. He, Z. Chen, Y. Long, Emerging mineral-coupled composite phase change materials for thermal energy storage, Energy Convers. Manag. 183 (2019) 633–644, https://doi.org/10.1016/j.enconman.2019.01.021.
[13] I. Dincer, On thermal energy storage systems and applications in buildings, Energ. Buildings 34 (2002) 377–388, https://doi.org/10.1016/S0378-7788(01)00126-8.
[14] V.A. Lebedev, A. Elsayed, A. Amer, V. Lebedev, Thermal energy storage by using latent heat storage materials, Int. J. Sci. Eng. Res. 9 (2018).
[15] A. Ribezzo, G. Falciani, L. Bergamasco, M. Fasano, E. Chiavazzo, An overview on the use of additives and preparation procedure in phase change materials for thermal energy storage with a focus on long term applications, J Energy Storage 53 (2022) 105140.
[16] G. Zhu, M. Zou, W. Luo, Y. Huang, W. Chen, X. Hu, X. Jiang, Q. Li, A polyurethane solid–solid phase change material for flexible use in thermal management, Chem. Eng. J. 488 (2024) 150930, https://doi.org/10.1016/j.cej.2024.150930.
[17] C. Alkan, E. Günther, S. Hiebler, Ö.F. Ensari, D. Kahraman, Polyurethanes as solid–solid phase change materials for thermal energy storage, Sol. Energy 86 (2012) 1761–1769, https://doi.org/10.1016/j.solener.2012.03.012.
[18] E.M. Shchukina, M. Graham, Z. Zheng, D.G. Shchukin, Nanoencapsulation of phase change materials for advanced thermal energy storage systems, Chem. Soc. Rev. 47 (2018) 4156–4175, https://doi.org/10.1039/C8CS00099A.
[19] A.S. Fleischer, Types of PCMs and their selection, in: SpringerBriefs in Applied Sciences and Technology, 2015, pp. 37–47, https://doi.org/10.1007/978-3-319-20922-7_3.
[20] https://www.gminsights.com/industry-analysis/phase-change-material-market.
[21] T.X. Li, D.L. Wu, F. He, R.Z. Wang, Experimental investigation on copper foam/hydrated salt composite phase change material for thermal energy storage, Int. J. Heat Mass Transf. 115 (2017) 148–157, https://doi.org/10.1016/j.ijheatmasstransfer.2017.07.056.
[22] A. García-Romero, G. Diarce, J. Ibarretxe, A. Urresti, J.M. Sala, Influence of the experimental conditions on the subcooling of Glauber's salt when used as PCM, Sol. Energy Mater. Sol. Cells 102 (2012) 189–195.
[23] X. Shi, M.R. Yazdani, R. Ajdary, O.J. Rojas, Leakage-proof microencapsulation of phase change materials by emulsification with acetylated cellulose nanofibrils, Carbohydr. Polym. 254 (2021) 117279, https://doi.org/10.1016/j.carbpol.2020.117279.
[24] K. Biswas, Nano-based phase change materials for building energy efficiency*, in: Start-Up Creation, Elsevier, 2016, pp. 183–211, https://doi.org/10.1016/B978-0-08-100546-0.00009-1.
[25] Y. Zhang, M.M. Umair, S. Zhang, B. Tang, Phase change materials for electron-triggered energy conversion and storage: a review, J Mater Chem A Mater 7 (2019) 22218–22228, https://doi.org/10.1039/C9TA06678K.
[26] J. Huang, Y. Liu, J. Lin, J. Su, C. Redshaw, X. Feng, Y. Min, Novel pyrene-based aggregation-induced emission luminogen (AIEgen) composite phase change fibers with satisfactory fluorescence anti-counterfeiting, temperature sensing, and high-temperature warning functions for solar-thermal energy storage, Adv. Compos. Hybrid Mater. 6 (2023), https://doi.org/10.1007/s42114-023-00706-4.
[27] X. Liu, S. Wang, C. Sun, H. Liu, L. Stevens, P.K. Dwomoh, C. Snape, Synthesis of functionalized 3D microporous carbon foams for selective CO2 capture, Chem. Eng. J. 402 (2020) 125459, https://doi.org/10.1016/j.cej.2020.125459.
[28] Y. Guo, S. Wang, K. Ruan, H. Zhang, J. Gu, Highly thermally conductive carbon nanotubes pillared exfoliated graphite/polyimide composites, Npj Flexible Electronics 5 (2021) 16, https://doi.org/10.1038/s41528-021-00113-z.
[29] R.S.R. da Silva, S.S. Oishi, E.C. Botelho, N.G. Ferreira, Carbon foam composites based on expanded graphite for electrochemical application, Diam. Relat. Mater. 103 (2020) 107730, https://doi.org/10.1016/j.diamond.2020.107730.
[30] K.-Y. Shin, J.-Y. Hong, S. Lee, J. Jang, High electrothermal performance of expanded graphite nanoplatelet-based patch heater, J. Mater. Chem. 22 (2012) 23404, https://doi.org/10.1039/c2jm34196d.
[31] A. Raulo, S. Suin, S. Paria, B.B. Khatua, Expanded graphite (EG) as a potential filler in the reduction of percolation threshold of multiwall carbon nanotubes (MWCNT) in the PMMA/HDPE/EG/MWCNT nanocomposites, Polym. Compos. 37 (2016) 2070–2082, https://doi.org/10.1002/pc.23385.
[32] O. Ola, Y. Chen, Y. Zhu, Three-dimensional carbon foam nanocomposites for thermal energy storage, Sol. Energy Mater. Sol. Cells 191 (2019) 297–305, https://doi.org/10.1016/j.solmat.2018.11.037.
[33] Y. Ma, M. Zou, W. Chen, W. Luo, X. Hu, S. Xiao, L. Luo, X. Jiang, Q. Li, A structured phase change material integrated by MXene/AgNWs modified dual-network and polyethylene glycol for energy storage and thermal management,

Appl. Energy 349 (2023) 121658, https://doi.org/10.1016/j.apenergy.2023.121658.
[34] X. Zhang, X. Li, Y. Zhou, C. Hai, Y. Shen, X. Ren, J. Zeng, Enhanced thermal conductivity in a hydrated salt PCM system with reduced graphene oxide aqueous dispersion, RSC Adv. 8 (2018) 1022–1029, https://doi.org/10.1039/C7RA10632G.
[35] B. Unveroglu, F. Dundar, F. Ay, S. Yazici, A. Ata, Expanded graphite epoxy composite bipolar plates for PEM fuel cells, ECS Trans. 41 (2011) 1869.
[36] A. Allahbakhsh, M. Arjmand, Graphene-based phase change composites for energy harvesting and storage: state of the art and future prospects, Carbon N Y 148 (2019) 441–480, https://doi.org/10.1016/j.carbon.2019.04.009.
[37] Graphitic Carbon Foam Market Size In 2021: 6.0% CAGR with Top Countries Data, Why are Graphitic Carbon Foam Industry gaining traction globally? | Latest 91 Pages Report - MarketWatch, (n.d.).
[38] https://www.alliedmarketresearch.com/graphite-market, Graphite Market Size is Projected to Reach USD 21.6 Billion by 2027 at CAGR 5.3% | Valuates Reports – Bloomberg), 2020 (n.d.).
[39] H. Hu, Recent advances of polymeric phase change composites for flexible electronics and thermal energy storage system, Compos B Eng 195 (2020) 108094, https://doi.org/10.1016/j.compositesb.2020.108094.
[40] F. Xue, X. Qi, T. Huang, C. Tang, N. Zhang, Y. Wang, Preparation and application of three-dimensional filler network towards organic phase change materials with high performance and multi-functions, Chem. Eng. J. 419 (2021) 129620, https://doi.org/10.1016/j.cej.2021.129620.
[41] R. Sattar, T. Ishaq, A. Afzal, R. Mukhtar, A. Naz, Phase change material infiltrated 3D porous carbon interconnected composites for thermal energy storage, Energy Sources, Part A: Recovery, Utilization and Environmental Effects 44 (2022), https://doi.org/10.1080/15567036.2022.2058117.
[42] https://www.sciencedirect.com/topics/engineering/expanded-graphite.
[43] D. Zhang, W. Zhang, S. Zhang, X. Ji, L. Li, Synthesis of expanded graphite-based materials for application in lithium-based batteries, J Energy Storage 60 (2023), https://doi.org/10.1016/j.est.2023.106678.
[44] X.H. Wei, L. Liu, J.X. Zhang, J.L. Shi, Q.G. Guo, The preparation and morphology characteristics of exfoliated graphite derived from HClO4–graphite intercalation compounds, Mater. Lett. 64 (2010) 1007–1009, https://doi.org/10.1016/j.matlet.2009.11.025.
[45] D.D.L. Chung, Exfoliation of graphite, J. Mater. Sci. 22 (1987) 4190–4198.
[46] Y. Liang, Z. Tao, Q. Guo, Z. Liu, Sponge gourd-bioinspired phase change material with high thermal conductivity and excellent shape-stability, J Energy Storage 39 (2021) 102634, https://doi.org/10.1016/j.est.2021.102634.
[47] H. Liu, S. Wu, N. Tian, F. Yan, C. You, Y. Yang, Carbon foams: 3D porous carbon materials holding immense potential, J Mater Chem A Mater 8 (2020), https://doi.org/10.1039/d0ta08749a.
[48] F. Lin, W. Zhang, T. Shi, Z. Lv, X. Min, M. Fang, X. Wu, Y. Liu, Z. Huang, Thermally conductive and shape-stabilized polyethylene glycol/carbon foam phase-change composites for thermal energy storage, ChemistrySelect 5 (2020), https://doi.org/10.1002/slct.201904489.
[49] M. Wang, P. Li, F. Yu, Hierarchical porous carbon foam-based phase change composite with enhanced loading capacity and thermal conductivity for efficient thermal energy storage, Renew. Energy 172 (2021) 599–605, https://doi.org/10.1016/j.renene.2021.03.071.
[50] P. Wilson, S. Vijayan, K. Prabhakaran, Thermally conducting microcellular carbon foams as a superior host for wax-based phase change materials, Adv. Eng. Mater. 21 (2019), https://doi.org/10.1002/adem.201801139.
[51] X. Zhang, X. Wang, C. Zhong, Q. Lin, Ultrathin-wall mesoporous surface carbon foam stabilized stearic acid as a desirable phase change material for thermal energy storage, J. Ind. Eng. Chem. 85 (2020) 208–218, https://doi.org/10.1016/j.jiec.2020.02.003.
[52] P. Jana, E. Palomo del Barrio, M. Dubois, M. Duquesne, A. Godin, C. Vautrin-Ul, V. Fierro, G. Medjahdi, A. Celzard, Hydrophobised carbon foams for improved long-term seasonal solar thermal energy storage, Sol. Energy Mater. Sol. Cells 220 (2021) 110849, https://doi.org/10.1016/j.solmat.2020.110849.
[53] O. Ola, Y. Chen, Q. Niu, Y. Xia, T. Mallick, Y. Zhu, Ultralight three-dimensional, carbon-based nanocomposites for thermal energy storage, J. Mater. Sci. Technol. 36 (2020) 70–78, https://doi.org/10.1016/j.jmst.2019.06.014.
[54] F. Cheng, Y. Xu, J. Zhang, L. Wang, H. Zhang, Q. Wan, S. Xu, W. Li, L. Wang, Z. Huang, A novel flexible carbon fiber with carbon nanotubes growing in-situ via chemical vapor deposition to impregnate paraffin for thermal energy application, J Energy Storage 68 (2023) 107718, https://doi.org/10.1016/j.est.2023.107718.
[55] I. Kholmanov, J. Kim, E. Ou, R.S. Ruoff, L. Shi, Continuous carbon nanotube–ultrathin graphite hybrid foams for increased thermal conductivity and suppressed subcooling in composite phase change materials, ACS Nano 9 (2015) 11699–11707, https://doi.org/10.1021/acsnano.5b02917.
[56] J.H. Lee, S.J. Park, Recent advances in preparations and applications of carbon aerogels: a review, Carbon N Y 163 (2020), https://doi.org/10.1016/j.carbon.2020.02.073.
[57] J. Yang, P. Yu, L.-S. Tang, R.-Y. Bao, Z.-Y. Liu, M.-B. Yang, W. Yang, Hierarchically interconnected porous scaffolds for phase change materials with improved thermal conductivity and efficient solar-to-electric energy conversion, Nanoscale 9 (2017) 17704–17709, https://doi.org/10.1039/C7NR05449A.
[58] H. Luo, F. Yu, H. Wu, C. Wang, M. Wang, High-performance heat storage phase change composite by highly aligned N-doped mesoporous carbon for efficient battery thermal management, ACS Appl Energy Mater 6 (2023) 950–959, https://doi.org/10.1021/acsaem.2c03383.
[59] S. Song, H. Ai, W. Zhu, L. Lv, R. Feng, L. Dong, Carbon aerogel based composite phase change material derived from kapok fiber: exceptional microwave absorbility and efficient solar/magnetic to thermal energy storage performance, Compos B Eng 226 (2021) 109330, https://doi.org/10.1016/j.compositesb.2021.109330.
[60] Z. Zou, W. Wu, Y. Wang, D. Drummer, Biomass derived carbon aerogel as an ultrastable skeleton of form-stable phase change materials for efficient thermal energy storage, Mater Res Express 7 (2020) 045601, https://doi.org/10.1088/2053-1591/ab8584.
[61] Q. Zhang, B. Chen, K. Wu, B. Nan, M. Lu, M. Lu, PEG-filled kapok fiber/sodium alginate aerogel loaded phase change composite material with high thermal conductivity and excellent shape stability, Compos. Part A Appl. Sci. Manuf. 143 (2021) 106279, https://doi.org/10.1016/j.compositesa.2021.106279.
[62] Q.-Q. Kong, H. Jia, L.-J. Xie, Z.-C. Tao, X. Yang, D. Liu, G.-H. Sun, Q.-G. Guo, C.-X. Lu, C.-M. Chen, Ultra-high temperature graphitization of three-dimensional large-sized graphene aerogel for the encapsulation of phase change materials, Compos. Part A Appl. Sci. Manuf. 145 (2021) 106391, https://doi.org/10.1016/j.compositesa.2021.106391.
[63] X. Du, J. Qiu, S. Deng, Z. Du, X. Cheng, H. Wang, Alkylated nanofibrillated cellulose/carbon nanotubes aerogels supported form-stable phase change composites with improved *n* -alkanes loading capacity and thermal conductivity, ACS Appl. Mater. Interfaces 12 (2020) 5695–5703, https://doi.org/10.1021/acsami.9b17771.
[64] Q. Zhang, T. Xia, Q. Zhang, Y. Zhu, H. Zhang, F. Xu, L. Sun, X. Wang, Y. Xia, X. Lin, H. Peng, P. Huang, Y. Zou, H. Chu, B. Li, Biomass homogeneity reinforced carbon aerogels derived functional phase-change materials for solar–thermal energy conversion and storage, Energy Environ. Mater. 6 (2023), https://doi.org/10.1002/eem2.12264.
[65] C. Wang, L. Wang, W. Liang, F. Liu, S. Wang, H. Sun, Z. Zhu, A. Li, Enhanced light-to-thermal conversion performance of all-carbon aerogels based form-stable phase change material composites, J. Colloid Interface Sci. 605 (2022) 60–70, https://doi.org/10.1016/j.jcis.2021.07.066.
[66] G. Li, G. Hong, D. Dong, W. Song, X. Zhang, Multiresponsive graphene-aerogel-directed phase-change smart fibers, Adv. Mater. 30 (2018), https://doi.org/10.1002/adma.201801754.
[67] H. Yang, Y. Wang, Q. Yu, G. Cao, X. Sun, R. Yang, Q. Zhang, F. Liu, X. Di, J. Li, C. Wang, G. Li, Low-cost, three-dimension, high thermal conductivity, carbonized wood-based composite phase change materials for thermal energy storage, Energy 159 (2018) 929–936, https://doi.org/10.1016/j.energy.2018.06.207.
[68] X. Lv, T. Tan, D. Cai, X. Zhou, G. Li, W. Zhu, H. Cao, Shape-stable phase change composite for highly efficiency thermal energy storage using metal-organic framework-encapsulated yeast as porous carbon carrier, Sol. Energy Mater. Sol. Cells 257 (2023) 112379, https://doi.org/10.1016/j.solmat.2023.112379.
[69] J. Luo, X. Cheng, W. Ji, Y. Li, Z. Liu, N-doped porous carbon chain with 3D interconnected network structure to modify expanded graphite for efficient thermal energy storage materials, J Energy Storage 47 (2022) 103634, https://doi.org/10.1016/j.est.2021.103634.
[70] X.-M. Zhou, Y.-F. Liu, Study on the preparation of high adsorption activated carbon material and its application as phase change energy storage carrier material, J. Therm. Anal. Calorim. 147 (2022) 8169–8176, https://doi.org/10.1007/s10973-021-11122-5.
[71] A.F. Nicholas, M.Z. Hussein, Z. Zainal, T. Khadiran, The effect of surface area on the properties of shape-stabilized phase change material prepared using palm kernel shell activated carbon, Sci. Rep. 10 (2020) 15047.
[72] A. Li, C. Dong, W. Dong, D.G. Atinafu, H. Gao, X. Chen, G. Wang, Hierarchical 3D reduced graphene porous-carbon-based PCMs for superior thermal energy storage performance, ACS Appl. Mater. Interfaces 10 (2018) 32093–32101, https://doi.org/10.1021/acsami.8b09541.
[73] M. Liu, C. Zhang, Z. Du, W. Zou, Fabrication of shape-stabilized phase change materials with melamine foam/multi-walled carbon nanotubes composite as container, Compos Interfaces 28 (2021) 255–271, https://doi.org/10.1080/09276440.2020.1763151.
[74] M. Wu, T. Li, P. Wang, S. Wu, R. Wang, J. Lin, Dual-encapsulated highly conductive and liquid-free phase change composites enabled by polyurethane/graphite Nanoplatelets hybrid networks for efficient energy storage and thermal management, Small 18 (2022) 2105647, https://doi.org/10.1002/smll.202105647.
[75] X.L. Wang, B. Li, Z.G. Qu, J.F. Zhang, Z.G. Jin, Effects of graphite microstructure evolution on the anisotropic thermal conductivity of expanded graphite/paraffin phase change materials and their thermal energy storage performance, Int. J. Heat Mass Transf. 155 (2020) 119853, https://doi.org/10.1016/j.ijheatmasstransfer.2020.119853.
[76] Y. Ren, C. Xu, M. Yuan, F. Ye, X. Ju, X. Du, Ca(NO3)2-NaNO3/expanded graphite composite as a novel shape-stable phase change material for mid- to high-temperature thermal energy storage, Energy Convers. Manag. 163 (2018) 50–58, https://doi.org/10.1016/j.enconman.2018.02.057.
[77] W. Wang, Y. Cai, M. Du, X. Hou, J. Liu, H. Ke, Q. Wei, Ultralight and flexible carbon foam-based phase change composites with high latent-heat capacity and Photothermal conversion capability, ACS Appl. Mater. Interfaces 11 (2019) 31997–32007, https://doi.org/10.1021/acsami.9b10330.
[78] D. Li, X. Cheng, Y. Li, H. Zou, G. Yu, G. Li, Y. Huang, Effect of MOF derived hierarchical Co3O4/expanded graphite on thermal performance of stearic acid phase change material, Sol. Energy 171 (2018) 142–149, https://doi.org/10.1016/j.solener.2018.06.062.
[79] R. Wang, J. Yu, F. Islam, A. Tahmasebi, S. Lee, Y. Chen, State-of-the-art research and applications of carbon foam composite materials as electrodes for high-capacity lithium batteries, Energy Fuel 34 (2020) 7935–7954, https://doi.org/10.1021/acs.energyfuels.0c01802.

[80] M. Maleki, A. Imani, R. Ahmadi, H. Banna Motejadded Emrooz, A. Beitollahi, Low-cost carbon foam as a practical support for organic phase change materials in thermal management, Appl. Energy 258 (2020) 114108, https://doi.org/10.1016/j.apenergy.2019.114108.
[81] H. Lan, S. Dutta, N. Vahedi, S. Neti, C.E. Romero, A. Oztekin, M. Nappa, R. Ruales, Graphite foam infiltration with mixed chloride salts as PCM for high-temperature latent heat storage applications, Sol. Energy 209 (2020) 505–514, https://doi.org/10.1016/j.solener.2020.09.029.
[82] U. Stachewicz, Microstructure study of fractured polar bear hair for toughening, strengthening, stiffening designs *via* energy dissipation and crack deflection mechanisms in materials, Mol Syst Des Eng 6 (2021) 997–1002, https://doi.org/10.1039/D1ME00066G.
[83] S. Metwally, S. Martínez Comesaña, M. Zarzyka, P.K. Szewczyk, J. E. Karbowniczek, U. Stachewicz, Thermal insulation design bioinspired by microstructure study of penguin feather and polar bear hair, Acta Biomater. 91 (2019) 270–283, https://doi.org/10.1016/j.actbio.2019.04.031.
[84] S.L. Jie Han, Myristic acid-hybridized diatomite composite as a shape-stabilized phase change material for thermal energy storage, RSC Adv. 7 (2017) 22170–22177.
[85] H. Mhiri, A. Jemni, H. Sammouda, Numerical and experimental investigations of melting process of composite material (nanoPCM/carbon foam) used for thermal energy storage, J Energy Storage 29 (2020) 101167, https://doi.org/10.1016/j.est.2019.101167.
[86] M.B. Bigdeli, M. Fasano, Thermal transmittance in graphene based networks for polymer matrix composites, Int. J. Therm. Sci. 117 (2017) 98–105, https://doi.org/10.1016/j.ijthermalsci.2017.03.009.
[87] X. Hu, C. Zhu, H. Wu, X. Li, X. Lu, J. Qu, Large-scale preparation of flexible phase change composites with synergistically enhanced thermally conductive network for efficient low-grade thermal energy recovery and utilization, Compos. Part A Appl. Sci. Manuf. 154 (2022) 106770, https://doi.org/10.1016/j.compositesa.2021.106770.
[88] Z. Wang, S. Liu, G. Ma, S. Xie, G. Du, J. Sun, Y. Jia, Preparation and properties of caprylic-nonanoic acid mixture/expanded graphite composite as phase change material for thermal energy storage, Int. J. Energy Res. 41 (2017) 2555–2564, https://doi.org/10.1002/er.3830.
[89] Z. Zhang, G. Alva, M. Gu, G. Fang, Experimental investigation on n–octadecane/polystyrene/expanded graphite composites as form–stable thermal energy storage materials, Energy 157 (2018) 625–632, https://doi.org/10.1016/j.energy.2018.06.006.
[90] Y. Wu, T. Wang, Hydrated salts/expanded graphite composite with high thermal conductivity as a shape-stabilized phase change material for thermal energy storage, Energy Convers. Manag. 101 (2015) 164–171, https://doi.org/10.1016/j.enconman.2015.05.006.
[91] Y. Song, N. Zhang, Y. Jing, X. Cao, Y. Yuan, F. Haghighat, Experimental and numerical investigation on dodecane/expanded graphite shape-stabilized phase change material for cold energy storage, Energy 189 (2019) 116175, https://doi.org/10.1016/j.energy.2019.116175.
[92] M. Weng, J. Su, J. Lin, J. Huang, Y. Min, Intrinsically lighting absorptive PANI/MXene aerogel encapsulated PEG to construct PCMs with efficient photothermal energy storage and stable reusability, Sol. Energy Mater. Sol. Cells 254 (2023) 112282, https://doi.org/10.1016/j.solmat.2023.112282.
[93] S. Wang, K. Wei, W. Shi, P. Cheng, J. Shi, B. Ma, Study on the rheological properties and phase-change temperature regulation of asphalt modified by high/low-temperature phase change material particles, J Energy Storage 56 (2022) 105970, https://doi.org/10.1016/j.est.2022.105970.
[94] J.-L. Zeng, J. Gan, F.-R. Zhu, S.-B. Yu, Z.-L. Xiao, W.-P. Yan, L. Zhu, Z.-Q. Liu, L.-X. Sun, Z. Cao, Tetradecanol/expanded graphite composite form-stable phase change material for thermal energy storage, Sol. Energy Mater. Sol. Cells 127 (2014) 122–128, https://doi.org/10.1016/j.solmat.2014.04.015.
[95] J. Ding, X. Wu, X. Shen, S. Cui, X. Chen, Form-stable phase change material embedded in three-dimensional reduced graphene aerogel with large latent heat for thermal energy management, Appl. Surf. Sci. 534 (2020) 147612, https://doi.org/10.1016/j.apsusc.2020.147612.
[96] D.-H. Yu, Z.-Z. He, Shape-remodeled macrocapsule of phase change materials for thermal energy storage and thermal management, Appl. Energy 247 (2019) 503–516, https://doi.org/10.1016/j.apenergy.2019.04.072.
[97] T. Wang, S. Wang, W. Wu, Experimental study on effective thermal conductivity of microcapsules based phase change composites, Int. J. Heat Mass Transf. 109 (2017) 930–937, https://doi.org/10.1016/j.ijheatmasstransfer.2017.02.068.
[98] G. Fang, M. Yu, K. Meng, F. Shang, X. Tan, High-performance phase-change materials based on paraffin and expanded graphite for solar thermal energy storage, Energy Fuel 34 (2020), https://doi.org/10.1021/acs.energyfuels.0c00955.
[99] I. Chriaa, M. Karkri, A. Trigui, I. Jedidi, M. Abdelmouleh, C. Boudaya, The performances of expanded graphite on the phase change materials composites for thermal energy storage, Polymer (Guildf) 212 (2021) 123128, https://doi.org/10.1016/j.polymer.2020.123128.
[100] X. Su, S. Jia, G. Lv, D. Yu, A unique strategy for polyethylene glycol/hybrid carbon foam phase change materials: morphologies, Thermal Properties, and Energy Storage Behavior, Materials 11 (2018) 2011, https://doi.org/10.3390/ma11102011.
[101] Y. Jing, K. Dixit, S.N. Schiffres, H. Liu, Carbon foam/$CaCl_2 \cdot 6H_2O$ composite as a phase-change material for thermal energy storage, Energy Fuel 37 (2023) 12381–12390, https://doi.org/10.1021/acs.energyfuels.3c01275.
[102] Y.G.C.W.D.W.Z.J.X.S.Y.D.X.Z.* and D.Z. Zhaofeng Dai, Oriented high thermal conductivity solid−solid phase change materials for mid-temperature solar-thermal energy storage, ACS Appl. Mater. Interfaces 15 (2023) 26863–26871.
[103] B.E. Jebasingh, Exfoliation of graphite by solar irradiation and investigate their thermal property on capric–myristic–palmitic acid/exfoliated graphite composite as phase change material (PCM) for energy storage, J Energy Storage 5 (2016) 70–76, https://doi.org/10.1016/j.est.2015.11.004.
[104] Y. Yang, Y. Pang, Y. Liu, H. Guo, Preparation and thermal properties of polyethylene glycol/expanded graphite as novel form-stable phase change material for indoor energy saving, Mater. Lett. 216 (2018) 220–223, https://doi.org/10.1016/j.matlet.2018.01.025.
[105] T. Wang, Y. Liu, R. Meng, M. Zhang, Thermal performance of galactitol/mannitol eutectic mixture/expanded graphite composite as phase change material for thermal energy harvesting, J Energy Storage 34 (2021), https://doi.org/10.1016/j.est.2020.101997.
[106] C. Liu, Y. Song, Z. Xu, J. Zhao, Z. Rao, Highly efficient thermal energy storage enabled by a hierarchical structured hypercrosslinked polymer/expanded graphite composite, Int. J. Heat Mass Transf. 148 (2020) 119068, https://doi.org/10.1016/j.ijheatmasstransfer.2019.119068.
[107] S. Wu, T. Li, M. Wu, J. Xu, Y. Hu, J. Chao, T. Yan, R. Wang, Highly thermally conductive and flexible phase change composites enabled by polymer/graphite nanoplatelet-based dual networks for efficient thermal management, J Mater Chem A Mater 8 (2020) 20011–20020, https://doi.org/10.1039/D0TA05904H.
[108] M. Yuan, Y. Ren, C. Xu, F. Ye, X. Du, Characterization and stability study of a form-stable erythritol/expanded graphite composite phase change material for thermal energy storage, Renew. Energy 136 (2019) 211–222, https://doi.org/10.1016/j.renene.2018.12.107.
[109] Z. Huang, Z. Luo, X. Gao, X. Fang, Y. Fang, Z. Zhang, Investigations on the thermal stability, long-term reliability of LiNO3/KCl – expanded graphite composite as industrial waste heat storage material and its corrosion properties with metals, Appl. Energy 188 (2017) 521–528, https://doi.org/10.1016/j.apenergy.2016.12.010.
[110] S. Ren, J. Li, B. Zhang, K. Huang, Y. Bai, Preparation of a composite phase change material with high thermal storage capacity using modified expanded graphite as the matrix, Diam. Relat. Mater. 121 (2022) 108736, https://doi.org/10.1016/j.diamond.2021.108736.
[111] C. Li, B. Zhang, B. Xie, X. Zhao, J. Chen, Tailored phase change behavior of Na2SO4·10H2O/expanded graphite composite for thermal energy storage, Energy Convers. Manag. 208 (2020) 112586, https://doi.org/10.1016/j.enconman.2020.112586.
[112] K. Bai, C. Li, B. Xie, D. Zhang, Y. Lv, J. Xiao, M. He, X. Zeng, J. Zeng, J. Chen, Emerging PEG/VO2 dual phase change materials for thermal energy storage, Sol. Energy Mater. Sol. Cells 239 (2022) 111686, https://doi.org/10.1016/j.solmat.2022.111686.
[113] C. Ao, S. Yan, L. Zhao, X. Zhao, Y. Wu, Design of a stearic acid/boron nitride/expanded graphite multifiller synergistic composite phase change material for thermal energy storage, Energy and Built Environment 4 (2023) 557–567, https://doi.org/10.1016/j.enbenv.2022.04.004.
[114] S.-G. Jeong, S. Jin Chang, S. We, S. Kim, Energy efficient thermal storage montmorillonite with phase change material containing exfoliated graphite nanoplatelets, Sol. Energy Mater. Sol. Cells 139 (2015) 65–70, https://doi.org/10.1016/j.solmat.2015.03.010.
[115] J.-L. Zeng, Y.-H. Chen, L. Shu, L.-P. Yu, L. Zhu, L.-B. Song, Z. Cao, L.-X. Sun, Preparation and thermal properties of exfoliated graphite/erythritol/mannitol eutectic composite as form-stable phase change material for thermal energy storage, Sol. Energy Mater. Sol. Cells 178 (2018) 84–90, https://doi.org/10.1016/j.solmat.2018.01.012.
[116] X. Liu, Z. Rao, Experimental study on the thermal performance of graphene and exfoliated graphite sheet for thermal energy storage phase change material, Thermochim. Acta 647 (2017) 15–21, https://doi.org/10.1016/j.tca.2016.11.010.
[117] Y. Li, J. Li, W. Feng, X. Wang, H. Nian, Design and preparation of the phase change materials paraffin/porous Al_2O_3@graphite foams with enhanced heat storage capacity and thermal conductivity, ACS Sustain. Chem. Eng. 5 (2017) 7594–7603, https://doi.org/10.1021/acssuschemeng.7b00889.
[118] F. Lin, X. Zhang, X. Liu, Y. Xu, Z. Sun, L. Zhang, Z. Huang, R. Mi, X. Min, Polyethylene glycol/modified carbon foam composites for efficient light-thermal conversion and storage, Polymer (Guildf) 228 (2021) 123894, https://doi.org/10.1016/j.polymer.2021.123894.
[119] Z. Yu, D. Feng, Y. Feng, X. Zhang, Thermal conductivity and energy storage capacity enhancement and bottleneck of shape-stabilized phase change composites with graphene foam and carbon nanotubes, Compos. Part A Appl. Sci. Manuf. 152 (2022) 106703, https://doi.org/10.1016/j.compositesa.2021.106703.
[120] W. Wu, R. Yao, X. Huang, R. Chen, K. Li, S. Gao, R. Zou, Dual-encapsulation of octadecanol in thermal/electric conductor for enhanced thermoconductivity and efficient energy storage, Mater Chem Front 1 (2017) 1430–1434, https://doi.org/10.1039/C6QM00381H.
[121] H. Zhang, J. Cheng, Q. Wang, D. Xiong, J. Song, Z. Tang, X. Liu, The graphite foam/erythritol composites with ultrahigh thermal conductivity for medium temperature applications, Sol. Energy Mater. Sol. Cells 230 (2021) 111135, https://doi.org/10.1016/j.solmat.2021.111135.
[122] D. Singh, T. Kim, W. Zhao, W. Yu, D.M. France, Development of graphite foam infiltrated with MgCl2 for a latent heat based thermal energy storage (LHTES) system, Renew. Energy 94 (2016) 660–667, https://doi.org/10.1016/j.renene.2016.03.090.

[123] C. Li, D. Zhang, W. Ren, Phase change materials composite based on hybrid aerogel with anisotropic microstructure, Materials 14 (2021) 777, https://doi.org/10.3390/ma14040777.
[124] L. Zhang, Z. Shi, B. Zhang, J. Huang, Silver attached graphene-based aerogel composite phase change material and the enhancement of thermal conductivity, Materials 13 (2020) 3271, https://doi.org/10.3390/ma13153271.
[125] S. Wang, P. Qin, X. Fang, Z. Zhang, S. Wang, X. Liu, A novel sebacic acid/expanded graphite composite phase change material for solar thermal medium-temperature applications, Sol. Energy 99 (2014) 283–290, https://doi.org/10.1016/j.solener.2013.11.018.
[126] T. Xu, Q. Chen, G. Huang, Z. Zhang, X. Gao, S. Lu, Preparation and thermal energy storage properties of d-mannitol/expanded graphite composite phase change material, Sol. Energy Mater. Sol. Cells 155 (2016) 141–146, https://doi.org/10.1016/j.solmat.2016.06.003.
[127] Y. Song, F. Jiang, N. Song, L. Shi, P. Ding, Multilayered structural design of flexible films for smart thermal management, Compos. Part A Appl. Sci. Manuf. 141 (2021) 106222, https://doi.org/10.1016/j.compositesa.2020.106222.
[128] C. Liu, Y. Yuan, N. Zhang, X. Cao, X. Yang, A novel PCM of lauric–myristic–stearic acid/expanded graphite composite for thermal energy storage, Mater. Lett. 120 (2014) 43–46, https://doi.org/10.1016/j.matlet.2014.01.051.
[129] H. Zhang, X. Gao, C. Chen, T. Xu, Y. Fang, Z. Zhang, A capric–palmitic–stearic acid ternary eutectic mixture/expanded graphite composite phase change material for thermal energy storage, Compos. Part A Appl. Sci. Manuf. 87 (2016) 138–145, https://doi.org/10.1016/j.compositesa.2016.04.024.
[130] Z. Zhang, G. Shi, S. Wang, X. Fang, X. Liu, Thermal energy storage cement mortar containing n-octadecane/expanded graphite composite phase change material, Renew. Energy 50 (2013) 670–675, https://doi.org/10.1016/j.renene.2012.08.024.
[131] C. Li, B. Zhang, Q. Liu, N-eicosane/expanded graphite as composite phase change materials for electro-driven thermal energy storage, J Energy Storage 29 (2020) 101339, https://doi.org/10.1016/j.est.2020.101339.
[132] G.T. Nguyen, H.S. Hwang, J. Lee, I. Park, Azelaic acid/expanded graphite composites with high latent heat storage capacity and thermal conductivity at medium temperature, ACS Omega 6 (2021) 8469–8476, https://doi.org/10.1021/acsomega.1c00265.
[133] A. Dinker, M. Agarwal, G. Das Agarwal, Experimental performance analysis of beeswax/expanded graphite composite for thermal energy storage in a shell and tube unit, Int J Green Energy 15 (2018) 585–595, https://doi.org/10.1080/15435075.2018.1525551.
[134] D. Zhou, Y. Zhou, J. Yuan, Y. Liu, Palmitic acid-stearic acid/expanded graphite as form-stable composite phase-change material for latent heat thermal energy storage, J. Nanomater. 2020 (2020) 1–9, https://doi.org/10.1155/2020/1648080.
[135] D. Zhou, J. Yuan, Y. Zhou, Y. Liu, Preparation and characterization of myristic acid/expanded graphite composite phase change materials for thermal energy storage, Sci. Rep. 10 (2020) 10889, https://doi.org/10.1038/s41598-020-67849-y.
[136] H. Fei, L. Wang, Q. He, W. Du, Q. Gu, Y. Pan, Preparation and properties of a composite phase change energy storage gypsum board based on capric acid-paraffin/expanded graphite, ACS Omega 6 (2021) 6144–6152, https://doi.org/10.1021/acsomega.0c05058.
[137] Y. Yuan, N. Zhang, T. Li, X. Cao, W. Long, Thermal performance enhancement of palmitic-stearic acid by adding graphene nanoplatelets and expanded graphite for thermal energy storage: a comparative study, Energy 97 (2016) 488–497, https://doi.org/10.1016/j.energy.2015.12.115.
[138] S.P. Venkatesan, B.R. Nagendra, C.R. Ram, S. Venkatesh, M. Purusothaman, The effect of expanded graphite on the performance of paraffin phase change materials used in thermal energy storage, J. Phys. Conf. Ser. 2054 (2021) 012071, https://doi.org/10.1088/1742-6596/2054/1/012071.
[139] L. Gao, X. Sun, B. Sun, D. Che, S. Li, Z. Liu, Preparation and thermal properties of palmitic acid/expanded graphite/carbon fiber composite phase change materials for thermal energy storage, J. Therm. Anal. Calorim. 141 (2020) 25–35, https://doi.org/10.1007/s10973-019-08755-y.
[140] X. Ran, H. Wang, Y. Zhong, F. Zhang, J. Lin, H. Zou, Z. Dai, B. An, Thermal properties of eutectic salts/ceramics/expanded graphite composite phase change materials for high-temperature thermal energy storage, Sol. Energy Mater. Sol. Cells 225 (2021) 111047, https://doi.org/10.1016/j.solmat.2021.111047.
[141] R. Ye, W. Lin, K. Yuan, X. Fang, Z. Zhang, Experimental and numerical investigations on the thermal performance of building plane containing CaCl2·6H2O/expanded graphite composite phase change material, Appl. Energy 193 (2017) 325–335, https://doi.org/10.1016/j.apenergy.2017.02.049.
[142] Z. Li, Z.-G. Wu, Development of medium-temperature composite phase change material with high thermal stability and conductivity, Sol. Energy Mater. Sol. Cells 155 (2016) 341–347, https://doi.org/10.1016/j.solmat.2016.06.027.
[143] T. Wang, Y. Jiang, J. Huang, S. Wang, High thermal conductive paraffin/calcium carbonate phase change microcapsules based composites with different carbon network, Appl. Energy 218 (2018) 184–191, https://doi.org/10.1016/j.apenergy.2018.02.108.
[144] S. Gong, X. Cheng, Y. Li, X. Wang, Y. Wang, H. Zhong, Effect of nano-SiC on thermal properties of expanded graphite/1-octadecanol composite materials for thermal energy storage, Powder Technol. 367 (2020) 32–39, https://doi.org/10.1016/j.powtec.2020.03.039.
[145] S.A. Nada, W.G. Alshaer, Experimental investigation of thermal conductivity enhancement of carbon foam saturated with PCM and PCM/MWCNTs composite for energy storage systems, Heat Mass Transf. 55 (2019) 2667–2677, https://doi.org/10.1007/s00231-019-02610-4.
[146] Z. Yin, Z. Huang, R. Wen, X. Zhang, B. Tan, Y. Liu, X. Wu, M. Fang, Preparation and thermal properties of phase change materials based on paraffin with expanded graphite and carbon foams prepared from sucroses, RSC Adv. 6 (2016) 95085–95091, https://doi.org/10.1039/C6RA13758J.
[147] X. Xiao, P. Zhang, Morphologies and thermal characterization of paraffin/carbon foam composite phase change material, Sol. Energy Mater. Sol. Cells 117 (2013) 451–461, https://doi.org/10.1016/j.solmat.2013.06.037.
[148] Y. Zhou, Y. Cao, H. Chen, R. Wu, H. Cheng, F. Luo, Q. Qian, Q. Chen, Q. Lin, Three-dimensional continuous network graphite nanosheets-based carbon foam supported stearic acid as effective shape-stabilized phase change material, J Energy Storage 59 (2023) 106575, https://doi.org/10.1016/j.est.2022.106575.
[149] R. Wu, W. Gao, Y. Zhou, Z. Wang, Q. Lin, A novel three-dimensional network-based stearic acid/graphitized carbon foam composite as high-performance shape-stabilized phase change material for thermal energy storage, Compos B Eng 225 (2021) 109318, https://doi.org/10.1016/j.compositesb.2021.109318.
[150] R. Zheng, Z. Cai, C. Wang, J. Shen, S. Xie, Z. Qi, Form-stable polyethylene glycol/activated carbon composite phase change materials for thermal energy storage, J. Therm. Anal. Calorim. 148 (2023) 9937–9946, https://doi.org/10.1007/s10973-023-12355-2.
[151] J. Huang, T.Y. Wang, C.H. Wang, Z.H. Rao, Exfoliated graphite/paraffin nanocomposites as phase change materials for thermal energy storage application, Mater. Res. Innov. 15 (2011) 422–431, https://doi.org/10.1179/1433075X11Y.0000000004.
[152] A. Mallow, O. Abdelaziz, K. Kalaitzidou, S. Graham, Investigation of the stability of paraffin–exfoliated graphite nanoplatelet composites for latent heat thermal storage systems, J. Mater. Chem. 22 (2012) 24469, https://doi.org/10.1039/c2jm35112a.
[153] S.-G. Jeong, J. Jeon, O. Chung, S. Kim, S. Kim, Evaluation of PCM/diatomite composites using exfoliated graphite nanoplatelets (xGnP) to improve thermal properties, J. Therm. Anal. Calorim. 114 (2013) 689–698, https://doi.org/10.1007/s10973-013-3008-4.
[154] Y. Zhong, Q. Guo, S. Li, J. Shi, L. Liu, Thermal and mechanical properties of graphite foam/Wood's alloy composite for thermal energy storage, Carbon N Y 48 (2010) 1689–1692, https://doi.org/10.1016/j.carbon.2010.01.002.
[155] M. Karthik, A. Faik, P. Blanco-Rodríguez, J. Rodríguez-Aseguinolaza, B. D'Aguanno, Preparation of erythritol–graphite foam phase change composite with enhanced thermal conductivity for thermal energy storage applications, Carbon N Y 94 (2015) 266–276, https://doi.org/10.1016/j.carbon.2015.06.075.
[156] M. Karthik, A. Faik, B. D'Aguanno, Graphite foam as interpenetrating matrices for phase change paraffin wax: a candidate composite for low temperature thermal energy storage, Sol. Energy Mater. Sol. Cells 172 (2017) 324–334, https://doi.org/10.1016/j.solmat.2017.08.004.
[157] P. Giménez, A. Jové, C. Prieto, S. Fereres, Effect of an increased thermal contact resistance in a salt PCM-graphite foam composite TES system, Renew. Energy 106 (2017) 321–334, https://doi.org/10.1016/j.renene.2017.01.032.
[158] H. Ji, D.P. Sellan, M.T. Pettes, X. Kong, J. Ji, L. Shi, R.S. Ruoff, Enhanced thermal conductivity of phase change materials with ultrathin-graphite foams for thermal energy storage, Energy Environ. Sci. 7 (2014) 1185–1192, https://doi.org/10.1039/C3EE42573H.
[159] Z. Niu, W. Yuan, Highly efficient Thermo- and sunlight-driven energy storage for thermo-electric energy harvesting using sustainable nanocellulose-derived carbon aerogels embedded phase change materials, ACS Sustain. Chem. Eng. 7 (2019) 17523–17534, https://doi.org/10.1021/acssuschemeng.9b05015.
[160] K. Sun, Y. Kou, H. Dong, S. Ye, D. Zhao, J. Liu, Q. Shi, The design of phase change materials with carbon aerogel composites for multi-responsive thermal energy capture and storage, J Mater Chem A Mater 9 (2021) 1213–1220, https://doi.org/10.1039/D0TA09035B.
[161] L. Jiang, G. Chen, L. Zhao, M. Li, C. Li, R. Zhang, Preparation and low temperature heat storage properties of 1-hexadecylamine/3D graphene aerogel composite phase change materials, Sol. Energy Mater. Sol. Cells 251 (2023) 112118, https://doi.org/10.1016/j.solmat.2022.112118.
[162] Y. Zhong, M. Zhou, F. Huang, T. Lin, D. Wan, Effect of graphene aerogel on thermal behavior of phase change materials for thermal management, Sol. Energy Mater. Sol. Cells 113 (2013) 195–200, https://doi.org/10.1016/j.solmat.2013.01.046.
[163] Z. Tao, H. Zou, M. Li, S. Ren, J. Xu, J. Lin, M. Yang, Y. Feng, G. Wang, Polypyrrole coated carbon nanotube aerogel composite phase change materials with enhanced thermal conductivity, high solar-/electro- thermal energy conversion and storage, J. Colloid Interface Sci. 629 (2023) 632–643, https://doi.org/10.1016/j.jcis.2022.09.103.
[164] M. Mehrali, S.T. Latibari, M.A. Rosen, A.R. Akhiani, M.S. Naghavi, E. Sadeghinezhad, H.S.C. Metselaar, M.M. Nejad, M. Mehrali, From rice husk to high performance shape stabilized phase change materials for thermal energy storage, RSC Adv. 6 (2016) 45595–45604.
[165] X. Zhang, Q. Lin, H. Luo, S. Luo, Three-dimensional graphitic hierarchical porous carbon/stearic acid composite as shape-stabilized phase change material for thermal energy storage, Appl. Energy 260 (2020) 114278, https://doi.org/10.1016/j.apenergy.2019.114278.
[166] Y. Luo, F. Zhang, C. Li, J. Cai, Biomass-based shape-stable phase change materials supported by garlic peel-derived porous carbon for thermal energy storage, J Energy Storage 46 (2022) 103929, https://doi.org/10.1016/j.est.2021.103929.
[167] K. Zhou, Y. Sheng, W. Guo, L. Wu, H. Wu, X. Hu, Y. Xu, Y. Li, M. Ge, Y. Du, X. Lu, J. Qu, Biomass porous carbon/polyethylene glycol shape-stable phase change composites for multi-source driven thermal energy conversion and storage, Adv. Compos. Hybrid Mater. 6 (2023) 34, https://doi.org/10.1007/s42114-022-00620-1.

[168] Xifeng Lv, Hui Cao, Guohua Li, Mengying Zhu, Wei Ji, Kai Wang, Changwei Zhang, Su Changsheng, Wenqiang Ren, Di Cai, Spent yeast-derived 3D porous carbon skeleton as low-cost D-mannitol supporting material for medium temperature thermal energy storage, Materials 16 (2023) 2569.
[169] X. Chen, H. Gao, G. Hai, D. Jia, L. Xing, S. Chen, P. Cheng, M. Han, W. Dong, G. Wang, Carbon nanotube bundles assembled flexible hierarchical framework based phase change material composites for thermal energy harvesting and thermotherapy, Energy Storage Mater 26 (2020) 129–137, https://doi.org/10.1016/j.ensm.2019.12.029.
[170] K. Sun, Y. Kou, Y. Zhang, T. Liu, Q. Shi, Photo-triggered hierarchical porous carbon-based composite phase-change materials with superior thermal energy conversion capacity, ACS Sustain. Chem. Eng. 8 (2020) 3445–3453, https://doi.org/10.1021/acssuschemeng.9b07659.
[171] Q. Ye, P. Tao, C. Chang, L. Zhou, X. Zeng, C. Song, W. Shang, J. Wu, T. Deng, Form-stable solar thermal heat packs prepared by impregnating phase-changing materials within carbon-coated copper foams, ACS Appl. Mater. Interfaces 11 (2019) 3417–3427, https://doi.org/10.1021/acsami.8b17492.
[172] C. Li, J. Liao, B. Xie, P. Cao, Y. Long, Three dimensional hybrid microcrystalline graphite-silica sol stabilized stearic acid as composite phase change material for thermal energy storage, J Energy Storage 72 (2023) 108328, https://doi.org/10.1016/j.est.2023.108328.
[173] B. Kalidasan, A.K. Pandey, R. Saidur, Belqasem Aljafari, Aman Yadav, M. Samykano, Green synthesized 3D coconut shell biochar/polyethylene glycol composite as thermal energy storage material, Sustain Energy Technol Assess 60 (2023) 103505.
[174] Z. Tang, P. Cheng, P. Liu, Y. Gao, X. Chen, G. Wang, Tightened 1D/3D carbon heterostructure infiltrating phase change materials for solar–thermoelectric energy harvesting: faster and better, Carbon Energy 5 (2023), https://doi.org/10.1002/cey2.281.
[175] https://en.wikipedia.org/wiki/Beeswax (accessed July 20, 2022).
[176] X. Zheng, N. Xie, C. Chen, X. Gao, Z. Huang, Z. Zhang, Numerical investigation on paraffin/expanded graphite composite phase change material based latent thermal energy storage system with double spiral coil tube, Appl. Therm. Eng. 137 (2018) 164–172, https://doi.org/10.1016/j.applthermaleng.2018.03.048.
[177] G. Fang, P. Sun, M. Zhao, W. Zhang, Experimental and numerical simulation of paraffin-based ternary composite phase change material used in solar energy system, Appl. Therm. Eng. 214 (2022) 118618, https://doi.org/10.1016/j.applthermaleng.2022.118618.
[178] J. B S, B.K. Ramaraj, R.K. Kottala, S. S P, A complete numerical model for low temperature composite form-stable phase change material slab based on dynamically simplified temperature transforming method, Energy Sources, Part A (2021) 1–26. doi:https://doi.org/10.1080/15567036.2021.1944403.
[179] A. Greco, X. Jiang, D. Cao, An investigation of lithium-ion battery thermal management using paraffin/porous-graphite-matrix composite, J. Power Sources 278 (2015) 50–68, https://doi.org/10.1016/j.jpowsour.2014.12.027.
[180] J. Li, W. Zhang, W. Ji, J. Wang, N. Wang, W. Wu, Q. Wu, X. Hou, W. Hu, L. Li, Near infrared photothermal conversion materials: mechanism, preparation, and photothermal cancer therapy applications, J. Mater. Chem. B 9 (2021) 7909–7926, https://doi.org/10.1039/D1TB01310F.
[181] X. Fan, J. Xiao, W. Wang, Y. Zhang, S. Zhang, B. Tang, Novel magnetic-to-thermal conversion and thermal energy management composite phase change material, Polymers (Basel) 10 (2018) 585, https://doi.org/10.3390/polym10060585.
[182] S. Harish, D. Orejon, Y. Takata, M. Kohno, Thermal conductivity enhancement of lauric acid phase change nanocomposite in solid and liquid state with single-walled carbon nanohorn inclusions, Thermochim. Acta 600 (2015) 1–6, https://doi.org/10.1016/j.tca.2014.12.004.
[183] F. Ye, Z. Ge, Y. Ding, J. Yang, Multi-walled carbon nanotubes added to Na2CO3/MgO composites for thermal energy storage, Particuology 15 (2014) 56–60, https://doi.org/10.1016/j.partic.2013.05.001.
[184] A.A. Mikhaylov, A.G. Medvedev, D.A. Grishanov, S. Sladkevich, Z.J. Xu, K. A. Sakharov, P.V. Prikhodchenko, O. Lev, Doubly coated, organic–inorganic paraffin phase change materials: zinc oxide coating of hermetically encapsulated paraffins, Adv. Mater. Interfaces 6 (2019), https://doi.org/10.1002/admi.201900368.
[185] N. Şahan, M. Fois, H. Paksoy, Improving thermal conductivity phase change materials—a study of paraffin nanomagnetite composites, Sol. Energy Mater. Sol. Cells 137 (2015) 61–67, https://doi.org/10.1016/j.solmat.2015.01.027.
[186] J.L. Zeng, Z. Cao, D.W. Yang, L.X. Sun, L. Zhang, Thermal conductivity enhancement of ag nanowires on an organic phase change material, J. Therm. Anal. Calorim. 101 (2010) 385–389, https://doi.org/10.1007/s10973-009-0472-y.
[187] S. Yu, X. Wang, D. Wu, Microencapsulation of n-octadecane phase change material with calcium carbonate shell for enhancement of thermal conductivity and serving durability: synthesis, microstructure, and performance evaluation, Appl. Energy 114 (2014) 632–643, https://doi.org/10.1016/j.apenergy.2013.10.029.
[188] S.O. Alayande, E.O. Dare, F.O.G. Olorundare, D. Nkosi, T.A.M. Msagati, B. B. Mamba, Superoleophillic electrospun polystrene/exofoliated graphite fibre for selective removal of crude oil from water, Physics and Chemistry of the Earth, Parts A/B/C 92 (2016) 3–6, https://doi.org/10.1016/j.pce.2015.09.004.
[189] Z.-X. Huang, X. Liu, S.-C. Wong, J. Qu, Electrospinning polyvinylidene fluoride/expanded graphite composite membranes as high efficiency and reusable water harvester, Mater. Lett. 202 (2017) 78–81, https://doi.org/10.1016/j.matlet.2017.05.067.
[190] L. Liu, W. Xu, Y. Ding, S. Agarwal, A. Greiner, G. Duan, A review of smart electrospun fibers toward textiles, Composites Communications 22 (2020) 100506, https://doi.org/10.1016/j.coco.2020.100506.
[191] D.P. Ura, K. Berniak, U. Stachewicz, Critical length reinforcement in core-shell electrospun fibers using composite strategies, Compos. Sci. Technol. 211 (2021) 108867, https://doi.org/10.1016/j.compscitech.2021.108867.
[192] J. Knapczyk-Korczak, J. Zhu, D.P. Ura, P.K. Szewczyk, A. Gruszczyński, L. Benker, S. Agarwal, U. Stachewicz, Enhanced water harvesting system and mechanical performance from Janus fibers with polystyrene and cellulose acetate, ACS Sustain. Chem. Eng. 9 (2021) 180–188, https://doi.org/10.1021/acssuschemeng.0c06480.
[193] J. Knapczyk-Korczak, D.P. Ura, M. Gajek, M.M. Marzec, K. Berent, A. Bernasik, J. P. Chiverton, U. Stachewicz, Fiber-based composite meshes with controlled mechanical and wetting properties for water harvesting, ACS Appl. Mater. Interfaces 12 (2020) 1665–1676, https://doi.org/10.1021/acsami.9b19839.
[194] E. Zdraveva, J. Fang, B. Mijovic, T. Lin, Electrospun poly(vinyl alcohol)/phase change material fibers: morphology, heat properties, and stability, Ind. Eng. Chem. Res. 54 (2015) 8706–8712, https://doi.org/10.1021/acs.iecr.5b01822.
[195] C. Chen, Y. Zhao, W. Liu, Electrospun polyethylene glycol/cellulose acetate phase change fibers with core–sheath structure for thermal energy storage, Renew. Energy 60 (2013) 222–225, https://doi.org/10.1016/j.renene.2013.05.020.